UCGE Reports

Number 20275

Department of Geomatics Engineering

Near Real-time GPS PPP-inferred Water Vapor System Development and Evaluation

(URL: http://www.geomatics.ucalgary.ca/research/publications)

by

Wenyou Tao

October 2008

UNIVERSITY OF CALGARY

Near Real-time GPS PPP-inferred Water Vapor System Development and Evaluation

by

Wenyou Tao

A THESIS

SUBMITTED TO THE FACULTY OF GRADUATE STUDIES

IN PARTIAL FULFILMENT OF THE REQUIREMENTS FOR THE

DEGREE OF MASTER SCIENCE

DEPARTMENT OF GEOMATICS ENGINEERING

CALGARY, ALBERTA

October, 2008

Abstract

Atmospheric water vapour is one of the key parameters for the analysis of global climate systems, in particular over high latitudes where water vapour displays a significant seasonal variability. The lack of detailed knowledge of the global distribution of atmospheric water vapour in space and time is the major limiting factor toward the accurate prediction of weather and climate using numerical models. In Canada, the sparse spatial and temporal sampling of atmospheric water vapour observations needs to be improved. GPS water vapour observations retrieved from geodetic (GPS) networks have provided a unique opportunity for this need.

At present water vapor determination using GPS is mainly based on Differential GPS (DGPS) techniques. But the large inter-station distance requirement has limited the DGPS application in meteorology, because the GPS stations have to be sufficiently separated in the network in order to estimate the water vapor on each station. An innovative alternative to the DGPS technique is the Precise Point Positioning (PPP) method which uses un-differenced observations from a single GPS receiver aided by precise orbit and clock products.

The primary objective of this thesis is to develop a *near* real-time GPS PPP-inferred water vapour system using precise point positioning (PPP) technique and Canada sparsely distributed geodetic GPS network for operational weather forecasting, climate monitoring and research. The fundamental problems in meeting this objective are: designing and implementing a distributed GPS computing network system, interpolating surface maps of precipitable water vapour (PWV) over Canada using the sample data derived from the system, and analyzing GPS water vapour datasets.

The desired system is designed and implemented with five functional components which are distributed over the Internet across Canada and cooperate under UDP/IP Multicast UDP/IP protocols. The system concurrently processes multi-station GPS data and produces (near) real-time tropospheric products ZTD/ZWD/PWV. The system performance evaluation shows: (i) the position errors (East/North/Up): RMS = l.1 ~ 4.3 cm and (ii) the ZTD and PWV accuracies of the (near) real-time water vapor system are ~13 mm and ~2mm, respectively, with the use of one-hour-latency MET data.

In the process of interpolating surface maps of PWV, an *ordinary kriging* program has been developed in Matlab, which performances calculating experimental semivariogram, model fitting and ordinary kriging algorithm for interpolation. Three most common models are used: *Spherical*, *Exponential* and *Gaussian*. Model fitting consists of (i) *nonlinear weighted least-squares* process for model parameter estimation and (ii) *cross-validation* process for the best model determination. The hourly kriginged PWV maps over Canada and associated kriging standard error maps are generated by the ordinary kriging program using limited-sample datasets, which provide valuable information to evaluate the meteorological role of the current Canada geodetic GPS network.

In the process of analyzing GPS water vapor dataset, we first categorize 17 variables into four types and then use (i) *principal component analysis* (PCA) to derive the six-principal-component/domain structure and six determinant variables of the system and (ii) *correlation analysis* to investigate and summarize quantitatively seven correlations among the four types.

Acknowledgements

God, the Almighty you are always a wonderful inspiration to me.

I would like to extend my heartfelt gratitude to my mother, Wenhui. Thanks for all the love and support for many years.

To my adviser, Professor Dr. Yang Gao, thank you very much for your patience, guidance, encouragement and unlimited support while I fully explored my thesis project.

To my committee members, Professor Dr. Susan Skone and Professor Dr. Naser El-Sheimy from the Department of Geomatics Engineering, and Professor Dr. Abraham Fapojuwo from the Department of Electrical and Computer Engineering, thank you very much for imparting your knowledge, and for checking and editing my work.

To my research colleagues, Yufeng Zhang, Kongzhe Chen, Zhizhao Liu and Min Wang, thank you for frequent help and consultation for the past three years.

To the BCC church, especially to Poster Roger Wu, Dr. Patrick Wu, Poster Meiping Law, thank you for your consistent encouragement and support.

To all faculty and staff members, the University of Calgary, thank you for providing the beautiful academic environment.

Thanks also to the Canadian Geomatics for Informed Decisions (GEOIDE) Network Centers of Excellence (NCE) and Natural Sciences and Engineering Research Council of Canada for their financial support and to the Natural Resource Canada (NRCan) for their valuable contributions to the project.

Table of Contents

List of Figures

List of Tables

List of Abbreviations

DGPS	Differential GPS
DOP	Dilution of precision
DOY	Day of year
ECEF	Earth centered earth fixed
FTP	File transfer protocol
GDOP	Geometric dilution of precision
GNSS	Global navigation satellite system
GPS	Global point positioning
HDOP	Horizontal dilution of precision
IGS	International GPS service
ITRF	International terrestrial reference frame
IWV	Integrated water vapour
IP	Internet protocol
JPL	Jet propulsion lab
LEO	Low earth orbit
MET	Meteorological
NAVSTAR	Navigation satellite timing and ranging
NRCan	Natural resource Canada
NWP	Numerical weather prediction
PCA	Principal component analysis
PDOP	Positional dilution of precision
PPP	Precise point positioning
PRN	Pseudo-random noise
PWV	Precipitable water vapour
RCP	Right circularly polarized
RTIGSA	Real-time IGS archive
SDD	Slant dry delay
STD	Slant total delay
SOPAC	Scripps orbit and permanent array center
SWD	Slant wet delay
TDOP	Time dilution of precision
RMS	Root mean square
UDP	User datagram protocol
WVR	Water vapor radiometer
VDOP	Vertical dilution of precision
ZTD	Zenith total delay
ZWD	Zenith wet delay
ZDD	Zenith dry Delay
ZHD	Zenith hydrostatic delay

List of Symbols

μ	Mean value
λ	Wavelength
ρ	Pseudorange
δt_u	Offset of GPS receiver clock
δt^s	Offset of satellite clock
ε_ρ	Effect of multipath and receiver noise
ε_ϕ	Un-modeled effects, modeling error and measurement error for carrier phase observation
ϕ	Phase observable
$\gamma(\vec{h})$	Semivariogram
τ_{GM}	Gaussian Markov correction time
Φ_{L1}	Phase measurement at L1
$\Phi_{:L2}$	Phase measurement at L2
Φ_{IF}	Ionosphere-free phase measurement
f	Carrier frequency
f_{L1}	L1 carrier frequency
f_{L2}	L2 carrier frequency
$m_d(e)$	Dry mapping function
$m_{wv}(e)$	Wet mapping function
$n(s)$	Refractive index
p_d	Universal gas constant for ideal gas
p_{wv}	Universal gas constant for water vapor
r	Geometric range
$w(t)$	Zero-mean white noise random variable of variance
I_ϕ	Ionosphere carrier phase advance
I_ρ	Ionosphere code delay
$L1$	L1 carrier (1575.42 MHz)
$L2$	L2 carrier (1227.60 MHz)
N	Integer ambiguity resolution
$N(s)$	Atmospheric refractivity
N_d	Ideal gas (dry) refractivity
N_{wv}	Water vapor refractivity
M_d	Molar mass for ideal gas
M_{wv}	Molar mass for water vapour
P_{IF}	Ionosphere-free pseudorange
P_{L1}	Pseudorange measurement at L1

P_{L2}	Pseudorange measurement at L2
Q	Dimensionless conversion factor: 5.9 ~ 6.5
R_d	Dry air constant
T	Troposphere delay
Z_d	Compressibility factor for dry air
Z_{wv}	Compressibility factor for water vapour
$Z(\vec{s})$	Real-valued stochastic process

Chapter One: Introduction

Since Global Positioning System (GPS) data were demonstrated to be a good source for measuring atmospheric water vapor, there have been extensive studies of the role that GPS water vapor measurements could play in weather prediction. There are two primary methods by which GPS can be used to actively sense the properties of the Earth's atmosphere: ground-based and space-based (Businger et al., 1996). This study concerns the ground-based GPS atmospheric water vapor sensing.

Water vapor is a normal constituent of atmosphere. It resides mostly in the troposphere (Figure 1.1), ranging in depth from 9 km at the poles to more than 16 km at the equator. Water vapor content decreases rapidly with elevation (Figure 1.2). In fact, more than 90% of the water vapor is contained within the lower 5 km of the troposphere and more than 50% within the lowest 1.5 to 2 km; only less than 5-6% of the water is above 5 km, and less than 1% is in the stratosphere (Ramirez, 2007).

Water vapor in the atmosphere is a crucial constituent on the climate system. The presence of water vapor is relatively small amounts, generally not exceeding 4% by volume, but the significance of the water vapor is far greater than the relative amount

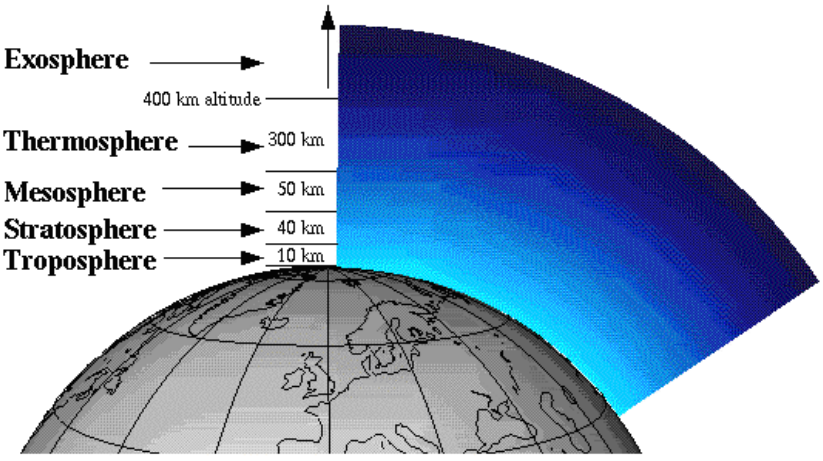

Figure 1.1 Layers of Atmosphere
(Williams, 2008)

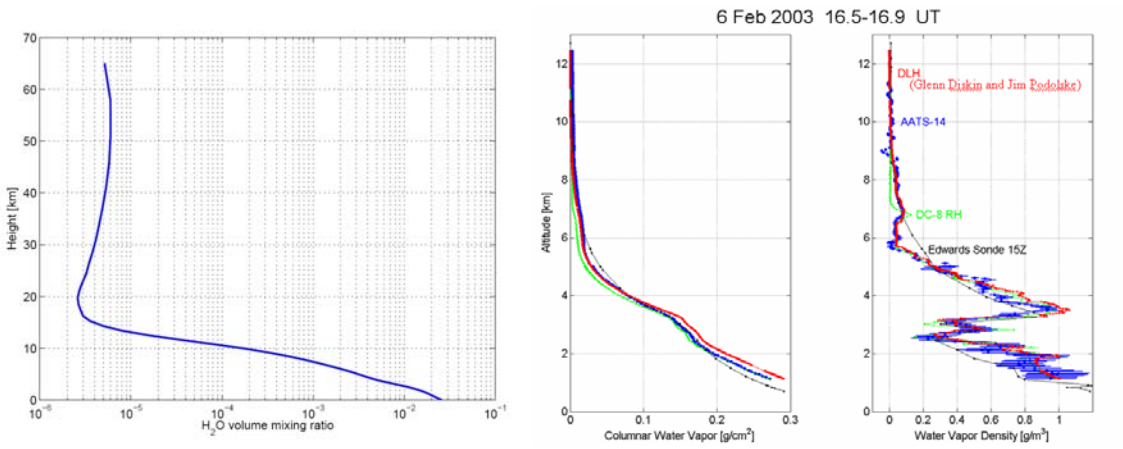

(a) **(b)**

Figure 1.2 Water vapor profiles

((a) Vertical distribution of water vapor for a standard atmosphere (Source: US Standard Atmosphere 1976); (b) Water vapor vertical profiles in and where each color line represents different method result (Russell et al., 2003))

would indicate (Hidore, 1972). The distribution and content of water vapor are critical factors for the description of the state and evolution of the atmosphere. Water vapor impacts the global climate in two ways. First it plays a fundamental role in the Earth's hydrological cycle: transferring of energy in the atmosphere, forming and propagating weather (Figure 1.3) (Hidore, 1972; Seidel, 1995). Second it is the dominant greenhouse gas in the atmosphere (Cess, 2005; Hieb, 2003). It allows the short wavelength radiation of the Sun to pass through the atmosphere, but traps the long wavelength radiation emitted by the Earth's surface. This trapped radiation causes the temperatures to increase.

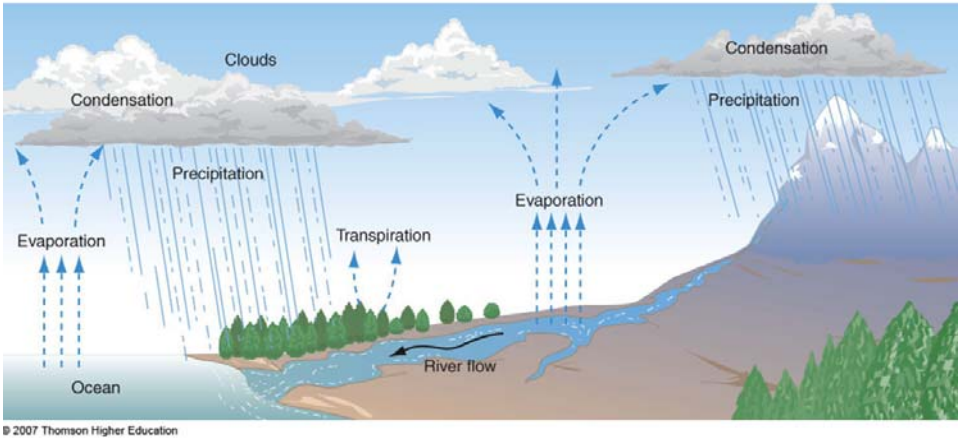

Figure 1.3 The climatic hydrological cycle at global scale
(Warner, 2006)

Atmospheric scientists employ three main techniques to routinely measure the water vapor: (i) In-situ measurements, i.e. radiosondes, (ii) remote sensing from the ground, i.e. ground-based upward-looking radiometry, and (iii) remote sensing from space, i.e. satellite-based downward-looking radiometry (Bevis, 1992).

In-situ measurements are radiosondes. Radiosondes are balloon-borne instrument packages which send data on pressure, ambient temperature, relative humidity, and wind (speed and direction) to the ground by radio signal. Although radiosonde provides respectable water vapor profiles, it has weaknesses of being expensive on the long run, a low temporal resolution (usually two launches per day), a low spatial distribution (i.e., point measurement), a questionable accuracy, and being sparsely distributed on the earth surface (Brocard, 2006). Thus, low spatial and temporal resolution of water vapor from radiosonde, and limitations of water vapor data, are major sources of error in short-term (< 24 hour) forecasts of precipitation (Rocken et al., 1993).

Ground-based radiometry employs *upward-looking* water vapor radiometer (WVR) to measure microwave energy emitted by the atmosphere which is converted into zenithal integrated water vapor (IWV) using retrieval coefficients. Retrieval coefficients are derived from regression analysis of radiosonde data which depend on climate and site variations. Ground-based radiometry provides high temporal but poor spatial resolution because only a few of these instruments are used today.

Alternatively, *satellite-based radiometry* employs *downward-looking* WVRs to measure microwave emissions from the atmosphere and underlying Earth's surface. The recovery of IWV by *downward-looking* WVRs is greatly affected by large variability in the surface brightness temperature and the results are limited to cloud-free conditions. For this reason, satellite-based radiometry tends to be more applicable over the oceans than over land, and their effectiveness is degraded in the presence of clouds. Satellite-based radiometry provides good spatial but poor temporal resolution. Both ground- and satellite-based radiometry are highly complementary and operating both together can improve short term (1~12 hour) forecasting. However, both have common weaknesses: (i) noisy signals during rainy weather as microwave is absorbed and scattered by raindrops, (ii) expensive to operate (Li et al., 2005), and (iii) limited in high-latitude areas like the Arctic.

Each of above techniques, either *in situ* measurement, ground-based or satellite-based remote sensing, has various limitations and often does not adequately provide important quantity information such as atmospheric water vapor required by the climatic research (Bevis et al., 1992). In May 1995, a report produced by the U.S. Weather Research Program identified a national need for a reliable, low-cost system for measuring atmospheric water vapor (Michelsen, 1998).

Bevis et al. (1992) presented the discussion on GPS method for measuring water vapor. This discussion shows a technical challenge using GPS to measure atmospheric water vapor. GPS was originally designed as a navigation and time transfer tool. The signals emitted from GPS satellites propagate through the ionosphere and neutral atmosphere to be received by ground based GPS receivers. One of the major error sources to positioning or navigating with GPS is the signal delay caused by atmospheric refraction. The total delay of the radio signals between a GPS satellite and a ground GPS receiver is essentially dependent on the total atmospheric mass, *i.e.*, the pressure at the surface, and the columnar atmospheric moisture content. Over the years, research efforts have been dedicated to modelling atmospheric refraction in order to improve on positioning accuracy. In the last decade, the estimation techniques used to solve for the atmosphere has been refined so that such delay can be determined on a routine basis with a high degree of accuracy. This innovation has lead to the possibility of using the GPS for remote sensing, known as *GPS meteorology*, which is currently becoming an active area of research (Alan and Shardlow, 1995; Awange and Grafarend, 2005).

The new technology of GPS atmospheric remote sensing has several advantages over the conventional water vapor observing system including low cost, being global coverage, reliable and stable result, high measurement accuracy, all weather operability and having radio frequencies that can penetrate clouds and dusts (Awange and Grafarend, 2005; Gutman et al., 2004). This new technology plays a major role in complementing the existing techniques, e.g. radiosonde and WVR. Figure 1.4 shows the GPS derived zenith wet delay compared with the radiosonde and WVR derived zenith wet delays at Haystack observatory, USA from 15-30 August 1995 (Coster et al., 1997).

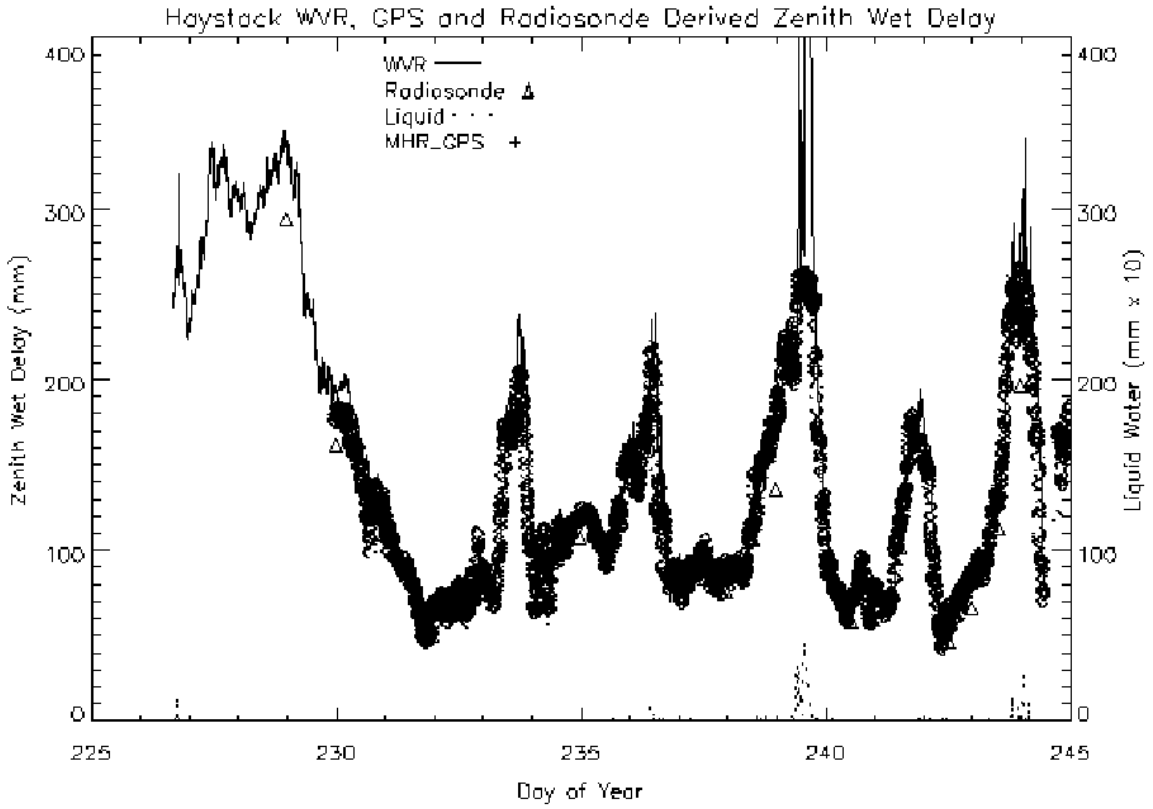

Figure 1.4 The comparison of radiosonde, WVR and GPS derived zenith wet delay at Haystack observatory in Westford, MA, USA, from 15-30 August 1995
(With the exception of the time periods associated with rain, it is clear that the estimates of the zenith wet delay from three techniques agree very closely (Coster et al., 1997))

In 1995, the results from the first proof of concept experiment GPS/STORM were first reported (Rocken et al., 1995). Subsequently there has been substantial activity involving ground-based GPS measurements in studies at various scales from national to global. Many of these initiatives are being carried out by research institutions in collaboration with national agencies, principally to assess the accuracy of ground-based GPS estimates of integrated water vapor (IWV) using the network of GPS stations (Bengtsson et al., 2003; Hagemann et al., 2002; Rocken et al., 1997; Ware and Gutman 2003; Wolfe et al., 2000). But their aim is also to develop and refine the fundamental techniques involved in making the observations, processing the data and making them available in a timely manner (Hagemann et al., 2002).

In Canada, some similar research activities have been carried out in recent years. A study was conducted to analyze the characteristics of high-latitude water vapor time series at some sites of Canadian Sun Radiometer Network/Aerosol Robotic Network

(AERONET/AEROCAN) (Bokoye et al., 2003). This research shows: (i) GPS meteorology can retrieve columnar water vapor amounts with an accurate (RMS) of less than ± 2 kg m^{-2} as compared to radiosonde data; (ii) In comparison to radiometer, GPS meteorology is potentially more appropriate for monitoring water vapor in Arctic regions where there are months when the Sun is absent or nearly so. In 2004, Deblonde and Macpherson (2005) conducted a similar research in order to evaluate GPS precipitable water over the IGS network in Canada. Through the inter-comparisons of IGS GPS_PW with radiosonde_PW and the Global Environmental Multiscale (GEM) model_PW for a seven-month period, it is found that the GPS_PW has the lowest estimated PW error (~1 mm) for PW in the 5~30 mm range. For PW greater than 30 mm, the radiosonde_PW error is ~2 mm while the GPS_PW error is ~2.5 mm. In Southern Alberta, Canada the water vapor profile was retrieved using GPS technology to investigate the estimation of vertical profiles of water vapor in a regional GPS network and the results indicate the improvements in the integrated domain were on the order of ~5 mm for the assimilation of radiosonde data (Skone and Shrestha, 2003; Hoyle et al., 2003; Hoyle, 2005). All these studies demonstrate that GPS atmospheric remote sensing technology is a key method to improve high latitude sparse spatial and temporal sampling of water vapor observation in Canada and that GPS precipitable water vapor (PWV) should be a useful source of humidity information for Numerical Weather Prediction (NWP) applications. Today, GPS meteorology has transitioned from research into a global operational network (Haan, 2006). However, there is still no operational GPS network for GPS meteorology in Canada. Thus, as a practical issue, it is important to build up a network of GPS stations across Canada which can routinely retrieve PWV for weather prediction, atmospheric research, and climate monitoring and prediction. This problem is the main motivation of this thesis. In the following chapters, the methods for completing a real-time water vapor monitoring system using GPS PPP (Precise Point Positioning) technique and a Canadian GPS network are presented.

1.1 Objectives

The primary objective of this thesis is to develop a real-time GPS PPP-inferred water vapor system using a Canadian GPS network.

There are two GPS techniques for water vapor remote sensing: Differential GPS (DGPS) and PPP. DGPS is most commonly used in today's GPS networks. It employs two or more receivers simultaneously observing GPS satellites and provides the solutions with high accuracy level. Its effectiveness, however, is limited by the inter-station distance between the two receivers. In contrast, PPP uses one GPS receiver to observe GPS satellites with the aid of precise GPS orbit and clock products and produces high-precision PWV results. Since PPP eliminates the limitation of inter-station distance, it can be efficiently implemented under any configurations of GPS networks. At present, there is no nationwide sparsely-distributed GPS network using PPP technique. The implementation of PPP technique within a Canada GPS network in this thesis is a valuable testimony for GPS PPP based PWV research. The implementation of PPP technique is based on the core functions of P^3 software developed at The University of Calgary and the additional software components that have been developed from this thesis to support concurrent multi-station GPS data processing in a real-time mode.

The system has the following major functions implemented:

1. Real-time raw GPS data acquisition – implemented using a Canadian GPS network which consists of 21 GPS stations,
2. Network data communication for real-time GPS retrieving,
3. Concurrent multi-station GPS data processing to calculate water vapor,
4. Displaying real-time water vapor (PWV) distribution visually, and
5. PWV data storage and output.

The real-time GPS PPP-inferred water vapor system is developed in the following four stages:

1. System design and implementation,
2. Evaluation of system performance,
3. Water vapor interpolation and mapping by ordinary kriging, and
4. Principal component analysis of GPS water vapor dataset.

To evaluate the system performance, the post-mission results are presented. The inter-comparisons of the tropospheric results from (near) real-time system, IGS and post-mission are conducted.

1.2 Contributions

In this thesis, a real-time GPS water vapor system has been developed using real-time PPP technique and a Canadian GPS network. Its performance and meteorological role under *near* real-time operation mode has been evaluated. The contribution of each of 17 original GPS water vapor variables to the system variability and the association between them has been investigated. The specific contributions of this thesis are as follows:

1. A real-time GPS PPP-inferred water vapor system based on a Canadian GPS network has been developed. The system generates and outputs (near) real-time PWV products under all weather conditions. The system performance evaluation show that water vapor estimates have an accuracy of 1.5 ~ 2.0 mm. An evaluation on the current Canadian GPS network performance as a meteorological role has also been conducted.
2. A program which uses Ordinary Kriging technique to predict and quantitatively describe water vapor distribution over Canada using the PWV samples from the system has been developed. The program performs (i) calculating experimental semivariogram, (ii) fitting semivariogram models by a nonlinear weighted least-square process, (iii) determining best model using cross-validation, and (iv) estimating PWV map and associated standard error map.
3. A Principal Component Analysis (PCA) and variable correlation analysis on GPS water vapor dataset has been conducted. *PCA* derives a seven-principal component/domain model, which simplifies the description of the set of intercorrelated original variables. *The variable correlation analysis* arrives at the conclusions of the associations between 17 variables of GPS-derived water vapor variables.

1.3 Outline

Chapter 2 presents the theoretical background of GPS water vapor remote sensing, which includes a brief introduction of GPS, the effect of troposphere on GPS measurement, GPS sensing techniques.

Chapter 3 presents the GPS PPP water vapor determination model used in this thesis. Precise Point Positioning error correction models are also described.

In Chapter 4, the design of the real-time GPS water vapor sensing system design and how it is implemented are explained. The system consists of five functional components and each component's function is illustrated. Since currently the meteorological data are provided with one-hour latency files, an auxiliary component is used to handle the downloading and unzipping the hourly meteorological files.

Chapter 5 gives the evaluation of the system performance, which includes positioning errors, zenith total delay (ZTD) and zenith wet delay (ZWD). In order to have a general assessment of the accuracy of the PPP-derived ZTD products, the accuracy comparison results of the real-time system are presented with some operational GPS network ZTD products.

The whole program for real-time precipitable water vapor prediction and interpolation is presented in Chapter 6. The geostatistic theory of kriging, which is the basis of this program, is briefly introduced. The three-step interpolation process of the ordinary kriging is illustrated using a one-day real-time sample data to generate 24 hourly PWV maps.

The principal component analysis (PCA) and the variable correlation analysis of GPS water vapor dataset are provided in Chapter 7. The 17 variables of the system are categorized into four groups. The chapter starts with a brief review of PCA theory and then explains the PCA process to derive a seven-principal-component/domain structure, which simplifies the description of the set of intercorrelated variables. A variable correlation analysis is further presented using the scatter plots and linear regression.

The conclusions and future work are given in Chapter 8.

Chapter Two: GPS Meteorology

This chapter presents the theory of GPS water vapor remote sensing and its applications.

2.1 Introduction to GPS

The GPS system is officially known as the NAVSTAR System (Navigation Satellite Timing and Ranging). It was originally envisioned as a ranging system from known positions of satellites in space to unknown positions on land, sea, in air and space. The GPS constellation consists of 24 satellites in 6 orbital planes with 4 satellites in each plane. (Currently, at least 31 GPS satellites are operated) The ascending nodes of the orbital planes are separated by 60 degrees and the planes are inclined 55 degrees. Each GPS satellite is in an approximately circular, semi-synchronous (20,200 km altitude) orbit (see Figure 2.1). The orbits of the GPS satellites are available from navigation message broadcast from GPS satellites or (in much better accuracy knows as precise orbits) organizations such as the Jet Propulsion Lab (JPL) and the International GNSS Service (IGS). The GPS receivers convert the satellite's signals into position, velocity, and time estimates for navigation, positioning, time dissemination, or geodesy.

Figure 2.1 Constellation of 24 GPS satellites (not to scale) which consists of six orbits (which has four satellites. The ascending nodes of the orbital planes are separated by 60 degrees; the planes are inclined 55 degrees (Willkommen, 2005))

GPS signals

Each GPS satellite transmits two signals for positioning purposes (Langley, 1990):

- **L1 signal**. Modulated onto the L1 carrier (1,575.42 MHz) are two pseudo-random noise (PRN) ranging codes and the navigation (*broadcast*) message. The codes (used to determine the pseudo-ranges) are (a) the 1 millisecond-long C/A-code (effective wavelength of ~300 m); (b) the weeklong segment of the P-code (effective wavelength of ~30 m). The navigation (*broadcast*) message comprises satellite orbital information (*ephemeris*), ionospheric modeling coefficients, status information, system time and satellite clock bias, and drift information.
- **L2 signal.** Modulated onto the L2 carrier (1,227.60 MHz) are the P-code and the navigation message — the C/A code is not present.

The PRN codes are unique for each satellite and the correlation between any pair of codes is very low. This allows all satellites to share the same carrier frequency.

The above GPS signals have some clear weakness: (i) Civil user has only access to the C/A-code on L1; (ii) they are not provided total spectrum protection and can not easily penetrate into interference and jamming; and (iii) the reflected signals (multipath) cause position errors. In 1996, a GPS modernization was planned and since then it has been advanced. According to this plan, a new civil signal would be added to the GPS L2 frequency. Instead of replicating the C/A-code, a truly modernized L2 civil (L2C) signal was designed. Also, to satisfy the needs of aviation, the third civil frequency, known as L5, would be centred at 1176.45 MHz, in the Aeronautical Radio Navigation Services (ARNS) band (Bruyninx, 2008).

- **L2C signal.** Modulated onto the L2 carrier are, two distinct PRN code sequences to providing ranging information; the Civilian Moderate length code (called CM), and the Civilian Long length code (called CL). The CM code is 10,230 bits long, repeating every 20 ms. The CL code is 767,250 bits long, repeating every 1500 ms. Each signal is transmitted at 511,500 bits per second (bit/s), however they are multiplexed together to form a 1,023,000 bit/s signal. L2C is tasked with

improving accuracy of navigation, providing an easy to track signal, and acting as a redundant signal in case of localized interference (Bruyninx, 2008).

GPS observables

Pseudorange. The pseudorange is the measured distance between a GPS satellite at some transmit time and the receiver's antenna at some receive time. It is calculated by the time the signal takes to propagate from the satellite to the receiver multiplied by the speed of light. The pseudorange is biased by the lack of time synchronization between the clock in the GPS satellite and the clock in the GPS receiver. Other bias effects include the ionosphere and troposphere delay, multipath and receiver noise. The equation for the pseudorange observable is (Misra and Enge, 2001):

$$\rho = r + c \cdot \left(\delta t_u - \delta t^s\right) + I_\rho + T + \varepsilon_\rho \tag{2.1}$$

where ρ is the pseudorange, r is the geometric range from the receiver to the satellite, c is the speed of light, δt_u and δt^s are the offsets of the receiver and satellite clock from the GPS time, I_ρ and T are the delays imparted by the ionosphere and troposphere and ε_ρ represents the effect of multipath and receiver noise. The receiver coordinates (x, y, z) are related with the geometric range r along with the coordinates of the satellite $\left(x^s, y^s, z^s\right)$ in the form of $r^2 = \left(x^s - x\right)^2 + \left(y^s - y\right)^2 + \left(z^s - z\right)^2$.

Carrier phase. The phase observable (ϕ) is the difference between the received satellite carrier phase (sensed by the receiver's antenna) and the phase of the internal receiver oscillator, which is also called carrier beat phase. A phase measurement is "ambiguous" as it cannot discriminate one (either L1 or L2) wavelength from another. The receiver measures the fractional phase and keeps track of the number of whole wavelengths of the carrier wave. The initial phase is undetermined, or ambiguous, by an integer number of cycles *N*. The equation for the carrier phase observation is (Misra and Enge, 2001):

$$\phi = \lambda^{-1} \cdot \left(r - I_\phi + T\right) + f \cdot \left(\delta t_u - \delta t^s\right) + N + \varepsilon_\phi \tag{2.2}$$

where N is the integer ambiguity and f is the carrier frequency. Estimation of N is referred to as *integer ambiguity resolution* or *initialization*. I_ϕ and T are the delays imparted by the ionosphere and troposphere and ε_ϕ represents the un-modeled effects, modeling error and measurement error for carrier phase observation. The carrier measurements in equation (2.2) can be converted to units of length by multiplying the wavelength (Misra and Enge, 2001):

$$\begin{aligned}\Phi &= \lambda \cdot \phi \\ &= r - I_\phi + T + c \cdot \left(\delta t_u - \delta t^s\right) + \lambda \cdot N + \lambda \cdot \varepsilon_\phi\end{aligned} \tag{2.3}$$

Differential techniques

Differential GPS surveying technique requires two or more GPS receivers to simultaneously track the same set of satellites. Based on this strategy, appropriate differential techniques have been developed to eliminate those biases common or linearly correlated across different observations to obtain GPS solutions. In the following, *single* and *double* differential processing for phase observations are given.

- *Single difference* (two different receivers tracking the same satellite) - eliminates the satellite clock offset (Misra and Enge, 2001):

$$\phi_{ij}^k = \lambda^{-1} \cdot r_{ij}^k + f \cdot \delta t_{ij} + N_{ij}^k + I_{ij}^k + T_{ij}^k + \varepsilon_{\phi,ij}^k \tag{2.4}$$

  where $(\bullet)_{ij}^k = (\bullet)_i^k - (\bullet)_j^k$; the superscript k denotes the kth satellite and the subscripts i and j donate the ith and jth receiver, respectively.

  When two receivers are within a short distance (e.g. < 10 km), $I_i^k = I_j^k$ and $T_i^k = T_j^k$ since both observation signals have a *proximately same* atmospheric path and I_{ij}^k and T_{ij}^k become zero. Under such condition, the model (2.4) becomes (Misra and Enge, 2001):

$$\phi_{ij}^k = \lambda^{-1} \cdot r_{ij}^k + f \cdot \delta t_{ij} + N_{ij}^k + \varepsilon_{\phi,ij}^k \tag{2.5}$$

- *Double difference* (*i.e.* difference either the between receivers or the between-satellite difference pairs (Figure 2.2)) - eliminate both the receiver and satellite clock offset.

The equation of double difference is (Misra and Enge, 2001):

$$\begin{aligned}\phi_{ij}^{kl} &= \phi_{ij}^{k} - \phi_{ij}^{l} \\ &= \lambda^{-1} r_{ij}^{kl} + N_{ij}^{kl} + I_{ij}^{kl} + T_{ij}^{kl} + \varepsilon_{\phi,ij}^{kl}\end{aligned} \tag{2.6}$$

where $(\bullet)_{ij}^{kl} = (\bullet)_{ij}^{k} - (\bullet)_{ij}^{l}$. In particular,

$$\phi_{ij}^{kl} = \left(\phi_{i}^{k} - \phi_{j}^{k}\right) - \left(\phi_{i}^{l} - \phi_{j}^{l}\right).$$

The model (2.6) for a short baseline between two receivers becomes

$$\begin{aligned}\phi_{ij}^{kl} &= \lambda^{-1} r_{ij}^{kl} + N_{ij}^{kl} + \varepsilon_{\phi,ij}^{kl} \\ &= \lambda^{-1}\left(r_{i}^{k} - r_{j}^{k} - r_{i}^{l} + r_{j}^{l}\right) + N_{i}^{k} - N_{j}^{k} - N_{i}^{l} + N_{j}^{l} + \varepsilon_{\phi,ij}^{kl}\end{aligned} \tag{2.7}$$

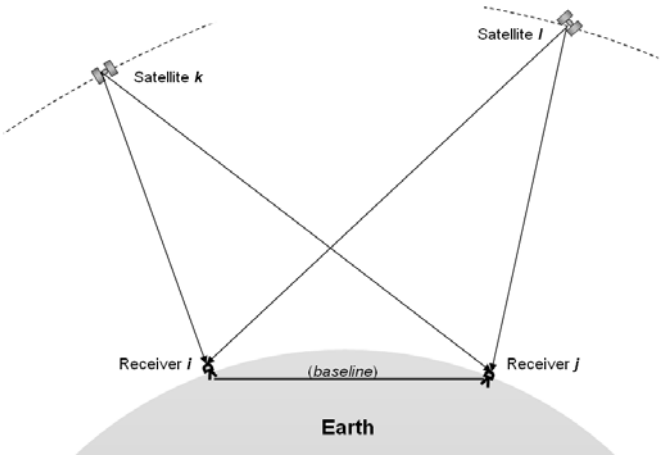

Figure 2.2 Configuration of two GPS receivers and two satellites with their corresponding ray paths
(The four observations are used to form on double difference observation. The straight line between two receivers is called baseline. (Adapted from (Kruse 2001)))

Error sources

Orbit error. This error is the discrepancy between the *true* position (and velocity) of a satellite and its *known* value. This discrepancy can be parameterized via the three orbit components: *alongtrack, crosstrack* and *radial*.

There are two basic types of satellite orbit information:

- Real-time ephemerides that are predicted from past tracking information, and are available to GPS users at the time of observation, and
- *Post-mission ephemerides*, which are orbit information available after fact as there is a delay for collection of the data, transmission of the data to the computer centre, the orbit determination process and the subsequent distribution to GPS users.

In this study, near real-time GPS data processing is utilized. Hereafter both predicted ephemerides and JPL real-time ephemerides correction data are used.

Satellite clock errors. These errors are satellite clock *bias*, *drift* and *drift-rate*, which are explicitly determined in the same procedure as the estimation of the satellite ephemeris and available to all GPS users as clock error coefficients broadcast in the Navigation Message.

In this study, PPP algorithm is utilized and the clock errors are ‘eliminated’ using real-time JPL satellite error correction data.

Receiver clock error. This error means the offset between the receiver clock and the GPS system time. Since GPS receivers use inexpensive crystal clocks, which are much less accurate than the satellite clocks, the receiver clock error is usually much larger than that of the GPS satellite clock. The receiver clock error leads to a range error in the pseudorange and carrier phase measurements. In this thesis, PPP algorithm is utilized and the receiver clock error is estimated.

Ionosphere delay. The GPS signals passing through the atmosphere encounter refraction effects including ray bending and propagation delays. Ionosphere delay is imparted by the ionosphere (thermosphere) which ranges from 80 to 1,500 km above the earth (Leick, 2004) and causes a significant range error. For day-time observations near solar maximum this effect can be tens of meters. Fortunately, the ionospheric delay is dispersive and can be reduced to a millimeter or less by forming particular linear combinations of the L1 and L2 code/phase measurements (*i.e.*, using dual-frequency observations) (Misra and Enge, 2001):

$$P_{IF} = \frac{f_{L1}^2}{\left(f_{L1}^2 - f_{L2}^2\right)} P_{L1} - \frac{f_{L2}^2}{\left(f_{L1}^2 - f_{L2}^2\right)} P_{L2} \tag{2.8}$$

and

$$\Phi_{IF} = \frac{f_{L1}^2}{\left(f_{L1}^2 - f_{L2}^2\right)} \Phi_{L1} - \frac{f_{L2}^2}{\left(f_{L1}^2 - f_{L2}^2\right)} \Phi_{L2} \tag{2.9}$$

where P_{IF} and Φ_{IF} are the *ionosphere-free* pseudorange and phase measurements, respectively; P_{L1}/Φ_{L1} and P_{L2}/Φ_{L2} are the pseudorange/phase measurement at L1 and L2 , respectively; f_{L1} and f_{L2} are the corresponding carrier frequencies. The linear combinations (2.8) and (2.9) eliminate the ionospheric effect, but may amplify other sources of error (Misra et al., 2001).

Troposphere delay. This delay is imparted by troposphere which is the lower part of atmosphere. Unlike ionosphere, troposphere is electically neutral and non-dispersive for GPS frequencies; therefore the delay can not be removed using dual-frequency relationship. The delay has to be measured, or estimated, from one of a number of models. Details on the tropospheric efftects and the corresponding methods of reduction will be discussed in later sections.

2.2 Effect of the troposphere on GPS Measurements

In this section, the nature of troposphere, how the neutral part of atmosphere affects the propagation of GPS signals, the nature of tropospheric effect and its size and variability, and the estimation of troposphere delays using GPS will be described.

2.2.1 Nature of the troposphere

The *troposphere* is the lowest major atmospheric layer, and is located from the Earth's surface up to the bottom of the *stratosphere* (Figure 2.3). It has decreasing temperature with height (at an average rate of 6.5 degrees C per kilometer); whereas the stratosphere has either constant or slowly increasing temperature with height. The thickness of the troposphere is not same everywhere. It extends to a height of less than 8 kilometers over the poles and exceeds 18 kilometers over the equator. The upper boundary of the stratosphere, called the *stratopause*, extends to a height of about 50 kilometers (S & TR, 2004).

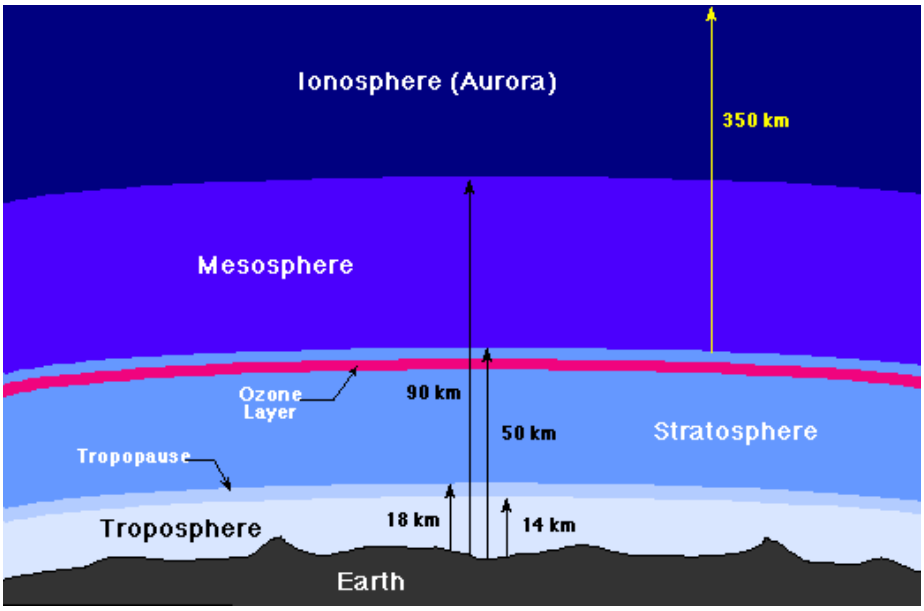

Figure 2.3 Layers of the Earth's atmosphere
(Cardall and Daunt, 2008)

The troposphere is denser than the layers of the atmosphere above it (because of the weight compressing it), and it contains up to 75% of the mass of the atmosphere. It is primarily composed of nitrogen (78%) and oxygen (21%) with only small concentrations of other trace gases. All atmospheric water vapor or moisture is found in the troposphere (Barry and Chorley, 2003).

The thin layer that divides the troposphere from the stratosphere is called the "tropopause", located at an altitude of around 8 km in the winter, to around 13 km high in the summer, and as high as 17 or 19 km in the deep tropics. Both stratosphere and troposphere layers are non-dispersive at radio frequencies below about 30 GHz because they are electrically neutral. Because 80% of the *neutral atmosphere* lies within the troposphere, the whole *neutral atmosphere* is commonly referred to as the "troposphere." (Brunner et al, 1993)

2.2.2 Nature of the tropospheric delay

As the GPS radio signals travels from satellite to receiver, it is affected by the atmosphere in two distinct ways (see Figure 2.4). First, the signals are bent with respect to in gradients in the index of refraction of the atmosphere, traveling along a curved path (S) instead a geometrical straight line (G) the signal would travel in a region of constant refractivity. The difference between the lengths of these two paths is known as the *geometrical delay*. Second, the speed of propagation of GPS signals is slower in a region of finite density than that in a vacuum. The increase in the time required to cover a given distance can also be expressed in terms of excess path length, yielding the optical delay. Both delays can be related to the variation of the refractive index, *n*, of the medium in the following manner (Yuan et al., 1993):

$$\Delta L = \int_L n(s) \cdot ds - G \tag{2.10}$$

where $n(s)$ is the refractive index as a function of position *s* along the curved path *L*, and *G* is the geometrical straight-line path length through the atmosphere. Because the index of refraction $n(s)$ is numerically close to unity, it is more conveniently expressed in terms of atmospheric refractivity (*N*) where

$$N(s) = \left[n(s) - 1 \right] \cdot 10^6 \tag{2.11}$$

Equation (2.10) can be expressed in terms of refractivity (Yuan et al., 1993):

$$\Delta L = 10^{-6} \int_L N(s) \cdot ds - (S - G) \tag{2.12}$$

where S is the curved path length along L. In this equation, the first term of the equation corresponds to optical delay and the second term corresponds to *geometrical delay*.

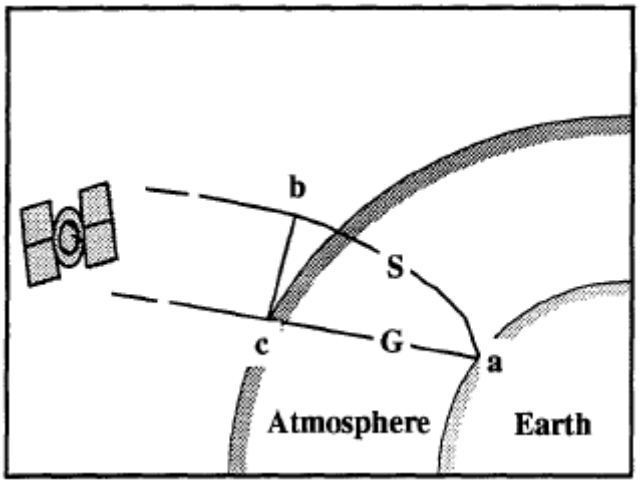

Figure 2.4 GPS Signal Geometry
(where G is the geometrical straight line the signal would travel in a region of constant refractivity and S is a curved path signal actually travels along due to the atmospheric refraction (Dodson et al., 1996))

To model the propagation delay one needs to develop a model to determine the integral along the line-of-sight to the satellite. The atmosphere is conveniently divided into two distinct strata: *ionosphere* and *troposphere* according to their natures and abilities to model the refractivity integral. The ionosphere is a dispersive medium at GPS signal frequencies and the delay imparted by it can be largely eliminated using dual-frequency observations (see Equation (2.8) and (2.9)). However, the troposphere is electrically *neutral atmosphere* which is a non-dispersive medium at GPS signal frequencies; therefore, the delay imparted by troposphere can not be eliminated by the linear combination of dual-frequency observations. The tropospheric delay has to be measured or estimated. The requirement of the model is the ability to estimate the integral of atmospheric refractivity along the line-of-sight.

The refractivity of the neutral atmosphere is a function of the local pressure, temperature, and water vapor content. The approximate expression for the refractivity is (Leick, 2004)

$$N(T, p_d, p_{wv}) = k_1 \cdot \frac{p_d}{T} \cdot Z_d^{-1} + k_2 \cdot \frac{p_{wv}}{T} \cdot Z_{wv}^{-1} + k_3 \cdot \frac{p_{wv}}{T^2} \cdot Z_{wv}^{-1} \tag{2.13}$$

where T is absolute temperature in degrees Kelvin, p_d is partial pressure of dry air in millibars, p_{wv} is partial pressure of water vapor in millibars, k_1, k_2 and k_3 are physical constants: $k_1 = 77.60 K/mbar$, $k_2 = 69.5 K/mbar$ and $k_3 = 370100 K^2/mbar$, Z_d and Z_{wv} are compressibility factors for dry air and water vapor, respectively. The first term expresses the sum of distortion of electro charges of the dry air molecules under the influence of an applied magnetic field. The second term accounts for the same effect but for water vapor. The third term accounts for the permanent dipole moments of the water vapor in the atmosphere; it is practically independent of frequency within GPS magnetic frequency (Leick, 2004).

Equation (2.13) is further developed by splitting the first term into two terms, one that represents refractivity of an ideal gas in hydrostatic equilibrium and another that is a function of the partial water vapor pressure. Thus the large hydrostatic (dry) constituent can be accurately computed using ground-based total pressure p $\left(p = p_d + p_{wv}\right)$. The smaller and more variable water vapor must be dealt with separately (Leick, 2004). The modified equation (2.13) becomes

$$N(T, p_d, p_{wv}) = k_1 \cdot R_d \cdot \rho + \left(k_2' \cdot \frac{p_{wv}}{T} + k_3 \cdot \frac{p_{wv}}{T^2} \right) \cdot Z_{wv}^{-1} \tag{2.14}$$

where R_d is dry air constant, ρ is the total density, $k_2' = k_2 - k_1 \cdot \frac{R_d}{R_{wv}} = k_2 - k_1 \cdot \frac{M_{wv}}{M_d}$, p_d and p_{wv} are the universal gas constant for ideal gas and water vapor, respectively, M_d and M_{wv} are the molar mass for ideal (dry) gas and water vapor, respectively.

In equation (2.14) the refractivity is clearly split into a dry component, *i.e.* dry refractivity N_d, and a wet component, *i.e.* water vapor refractivity N_{wv}:

$$N_d(T, p) = k_1 \cdot R_d \cdot \rho = k_1 \cdot \frac{p}{T} \tag{2.15}$$

$$N_{wv}(T, p_{wv}) = \left(k_2' \cdot \frac{p_{wv}}{T} + k_3 \cdot \frac{p_{wv}}{T^2} \right) \cdot Z_{wv}^{-1} \tag{2.16}$$

where $N = N_d + N_{wv}$. The hydrostatic refractivity N_d depends on total density ρ or the total pressure p. Figure 2.5 shows a typical height profile of N_d and N_{wv} as derived from radiosonde data (Brunner et al., 1993) where the shaded area indicates the overall variability of the wet component. Figure 2.5 reveals (1) that the variability of N_d is very small within the troposphere because the nearly constant ratio of the constituents of air, with the exception of water vapor and condensed water; (2) that the effective height for N_d is about 40 kilometers, above which N_d is negligible; (3) that the effective height for N_{wv} is at heights below the troposphere, within this region the mixing of dry air and water vapor is a rather complicated process depending on weather conditions. Thus the N_{wv} profiles show strong variations with height, time, and location and are very difficult to predict.

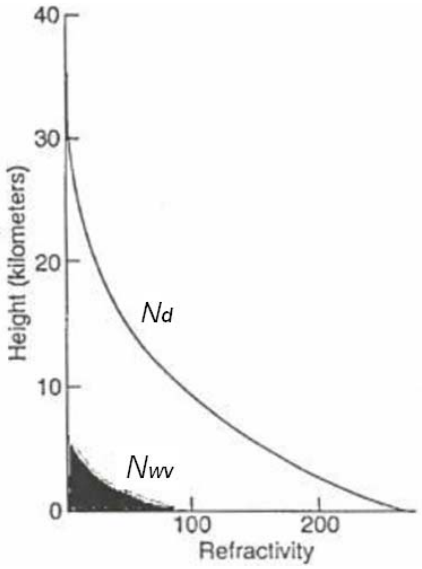

Figure 2.5 Typical height profiles of dry refractivity and water vapor refractivity
(where the shaded area indicates the overall variability of the wet component (Brunner et al., 1993))

Integrating (2.13) along the zenith direction using (2.15) and (2.16) gives the zenith hydrostatic (*dry*) delay (*ZHD* or *ZDD*) and zenith wet delay (*ZWD*), respectively,

$$ZDD = 10^{-6} \cdot \int N_d(s) \cdot ds \tag{2.17}$$

$$ZWD = 10^{-6} \cdot \int N_{wv}(s) \cdot ds \tag{2.18}$$

where zenith total delay $(ZTD) = ZDD + ZWD$. The hydrostatic refractivity N_d depends on the total pressure p ; if integrating N_d along the signal path then hydrostatic equilibrium condition to ideal gases is applied (Leick, 2004). The integration of N_{wv} is rather complicated due to the temporal and spatial variation of partial water vapor pressure p_{wv} along the path (Leick, 2004). Figure 2.6 shows a typical example of the variation of the tropospheric delays as a function of elevation angle to a GPS satellite. The shaded area indicates the *range* of water vapor delays. The total tropospheric delay effects are the sum of both curves in Figure 2.6. Figure 2.6 indicates that it should be possible to express the tropospheric delay at a certain elevation angle as the product of the tropospheric zenith delay and a function that maps the increase in delay with an increasing zenith angle.

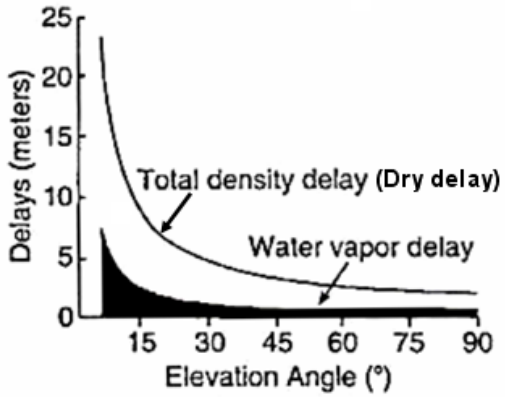

Figure 2.6 Propagation delays as a function of elevation angle
(Brunner et al., 1993)

2.2.3 Modeling zenith delays

Even though the hydrostatic refractivity N_d obeys the ideal gas law, performing integration (2.17) still requires *assumption* about the variation of temperature and gravity along the path (Leick, 2004). A successful solution for ZHD is Saastamoinen model,

which simplifies assumptions regarding changes in pressure, temperature, and humidity. The Saastamoinen's model is given as (Leick, 2004)

$$ZHD_{[m]} = \frac{0.0022768 \cdot p_{0[mbar]}}{1 - 0.00266 \cdot \cos(2\varphi) - 0.00028 \cdot H_{[km]}} \tag{2.19}$$

where p_0 is the total pressure at the site whose orthometric height is H and latitude is φ.

The model assumptions about the wet refractivity are much more difficult because of the strong variations of the water vapor with respect to time and space. There are some models for ZWD solutions such as Hopfield model, and Mendes and Langley model. The latter is presented below. Mendes and Langley model was derived based on the radiosonde data and the correlation analysis between the ZWD and the surface partial water vapor pressure $p_{vw,0}$. The model is (Leick, 2004)

$$ZWD = 0.0122 + 0.00943 \cdot p_{wv,0} \tag{2.20}$$

Since the tropospheric zenith wet delay *ZWD* is poorly correlated with surface meteorological data and the surface meteorological data are not necessarily representative of adjacent layers along the line of sight to the satellites, the derived *ZWD* models tend to be inadequate, offering poor results (Leick, 2004; Dodson et al., 1996).

As a remedy, meteorological data of a standard atmosphere has often been used. Such a standard atmosphere is referenced to sea-level and then using the height of the GPS site as the sole variable to calculate the meteorological values for a site. And so these values are independent of time and actual weather conditions. Excellent results have been found using standard atmospheric data as input for the Saastamoinen model in processing GPS data (Brunner et al., 1993).

2.2.4 Mapping functions

The models described above provide the solutions for tropospheric delays in the *zenith* direction. The satellites however are observed at numerous elevation angles (e). In fact, tropospheric delay increases with the zenith angle ϑ as the air mass traversed by the signal increases (see Figure 2.7). The exact functional relationship is again complicated by temporal and spatial variability of the troposphere. As Figure 2.7 indicates, it is possible to map a tropospheric delay from zenith down to slant path for the respective

elevation angles. The mapping function models this dependency, which provides an advantage for us to model or estimate a zenith delay for each site as an unknown parameter in the least-squares adjustment of GPS observations instead of delay values at all elevation angles (Brunner et al, 1993). The following functions show the relationship

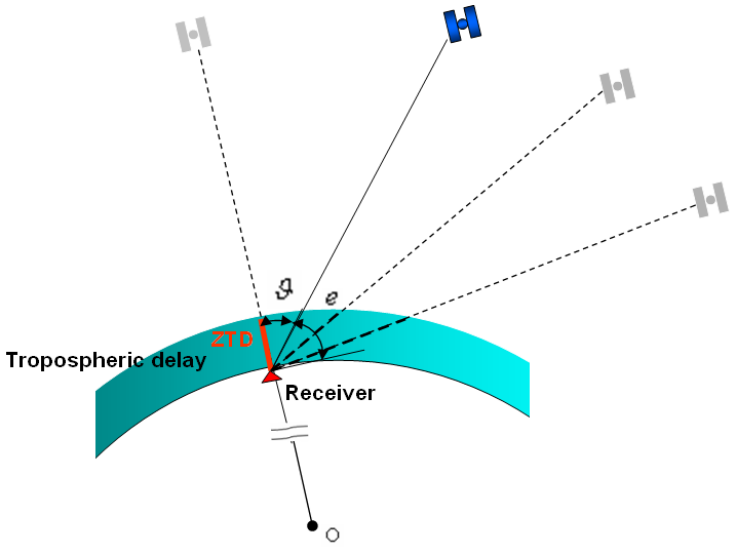

Figure 2.7 The path length of a signal through troposphere
(where ϑ is zenith angle and e is the elevation angle. The parts of rays highlighted in red represent schematically the different tropospheric delays, where the ZTD is the shortest one. (Adapted from (Misra and Enge, 2001))

between the slant hydrostatic (dry) and wet delays, SDD_i and SWD_i, and the respective zenith delays:

$$SDD_i = ZDD_i \cdot m_{d,i}(e) \tag{2.21}$$

$$SWD_i = ZWD_i \cdot m_{wv,i}(e) \tag{2.22}$$

The slant total delay (STD_i) is

$$STD_i = ZDD_i \cdot m^k_{d,i}(e) + ZWD_i \cdot m^k_{wv,i}(e). \tag{2.23}$$

In this study the popular Niell mapping functions are used, which are derived based on temporal changes and geographic location. Both the dry and wet mapping functions are given as below respectively (Leick, 2004):

$$m_d(e) = \frac{1 + \dfrac{a_{dry}}{1 + \dfrac{b_{dry}}{1 + c_{dry}}}}{\sin e + \dfrac{a_{dry}}{\sin e + \dfrac{b_{dry}}{\sin e + c_{dry}}}} + h \cdot \left(\frac{1}{\sin e} - \frac{1 + \dfrac{a_{ht}}{1 + \dfrac{b_{ht}}{1 + c_{ht}}}}{\sin e + \dfrac{a_{ht}}{\sin e + \dfrac{b_{ht}}{\sin e + c_{ht}}}} \right) \tag{2.24}$$

$$m_{wv}(e) = \frac{1 + \dfrac{a_{wet}}{1 + \dfrac{b_{wet}}{1 + c_{wet}}}}{\sin e + \dfrac{a_{wet}}{\sin e + \dfrac{b_{wet}}{\sin e + c_{wet}}}} \tag{2.25}$$

where e is the geometric elevation of the observation, h is the site height above sea level in kilometers, both a_{dry}, b_{dry}, c_{dry} and a_{wet}, b_{wet}, c_{wet} are hydrostatic and wet coefficients which are listed in the look-up Tables in Appendix A, a_{ht}, b_{ht}, c_{ht} are the height correction constants: $a_{ht} = 2.53 \times 10^5$, $b_{ht} = 5.49 \times 10^3$, *and* $c_{ht} = 1.14 \times 10^3$.

2.2.5 Stochastic path delay models

The water vapor in troposphere is variable in space and time which result in fluctuations in the wet delay (ZWD). If its spatial and temporal characteristics can be characterized by probabilistic laws or statistical models, then ZTD/ZWD can be predicted over varying spatial dimensions and temporal scales according to a given probability density function or stochastically in terms of the spatial and temporal correlations of the fluctuations (Tralli et al., 1990). Two appropriate models for stochastic path are *random walk* and *first-order Gauss-Markov processes*.

2.2.5.1 First-order Gauss-Markov process

The first-order Gauss-Markov process, expressing the change in the zenith wet delay (ZWD) with time (dt), can be defined by the differential equation (Tralli et al., 1990):

$$dZWD / dt = -ZWD(t) / \tau_{GM} + w(t) \tag{2.26}$$

where *w(t)* is a zero-mean white noise random variable of variance and τ_{GM} is the Gauss-Markov correlation time. The discrete solution to (2.26) is represented by (Tralli et al., 1990):

$$ZWD(t+\Delta t) = m \cdot ZWD(t) + (1 - m^2)^{\frac{1}{2}} \cdot w_{GM}(t) \tag{2.27}$$

where

$$m = exp(-\Delta t / \tau_{GM}) \tag{2.28}$$

The parameter, *m*, is a measurement of the exponential correlation between adjacent measurements of sampling interval Δt (in GPS, Δt donates the time difference between epochs $k + 1$ and k) and it can be obtained from

$$m \cdot [ZWD^2(t)] = [ZWD(t+\Delta t) \cdot ZWD(t)] \tag{2.29}$$

where [] denotes the expectation value operator; based on *m*, the Gauss-Markov correlation time, τ_{GM} , is obtained by

$$\tau_{GM} = -\frac{\Delta t}{\ln(m)} \tag{2.30}$$

Given *m*, the steady-state deviation of Gauss-Markov process, σ_{GM} , is obtained from (2.27)

$$\sigma_{GM} = \sqrt{\left[\frac{(ZWD(t+\Delta t) - m \cdot ZWD(t))^2}{(1-m^2)}\right]} \tag{2.31}$$

2.2.5.2 Random walk process

A random walk process is a defined simply by

$$dZWD/dt = w(t) \tag{2.32}$$

which is the same as equation (2.26) in the limit of an infinite correlation time ($\tau_{GM} = \infty$). The discrete solution to equation (2.32) is given by

$$ZWD(t+\Delta t) = m \cdot ZWD(t) + \sqrt{\Delta t \cdot w_{rw}} \tag{2.33}$$

Hence, the deviation for random walk process is

$$\sigma_{rw} = \sqrt{\left[\frac{\left(ZWD(t+\Delta t) - ZWD(t)\right)^2}{\Delta t}\right]} \tag{2.34}$$

The random walk deviation actually is the reverse ratio of the sampling interval. It can grow indefinitely and therefore is not steady-state.

Zenith delays (ZDD or ZWD) can be modeled either as *Gauss-Markov process* entirely with parameters of the steady-state deviation (σ_{GM}) and correlation time (τ_{GM}), or as *random walks process* based solely on the process noise rates (σ_{rw}). According to the limit of infinite or large correlation time relative to data sampling interval Δt, modeling the tropospheric delays as a Gauss-Markov process becomes equivalent to modeling as a random walk process. Since the first-order Gauss-Markov process is of zero mean, a constant term is estimated jointly as an additional parameter (Tralli et al., 1990). An advantage with the Gauss-Markov model is that the direct comparison can be made among constant delay models to evaluate the marginal improvement to the parameter estimates especially attributable to modeling the path delay fluctuations (Tralli et al., 1988). A random walk process, in the limit of decreasing process noise, approaches a constant constrained by an a priori deviation specified according to the expected path delay at the start of the process. This *a priori* deviation is analogous to the constraint imposed on the constant term which is estimated jointly with Gauss-Markov process (Tralli et al., 1990).

Stochastic model parameters values such as σ_{GM}, τ_{GM} and σ_{rw} could be initially from the data by fitting a sample mean and sample autocorrelation function.

2.2.6 Estimating zenith delays

The standard atmospheric model helps obtain accurate meteorological data, but it fails to describe the meteorological conditions at a GPS site during a particular observation session (Dodson et al., 1996).

Least-squares adjustment technique can be used to solve for the entire tropospheric zenith delay, or the tropospheric wet delay (the dry tropospheric zenith delay is then modeled from barometric pressure alone) for each GPS station.

For simplicity, equation (2.23) will be considered as:

$$STD_i = ZTD_i \cdot m^k_{combined,i}(e), \tag{2.35}$$

where

$$m^k_{combined,i}(e) = \frac{ZDD_i \cdot m^k_{d,i}(e) + ZWD_i \cdot m^k_{wv,i}(e)}{ZDD_i + ZWD_i} \tag{2.36}$$

Then the tropospheric delay is estimated as part of the least-squares procedure using the double-difference observation, *i.e.*,

$$\Phi^{kl}_{ij} = \rho^{kl}_{ij} - \lambda \cdot N^{kl}_{ij} + ZTD_j \cdot \left(m^l_j - m^k_j\right) - ZTD_i \cdot \left(m^l_i - m^k_i\right) \tag{2.37}$$

Usually an unknown troposphere zenith delay is estimated per site and session. Such a model tends to average any variations of the troposphere zenith delay. The problem with this technique is that it can not model certain error sources within the system such as ocean loading effects, the wet tropospheric delay fluctuation (Brunner et al., 1993; Dodson et al., 1996).

An alternative is to model the troposphere zenith delay by a stochastic model (see Section 2.2.5), which treats the unknown troposphere zenith delay as a time-varying parameter. The mathematical adjustment is performed with a sequential Kalman filter (see Figure 2.8).

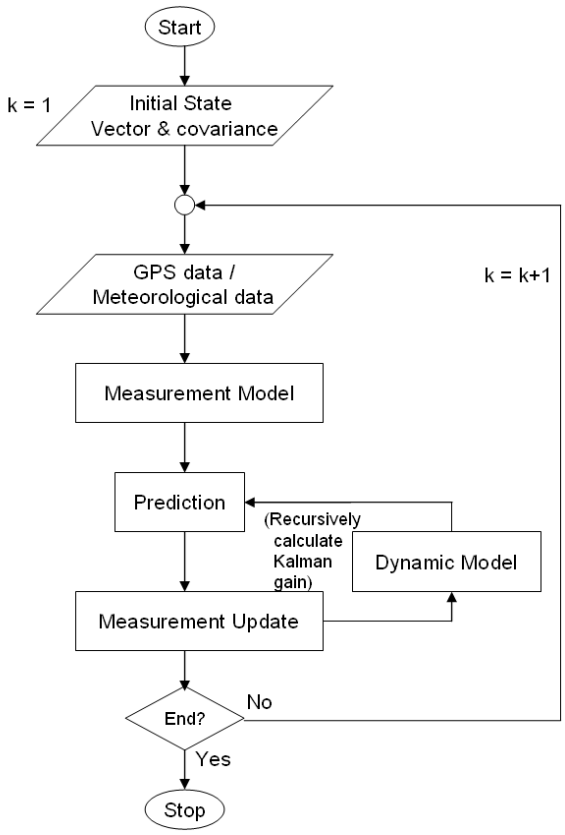

Figure 2.8 Programming diagram for Kalman filter parameter estimation

The Kalman filter is designed to produce minimum error estimation for a system. The development of Kalman filter needs to concern the initial state of the system, the system dynamics, the measurement dynamics and assumptions of system noise and measurement errors (Gelb, 1974).

2.2.7 Zenith wet delay conversion into precipitable water vapor

Zenith wet and precipitable water vapor (PWV) are related by:

$$Q = \frac{ZWD}{PWV} \tag{2.38}$$

where Q is a dimensionless conversion factor and its value varies between $5.9 \sim 6.5$, depending on the air temperature (Leick, 2004). For warmer conditions, when the air holds more water vapor, the ratio is toward the low end.

A ground receiver can have simultaneous observations along 4-12 ray paths. GPS sensed PWV is modeled using an average of *all* observed GPS rays after they have been scaled to zenith, as shown in Figure 2.9.

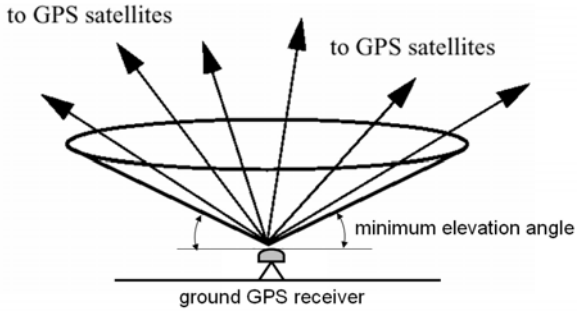

Figure 2.9 Schematic presentation of GPS PWV
(GPS PWV is modeled as an average of all GPS satellite observations above the minimum elevation angle represented by the cone. The cone is the maximum angle aperture of the GPS antenna) (Adapted from Ware et al. (1997))

2.3 GPS sensing techniques

In terms of source of the GPS data for meteorological application, there are two primary methods by which GPS data can be used for sensing the properties of atmospheric water vapor (Bevis et al., 1992; Yuan et al., 1993).

2.3.1 Mapping precipitable water vapor using existing geodetic GPS networks

This technique utilizes stationary ground-based receivers, which originally are developed for high-precision geodetic applications (see Figure 2.10). It is achieved in two steps: accurately modeling all GPS signal delays, including the delay caused by the Earth's atmosphere, and then adopting the stochastic filter and other statistical techniques to recover the zenith wet delay from GPS data. Afterwards, it is possible to estimate the PWV from observed zenith wet delay (based on (2.3)). Given a sufficient dense network of GPS receivers, it would be possible to map the distribution of PWV in some detail (Bevis et al, 1992). This study is based on this technique, i.e., GPS PPP technique plus a continuously operating GPS geodetic network.

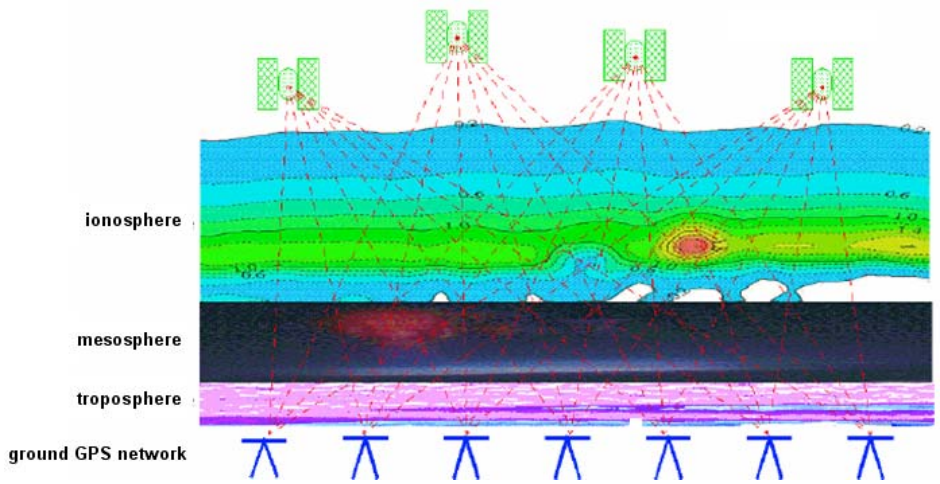

Figure 2.10 Retrieve water vapor using geodetic GPS network
(Ware et al., 2001)

2.3.2 Space-based GPS occultations

This technique means to obtain GPS soundings of the atmosphere by means of readings from the GPS transmitter to a low Earth orbit (LEO) satellite (Figure 2.11). (Radio) Occultation techniques have been applied for decades to explore and measure atmospheric properties of other planets in the solar system. With the advent of GPS it is regarded a valuable means to obtain profiles of refractivity, temperature, pressure, and water vapor in the neutral atmosphere and electron density in the ionosphere. In April 1995, the GPS Meteorology (GPS MET) experiment, which placed a GPS receiver in a low earth orbit (LEO), provided a wealth of data which was used to test this concept and the accuracy of the retrievals. Several investigations have already demonstrated that the retrieval accuracies obtained with GPS/MET is already comparable with the more traditional atmospheric sensing techniques (Kursinski et al., 2001).

To extract atmosphere information from the LEO data, first the orbit of LEO must be determined. This task can be achieved using GPS data from the LEO. Once the LEO – GPS configuration is known accurately, the GPS measurements of an occulting LEO can be interpreted in terms of atmospheric delay. This delay is caused by both the neutral atmosphere and the ionosphere. The ionosphere effect can be corrected using dual frequency signals from the GPS satellites; however, for LEO observations where the two frequencies travel along paths, separated by several 100 m, there is an ionosphere

correction error of 1 m or more. *Brunner* and *Gu* (1991) describes how path separation effects may be compensated in order for GPS occultation work to achieve the highest accuracy possible (Yuan et al., 1993).

Radio Occultation measurements using GPS and a receiver on a LEO have recently been shown to produce accurate profiles of Atmospheric refractivity with high vertical resolution (Yuan et al., 1993).

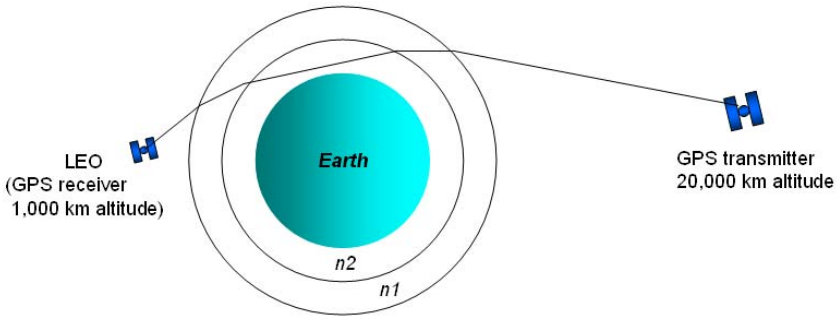

Figure 2.11 Schematic diagram for GPS occultation geometry for path delay calculation (where ray paths through two (exaggerated) atmospheric layers with indices of refraction n1 and n2 are shown) (Adapted from: http://www.cpar.qinetiq.com/ro.html)

2.4 Summary

This chapter has presented an overview of the GPS technique, the neutral atmospheric effects on radio frequency signals and the GPS meteorological applications.

GPS meteorology is the application of GPS data to the monitoring and analyses of atmospheric conditions. The use of GPS observations to estimate the precipitable water vapor is based on the fact that the atmospheric water vapor introduces additional delay (range error) to GPS observables as the GPS signals travel through neutral atmosphere. To obtain the high positioning precision this delay has to be modeled or estimated by a time-varying zenith wet delay (ZWD) which is retrieved by stochastic filtering of the GPS data. Given surface temperature and pressure at the GPS receiver, the retrieved ZWD can be transformed into an estimate of the precipitable water vapor (PWV).

GPS atmospheric remote sensing based on the ground-based GPS networks has two advantages: (i) providing unattended, continuous, independent, frequent, and accurate

observations of IPW/PWV at very low cost, and (ii) providing all-weather-condition observations.

The GPS meteorological applications have been mainly developed in three areas: *mapping of IWV/PWV using existing geodetic GPS networks* (*ground-based*), *tropospheric water vapor tomography using meteorological GPS networks* (*ground-based*), and *GPS occultation observed from space* (*space-based*).

In the following chapter, the precise point positioning (PPP) model which is adopted in this thesis will be presented.

Chapter Three: GPS PPP Water Vapor Determination Model

3.1 Introduction

In the previous chapter, the GPS remote sensing theory was represented. The most commonly used technique for water vapor remote sensing is DGPS. The DGPS approach requires at least two receivers simultaneously observing common GPS satellites and it uses the double-difference observations to eliminate common satellite and receiver errors. While the DGPS provides accurate positioning results, it has some drawbacks when it is used to measure atmospheric water vapor. *First*, its precision is related to the baseline length between the base and rover GPS receivers (Rocken et al., 1993; Zhang, 1999). *Next*, its solution is a relative estimate of the water vapor (for shorter baselines). *Third*, its operation requires data communication and synchronization between the network receivers to facilitate double difference baseline processing. An alternative to the DGPS approach is the Precise Point Positioning (PPP) technique.

The PPP is a concept of GPS positioning using data from a single GPS receiver and precise satellite orbit and clock information generated by the International GNSS Service (IGS). To achieve the highest possible point positioning accuracy to match DGPS solution, PPP uses ionosphere-free, undifferenced code pseudorange and carrier-phase measurements. In addition, the remaining errors such as tropospheric delay, satellite attitude error and site displacement effect due to such as solid Earth tides are dealt with by modelling or estimation. This technique has been demonstrated that carrier-phase-based single point positioning can achieve decimetre or sub-decimetre accuracy levels without the need for processing any GPS reference station data (Gao et al., 2001; Kouba et al., 2001).

The next two sections will present the PPP water vapor determining model employed in this thesis and the related PPP correction models.

3.2 PPP water vapor determination model

3.2.1 Observation equations

The ionospheric-free combinations of dual-frequency GPS pseudorange and carrier-phase obaservations are respectively given below (Gao et al., 2004):

$$P_{IF} = \frac{f_1^2 \cdot P_1 - f_2^2 \cdot P_2}{f_1^2 - f_2^2}$$

$$= \rho + c \cdot dt + d_{trop} + dm_{IF} + \varepsilon(P_{IF}) \tag{3.1}$$

$$\Phi_{IF} = \frac{f_1^2 \cdot \Phi_1 - f_2^2 \cdot \Phi_2}{f_1^2 - f_2^2}$$

$$= \rho + c \cdot dt + d_{trop} + \frac{c \cdot f_1 \cdot N_1 - c \cdot f_2 \cdot N_2}{f_1^2 - f_2^2} + \delta m_{IF} + \varepsilon(\Phi_{IF}) \tag{3.2}$$

where

P_i is the measured pseudorange on L_i (m), *i = 1 or 2*;

Φ_i is the measured carrier phase on L_i (m), *i = 1 or 2*;

f_i is the carrier frequency of L_i, *i = 1 or 2*;

ρ is the true geometric range (m);

c is the speed of light (m/s);

dt is the receiver clock error (s);

d_{trop} is the tropospheric delay (m);

N_i is the integer phase ambiguity on L_i (cycle), *i = 1 or 2*;

dm_{IF} is the multipath effect in the measured pseudorange on L_i (m);

δm_{IF} is the multipath effect in the measured carrier phase on L_i (m);

$\varepsilon(\cdot)$ is the measurement noise (m);

3.2.2 Tropospheric delay estimation

In Equation 3.2, the *slant* tropospheric delay d_{trop} can be represented using the following form (Leick, 2004):

$$d_{trop} = m_d(e) \cdot ZDD + m_{wv}(e) \cdot ZWD \tag{3.3}$$

where

ZDD, ZWD are the zenith dry and wet delay, respectively;

$m_d(e)$ is the dry mapping function;

$m_{wv}(e)$ is the wet mapping function;

e is the elevation angle.

In this study, ZDD is modeled using the Saastamoinen's model (Equation 2.19); ZWD is estimated using the first-order Gauss-Markov process described in Section 2.2.5. $m_d(e)$ and $m_{wv}(e)$ are the dry (Equation 2.24) and wet (Equation 2.25) Niell mapping functions, respectively.

3.3 Precise point positioning correction models

Unlike in relative positioning, common errors can not be cancelled in PPP. The corrections for these errors must be applied to the observations.

3.3.1 Satellite ephemeris and clock errors

The GPS navigation accuracy specification calls for a 16m 50% Spherical Error Probable (SEP) and a 100m 95% 2drms, for the PPS and SPS systems, respectively (Warren et al., 2003). Errors associated with satellite are ephemeris and satellite clock phase error (wrt GPS time). Both of these errors are uncertainties. The magnitude of the former is ~2 m and the magnitude of the latter is 7 ns. The effects of these errors depend on the type of the GPS processing techniques that is being used. IGS provides precise GPS ephemerides and adjusted clock parameters. Such a service is accomplished through a globally distributed tracking stations equipped with continuously operating dual frequency

receivers (see Figure 3.1). Positions and velocities are given for every 15 minutes, and clock parameters for every 5 minutes. Table 3.1 gives the IGS precise data in different latencies and intervals and their characteristics. Use of the IGS Rapid or Final products reduces the uncertainty of satellite orbit and clock and achieves high level of accuracy. The drawback of this precise data is the availability at some latency at present.

NASA JPL (Jet Propulsion Laboratory) has developed a model for predicting ephemeris and satellite clock correction, which makes the real-time PPP applications possible. For the JPL real-time precise correction products, the data sample intervals for ephemeris and clock are 1 second and 31 seconds, respectively. This study uses JPL real-time precise correction to implement PPP algorithm, which are sent to the University of Calgary in a real-time data stream using UDP (User Datagram Protocol) via the Internet.

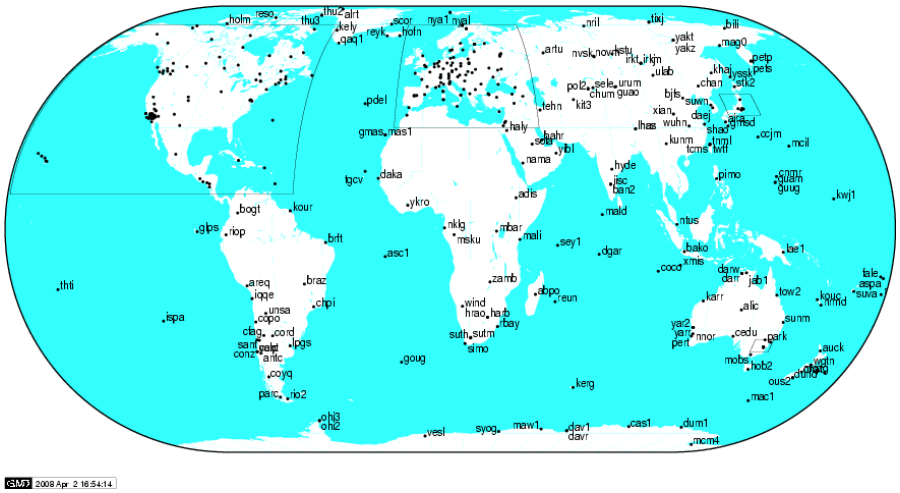

Figure 3.1 IGS network of globally distributed tracking sites
(from:http://igscb.jpl.nasa.gov/network/complete.html)

Table 3.1 IGS combined orbit and clock products and their characteristics compared with broadcast values (Ray et al., 2005)

GPS satellite ephemerides and satellite/station clocks		Accuracy estimates	Latency	Update intervals	Sample interval
Broadcast	Orbits	~200 cm	Real time	—	Daily
	Sat. clocks	~7 ns			
Ultra-Rapid (predicted half)	Orbits	~10 cm	Real time	Four times daily	15 min
	Sat. clocks	~5 ns			
Ultra-Rapid (observed half)	Orbits	<5 cm	3 h	Four times daily	15 min
	Sat. clocks	~0.2 ns			
Rapid	Orbits	<5 cm	17 h	Daily	15 min
	Sat. & stn. clocks	~0.1 ns			5 min
Final	Orbits	<5 cm	~13 days	Weekly	15 min
	Sat. & stn. clocks	~0.1 ns			5 min

3.3.2 Satellite antenna phase center offset

This offset is caused by the separations between the GPS satellite center of mass and the antenna phase center. Since satellite antenna broadcasts its signals, all measurements are made to the antenna phase centers. The IGS uses dynamic modeling for estimating the GPS orbit and the resulting orbital data refers to the center of mass (Figure 3.2).

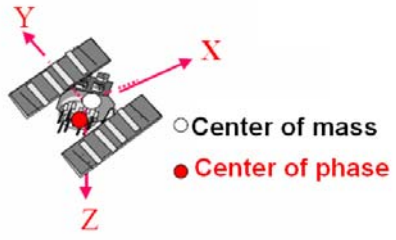

Figure 3.2 Satellite antenna phase center offset
(where the z-axis points toward the Earth center; the x-axis points along the solar panel axis, the y-axis completes the right-handed coordinate system and lies in the Sun-satellite Earth plane. (Kouba et al., 2001))

Starting on 1998-Nov-29 (GPS Week 986, day 0) the IGS products incorporated the antenna phase center offsets given in Table 3.2. The correction of this error can be done in Equation 3.4 (Leick, 2004):

$$X_{\text{phase\_center}} = X_{\text{mass\_center}} + \left[\vec{i} \quad \vec{\text{j}} \quad \vec{\text{k}}\right]^{-1} X \tag{3.4}$$

where X_{phase_center} is the position of the satellite antenna (i.e. phase center); X_{mass_center} is the position of the satellite's center of mass; $\left[\vec{i} \ \vec{\text{j}} \ \vec{\text{k}}\right]$ is satellite body local *unit matrix*, $\vec{i} = [1 \ 0 \ 0]^T$ is satellite-Sun unit vector in Earth Centered Earth Fixed (ECEF), $\vec{k} = [0 \ 0 \ 1]^T$ is satellite unit vector toward Earth in ECEF, $\vec{j} = [0 \ 1 \ 0]^T$ is the third vector of $\vec{i}$ and $\vec{k}$ which completes the right hand system, $X = \left[x_{offset} \ y_{offset} \ z_{offset}\right]^T$, which is offset in the satellite fixed coordinates system.

Table 3.2 GPS satellite antenna phase center offset (*X*) adopted by IGS
(Block II/IIA and IIR are different prototype of satellites) (Kouba et al., 2001)

	x_{offset} (m)	y_{offset} (m)	z_{offset} (m)
Block II/IIA	0.279	0.000	1.023
Block IIR	0.000	0.000	0.000

3.3.3 Phase wind-up error

GPS satellites transmit right circularly polarized (RCP) radio wave and therefore, the observed carrier-phase depends on the mutual orientation of the satellite and the receiver. Any relative rotation between satellite antenna and receiver antenna will change the carrier-phase up to one cycle, which corresponds to one complete revolution of the antenna. When using GPS carrier phase observations, any relative orientation during the observation period must be corrected by the following equations (Wu et al., 1993; Leick, 2004):

$$d = \hat{x} - k(k \cdot \hat{x}) + k \times \hat{y} \tag{3.5}$$

$$d' = \hat{x}' - k(k \cdot \hat{x}') + k \times \hat{y}' \tag{3.6}$$

$$\delta\varphi = sign\left[k \cdot \left(d' \times d\right)\right] \cdot \cos^{-1}\left(\frac{d' \cdot d}{\|d'\| \cdot \|d\|}\right) \tag{3.7}$$

where $\hat{x}$, $\hat{y}$, $\hat{z}$ are the satellite body local unit vectors (as in satellite antenna phase offset), $\hat{x}'$, $\hat{y}'$, $\hat{z}'$ are the receiver local unit vector, k is the unit vector pointing from satellite to receiver, $\|d\|$ is the magnitude of the vector, $\delta\varphi$ is the phase wind-up correction.

3.3.4 Solid Earth tides

The Earth as a whole responds to external forces as an elastic body. Solid earth tides are caused by the gravitational force exerted by the sun and moon. The caused effect is the periodic deformation of the solid Earth, *i.e.* vertical and horizontal site displacement, by

decimetre level. The effective values of displacements weakly depend on station latitude and tide frequency and need to be taken account. The solid earth tide is corrected by the following equation (Kouba and Heroux, 2001):

$$\Delta\vec{r} = \sum_{j=2}^{3} \frac{GM_j}{GM} \cdot \frac{r^4}{R_j^3} \left\{ \left[3 \cdot l_2 \left(\hat{R}_j \cdot \hat{r} \right) \right] \cdot \hat{R}_j + \left[3 \left(\frac{h_2}{2} - l_2 \right) \left(\hat{R}_j \cdot \hat{r} \right)^2 - \frac{h_2}{2} \right] \cdot \hat{r} \right\}$$
$$+ \left[-0.025 \cdot \sin\phi \cdot \cos\phi \cdot \sin\left(\theta_g + \lambda \right) \right] \cdot \hat{r} \,, \qquad (3.8)$$

where GM, GM_j are the gravitational parameters of the Earth, the Moon (j = 2), and the Sun (j = 3); r, R_j are geocentric distances of the station, the Moon, and the Sun with the corresponding unit vector $\hat{r}$ and $\hat{R}_j$, respectively; l_2 and h_2 are the nominal second-degree Love and Shida dimensionless numbers (0.609, 0.085); ϕ and λ are the site latitude and longitude and θ_g is Greenwich Mean Sidereal Time.

The tidal correction in (3.8) reaches ~30 cm in the radial and ~5 cm in the horizontal direction (Kouba and Heroux, 2001).

3.3.5 Ocean loading

The ocean loading is primarily vertical variation of the crust in primarily coastal areas, which is caused by sea level fluctuations due to the tides. These changes may cause a surface displacement of 5 cm in the vertical and 2 cm in the horizontal direction. Tidal ocean loading should be taken into account in space geodesy observations when precision better than 4 cm is required and when the tropospheric zenith path delay or clock solutions are required, unless the station is far (>1,000 km) from the nearest coast line. The ocean load effects can be modeled in each principal direction by the following correction term (Kouba and Heroux, 2001):

$$\Delta c = \sum_j f_j \cdot A_{cj} \cos\left(\omega_j \cdot t + \chi_j + u_j - \Phi_{cj} \right) \qquad (3.9)$$

where f_j and u_j depend on the longitude of lunar node (at 1 ~ 3-mm precision $f_j = 1$ and $u_j = 0$); $\sum_j (\cdot)$ represents the 11 tidal waves designated as M_2, S_2, N_2, K_2, K_1, O_2, P_2, Q_1, M_f, M_m, and S_{sa}; ω_j and χ_j are the angular velocity and the astronomical arguments at time t = 0 h, corresponding to the tidal wave component j; A_{cj} is the station specific amplitude; Φ_{cj} is the station specific phase.

3.3.6 Atmospheric tides

Atmosphere tides fundamentally affect the ocean and Earth tides in an indirect way. Sea level is affected as a result of atmospheric pressure variations. Spatial and temporal variations of atmospheric mass deform the Earth's surface. The magnitude of the effect can be up to ~20 mm (Tregoning et al., 2005). A simplified form for vertical displacement correction (mm) is (Rabbel et al., 1986):

$$\Delta r = -0.35 \cdot p - 0.55 \cdot \overline{p} \tag{3.10}$$

where Δr is the atmosphere pressure load displacement (mm); p is site pressure difference from the standard value (101.3 KPA); $\overline{p}$ is the average pressure anomaly within 2000 km radius surrounding the site.

3.3.7 Relativity

The clocks in satellites are subject to two relativistic effects. According to the Special Theory of Relativity, a clock in satellite traveling at a constant speed would appear to tick slower than a clock on the ground due to the time dilation effect of their relative motion. According to the General Relativity, a clock located farther away a massive object (*i.e.* a clock in satellites) will seem to run faster than ones on the ground (*i.e.* ground receiver clocks) due to the difference in gravitational potential. The correction for the first effect is suggested in the ICD-GPS_200C:

$$\Delta t_r = \frac{2}{c^2} \cdot \vec{r}^{\,s} \cdot \vec{v}^{\,s} \tag{3.11}$$

where Δt_r is the relativity correction; $\vec{r}^{\,s}$ and $\vec{v}^{\,s}$ are position and velocity of a GPS satellite; c is the speed of light.

The correction for the second effect is (Rothacher et al., 2002):

$$\Delta t_p = \frac{2GM_E}{c^2} \ln\left(\frac{r^s + r_r + r_r^s}{r^s + r_r - r_r^s}\right) \tag{3.12}$$

where Δt_p is gravity delay error; G is gravitational constant; M_E is mass of the earth; r^s is distance between the satellite and earth center; r_r is distance between the receiver and earth center; r_v^s is distance from the receiver to satellite.

The above correction models have been implemented in the P^3 software.

3.4 Summary

GPS water vapor sensing can be performed by either of two ways: DGPS or PPP. The former employs two (or more) GPS receivers simultaneously tracking the same satellites and the latter employs one GPS receiver. While DGPS provides accurate solutions, its performance is dependent on the inter-station distances. Through the use of ionosphere-free, undifferenced code pseudorange and carrier-phase measurements with precise satellite orbit and clock parameters and other error models, PPP can provide the high accurate point positioning solutions to match the DGPS solution. Since PPP performs single receiver station based data processing, PPP water vapor sensing technology can be efficiently implemented in all kinds of GPS tracking site configurations.

Chapter Four: System Design and Implementation

The real-time GPS PPP-inferred water vapor system development starts with the system design. In this chapter, the initial conditions and system requirements are discussed firstly and then the system design and implementation are illustrated.

4.1 Initial conditions and system requirements

4.1.1 Initial conditions

The initial conditions of this study are presented below.

4.1.1.1 Canadian geodetic (GPS) network

The present Canadian geodetic GPS network has been constructed during the last decade and is now operated by Natural Resources Canada (NRCan). It consists of 35 continuously operating GPS stations. 20 of the 35 stations are equipped with collectable surface weather stations which collect and record the meteorological (MET) data such as pressure, temperature and relative humidity, and 21 of the 35 stations send raw GPS data stream in real-time. Figure 4.1 shows the distribution of the 21 GPS stations with their coordinate information provided in Table 4.1. The system is developed based on this 21-real-time-GPS-station network. The raw GPS/MET data collection and management within the network is done through RTIGSA (Real-Time IGS Archive) software, which is developed in C++ by NRCan. RTIGSA is executed under LINUX environment and it does the following tasks (NRcan, 2005):

- Listening to the RTIGS format data steam from the GPS stations,
- Validating the RTIGS messages,
- Saving the RTIGS data in files, and
- Multicasting the GPS/MET data on the subnet so that it is available to many users.

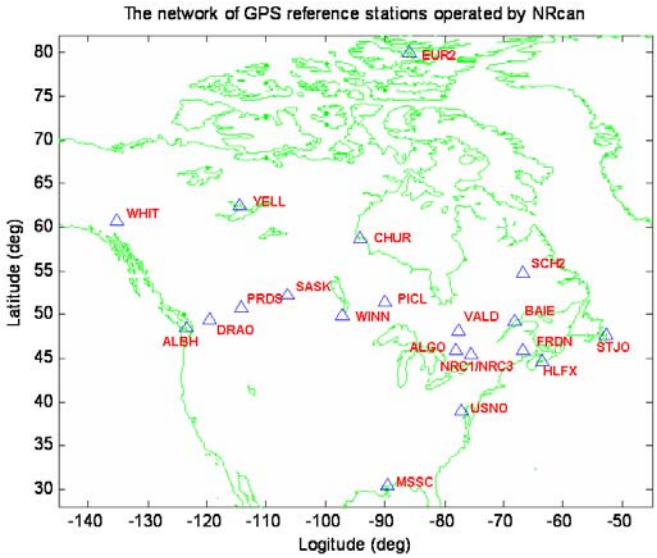

Figure 4.1 Canada (geodesy) GPS network operated by NRCan
(The network consists of 21 continuously operating GPS stations which send raw GPS data in real-time, 19 of 21 stations (except for USNO and MSSC) send real-time MET data stream, too.)

Table 4.1 Network GPS station ID and coordinates

GPS site ID / name	Lat (deg)	Lon (deg)	Height (m)
ALBH / VICTORIA	48.39 N	123.49 W	32.06
ALGO / ALGONQUIN PARK	49.90 N	78.07 W	201.97
BAIE / BAIE-COMEAU	49.18 N	68.26 W	28.48
CHUR / CHURCHILL	58.76 N	94.10 W	-18.87
DRAO / PENTICTON	49.32 N	119.63 W	542.24
EUR2 / EUREKA	79.99 N	85.94 W	28.68
FRDN / FREDERICTON	45.93 N	66.66 W	95.96
HLFX / DARTMOUTH	44.68 N	63.61 W	4.28
MSSC / MISSISSIPPI	30.38 N	89.61 W	-13.00
NRC1 / OTTAWA	45.45 N	75.62 W	83.59
NRC3 / OTTAWA	45.45 N	75.62 W	83.59
PICL / PICKLE LAKE	51.48 N	90.17 W	315.87
PRDS / CALGARY	50.87 N	114.28 W	1248.39
SASK / SASKATOON	52.18 N	106.38 W	579.44
SCH2 / SCHEFFERVILLE	54.83 N	66.83 W	499.03
STJO / ST. JOHN'S	47.60 N	52.68 W	153.89
USNO / COLUMBIA	38.92 N	77.06 W	50.17
VALD / VAL D'OR	48.09 N	77.56 W	313.77
WHIT / WHITEHORSE	60.75 N	135.22 W	1427.23
WINN / WINNIPEG	49.90 N	97.25 W	221.11
YELL / YELLOWKNIFE	62.48 N	114.48 W	181.03

4.1.1.2 Precise satellite orbit and clock correction data

Jet Propulsion Laboratory (JPL) has developed a program to distribute the real-time precise ephemeris correction products through the Internet. The University of Calgary is granted to retrieve the data using User Datagram Protocol (*UDP*) protocol via Internet.

4.1.1.3 Meteorological (MET) data

At present, real-time MET data stream is not available in real-time stream. NRCan provides one-hour-latency MET data files through its FTP file server on Internet.

4.1.1.4 GPS software sources

A PPP software product P^3 was developed at the University of Calgary, which runs in both post-mission and real-time mode under MS Window environment. Under the static real-time processing condition, PWV estimate at about 1 mm accuracy level has been demonstrated using the software P^3 (Gao et al., 2004). P^3 will be the core function unit for calculating water vapor in this real-time system, but it needs to be adapted for concurrent real-time *multi-station* data processing since the real-time raw data stream contains 21 station GPS and observation data.

NRCan offers an open source: RTIGSMR (Real-Time IGS Multicast Receiver) software, which is a framework developed in C++ and run on LINUX platform. RTIGSMR does the following (NRCan, 2005):

- Listens to the broadcast multicast, and
- Decodes the RTIGS messages.

Since RTIGSMR is a framework, some LINUX system functions of it can be replaced with the corresponding MS Windows system functions or with the user's developed functions and then it can be applied to Microsoft Windows platform.

4.1.2 System-level requirements

Based on the system goals and development conditions stated above, the system-level requirements are specified as below:

- A GPS network is needed with receiver stations distributed over Canada;
- Real-time precise orbit and clock correction data is needed to support PPP data processing;
- Data communication between the GPS data processing center (at the University of Calgary) and RTIGSA (at the NRCan) via multicast IP address and port;
- Data communication between the GPS data processing center (at the University of Calgary) and the JPL precise data server via UDP IP address and port;
- Concurrent multi-station GPS data processing;
- Produce near real-time estimated PWV data for each individual station;
- Store/output the station daily/hourly log files to Web data server/FTP server; and
- Produce/output near real-time hourly PWV distribution map.

4.2 System design

The architecture of the system design is shown in Figure 4.2. The whole system comprises five functional components (subsystems). Each of the components has its own allocated function and is organized to cooperate with each other.

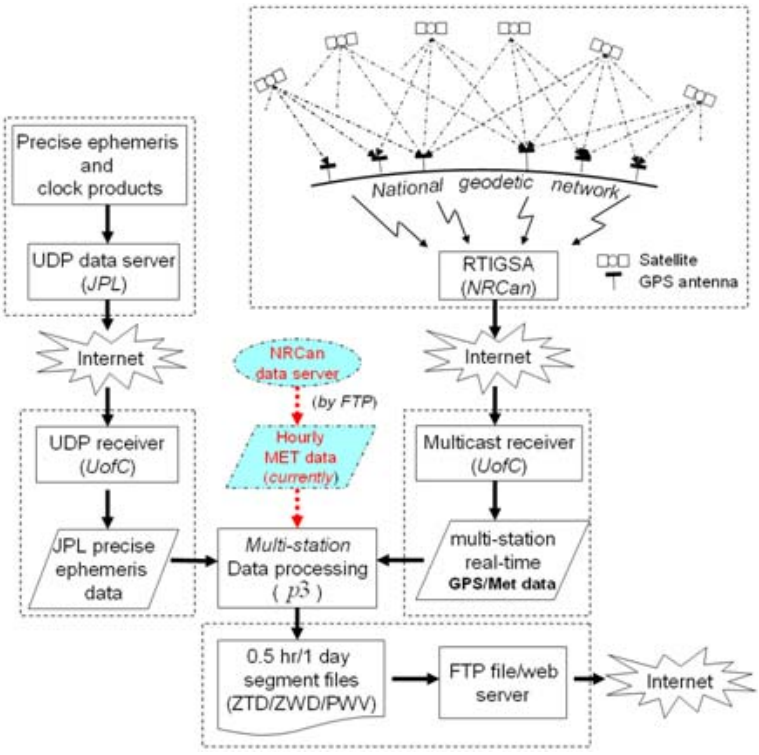

Figure 4.2 System design and dataflow diagram

(1) *GPS tracking network component*, which is a nation-wide network of GPS reference stations. It includes tracking and collecting GPS observation data, navigation data and meteorological data (temperature, pressure and relative humidity) from each station and distributing them via Multicast (IP Multicast).

(2) *Precise ephemeris correction data component*, which is responsible for collecting satellite orbit and clock correction data from JPL control center and distributing them to internet users via UDP (User Datagram Protocol).

(3) *PPP processing server component*, which performs concurrent multi-station water vapor calculation in real-time mode and outputs solutions: station coordinates, clock error and ZTD/ZWD/PWV.

(4) *Data communication component*, which includes (1) implementing IP Multicast protocol to set up data link between *GPS tracking network component* and *PPP processing server component* and decode the incoming GPS/MET data stream, and (2) implementing the UDP protocol to set up data links between *Precise ephemeris correction data component* and *PPP processing server component* and decode the incoming data stream.

(5) *Database component*, which includes a Web/FTP server and stores tropospheric products for Web clients.

The system data processing is accomplished in a pipeline of three steps:

- Raw GPS/MET signal tracking and archiving,
- Data distributing/acquiring via Internet protocol in *near* real-time mode,
- Calculating PWV observables/products using GPS PPP technique,

Afterward, near real-time PWV surface maps are estimated using Kriging interpolation based on the derived sample data from the system.

4.3 System implementation

The realization of the real-time water vapor sensing/measurement system relies on the Internet. UDP and IP Multicast are the two Internet communication protocols used in this thesis. To help understanding, these concepts are briefly illustrated in Appendix B.

4.3.1 System infrastructure

According to the system design, *GPS tracking network component* and *Precise ephemeris correction data component* are already accomplished by NRCan and JPL, respectively. To complete the whole system infrastructure, three computers are deployed at the University of Calgary (Figure 4.3).

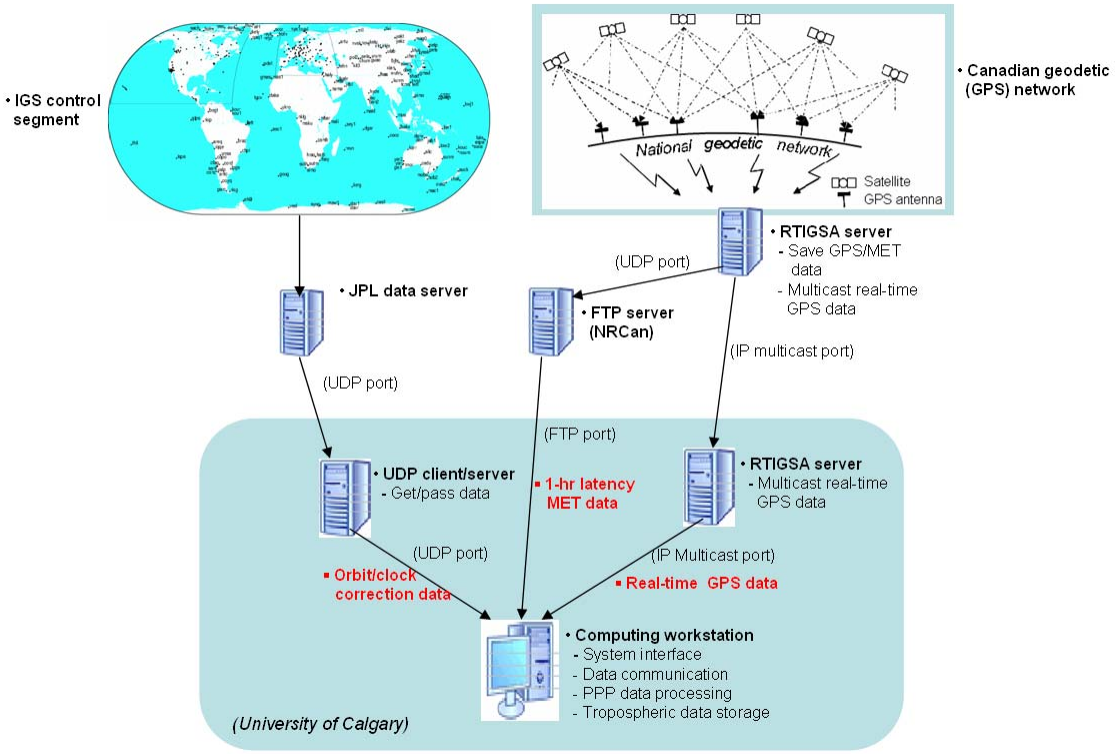

Figure 4.3 System infrastructure diagram

- *UDP client/server*, which logs in the JPL UDP data server, listens to the JPL orbit/clock correction data through UDP socket and then relays the data to computing workstation through UDP port.
- *RTIGSA server*, which is loaded with NRCan RTIGSA software (LINUX system environment) and performs the following tasks:
    - Listening to the RTIGS format data steam from the GPS stations,
    - Validating the RTIGS messages,

- Multicasting the GPS data on the subnet so that it is available to many users.

- *PPP processing workstation*, which is the central service application. It is equipped with Intel Core 2 CPU 6700 @ 2.66 GHz, 3.25 GB of RAM and 950 GB hard disk. Its allocated functions include:

  1. Data communication component, which includes two modules:
     a. UDP data receiver, which listens to/decodes JPL precise satellite orbit/clock correction data stream through UDP port.
     b. Multicast data receiver, which listens to/decode the RTIGS format GPS data through the IP multicast port.
  2. PPP-based processing server, which provides the system interface (Figure 4.4), performs multi-station real-time water vapor calculation and output solution log files.
  3. FTP/Web server, which stores the daily, hourly solution log files for each station and PWV distribution files.

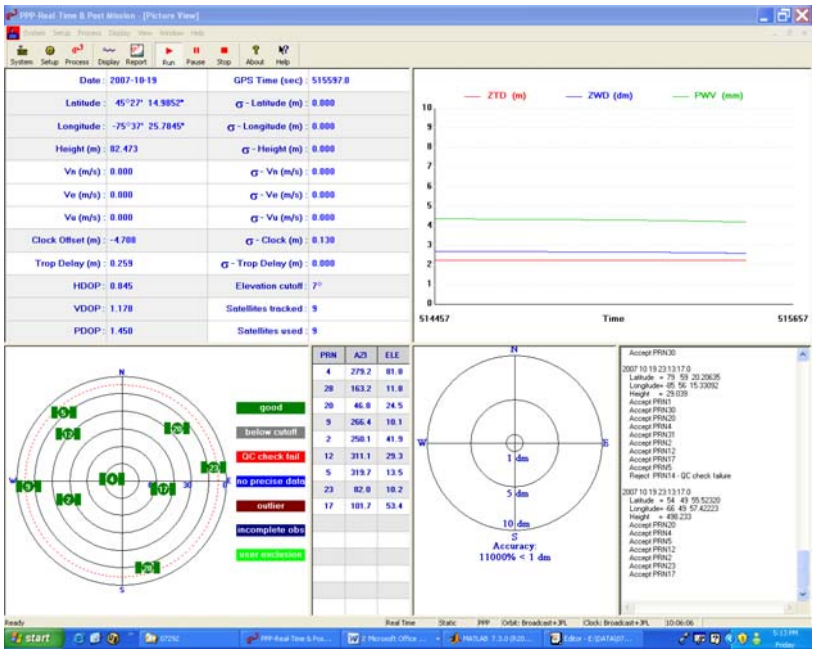

Figure 4.4 The real-time GPS PPP-inferred water vapor system interface
(The right top pane shows the (near) real-time tropospheric observables/products: ZTD, ZWD and PWV in time series in different scales)

4.3.2 Software implementation

- ***Multicast receiver***

Data communication component has two subcomponents: *UDP receiver* (for real-time JPL orbit/clock precise data) and *Multicast receiver* (for real-time GPS data). The former has already been done. This thesis handles the latter. The Multicast receiver subcomponent is developed based on RTIGSMR (Real-Time IGS Multicast Receiver) framework. Since RTIGSMR use Unix Socket for network programming interface, that part of files needs to be replaced with Windows Sockets (abbreviated "Winsock" or "WinSock") files. A new Multicast wrapper class: `CMulticastSocket` is created, which derives from MFC `CAsyncSocket` and provides all multicast protocol programming functions such as: *JoinGroup, LeaveGrou,* and *OnReceive*.

- ***PPP-based processing server***

The development of PPP-based processing server is based on the P^3 software. P^3 is originally designed for one-station processing. At present, twenty-one-station real-time data is to be processed concurrently. In PPP-based processing server, twenty one objects of Epoch are created, each of which presents a station and process its own data individually. Currently only one main thread runs inside the server to execute twenty one objects and the system performance is satisfied.

- ***MET data module***

The real-time water vapor sensing system is designed to receive and process whole real-time data set, i.e. GPS data, MET data and precise orbit/clock correction data. At present, NRCan distributes hourly MET data by FTP server with one-hour latency instead by real-time data stream. To handle this one-hour-latency MET data, an auxiliary *MET data module* is created, which consists of four Window NT command script files: MONTH_SCHEDULE.cmd, DAY_SCHEDULE_1.cmd, DAY_SCHEDULE_2.cmd and RUNFILE.cmd (Figure 4.5). MONTH_SCHEDULE.cmd file takes charge of scheduling for each individual month. Since there is a six-hour difference between local time and CTU time of the MET file, two files are created to schedule whole day transaction (hourly file downloading): DAY_SHEDULE_1.cmd for hour 00:00 ~ 15:00 and DAY_SHEDULE_2.cmd for hour16:00 ~ 23:00. RUNFILE.cmd takes charge of FTP getting file, unzipping file and saving file to local directories.

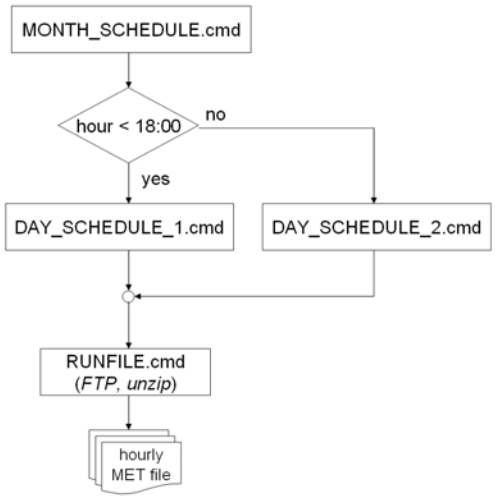

Figure 4.5 Flowchart of MET data module

- ***Integration of components***

To make the whole system work, the UDP receiver, Multicast receiver, MET data components need to be integrated with PPP-based processing server.

4.4 Summary

In this chapter, the real-time GPS PPP-inferred water vapor system design and implementation has been introduced. The aim of the system design is to construct a distributed system where distributed GPS data sources (network) and distributed computing facility (GPS software/process) cooperate under network protocols to generate the water vapor observables/products over Canada. The whole system consists of five functional segments/components: two data components, one data communication component, one GPS PPP process component and one database component. Since at present there is no real-time MET data stream, an auxiliary component is added to handle with downloading one-hour-latency MET files.

In the future when the GPS network is enlarged, *i.e.* more stations are added into the network, the increased workload of data processing can be distributed throughout the network to the newly added GPS processing center(s).

Chapter Five: System Performance Analysis

This chapter presents the evaluation of the system performance based on a two-day real-time executing segment results from the system. The performance analysis includes *position error*, *ZTD accuracy* and *PWV accuracy*. In the evaluation process, the IGS tropospheric products are used as comparison reference values (*i.e.*, true values) and post-mission results are also presented. In the end of the chapter, the accuracy comparison between the real-time GPS PPP-inferred water vapor system and some developed operational networks are shown.

5.1 Data description

The running real-time input raw dataset is from October 18~19, 2007. The observations were started to be collected 20 hours later from the execution time of the system. The data description is as follows:

- The number of GPS stations processed in the system is 19 (except MSSC and USNO where no MET data available at present);
- Each station has its own Navigation data files;
- GPS observation data sampling rate at each station is 1 Hz;
- JPL satellite orbit and clock correction data sampling intervals are 31 seconds and 1 second, respectively;
- 18 out of 19 stations have their own one-hour-latency MET data files, except for SASK;
- MET data sampling interval is 5 minutes;
- The used elevation cutoff angle is 7 degrees; and
- Each station is assigned an *executing object* (i.e. *Epoch object*) to process its own real-time data; the executions of *all* objects are *concurrent* and independent of each other.

Besides the real-time data set, the following IGS datasets were also downloaded:

- 14-day-latency International GNSS Service (IGS) tropospheric product ZTD files as *ground truth* for comparison calculation, and
- 14-day-latency IGS final orbit and clock products for post-mission calculation.

5.2 Performance evaluation

Three aspects of the system performance are analyzed in this section: *position error*, *ZTD accuracy* and *PWV accuracy*.

Since *IGS* tropospheric products are used as comparison reference values and *10* out of *19* stations within the NRCan operated GPS reference network are also part of IGS global network, the performance evaluation is conducted on these 10 stations.

5.2.1 Position error

The real-time system computes GPS receiver position, clock error, ambiguity and zenith wet delay estimates simultaneously. The position error will illustrate the accuracy level of the system solution and it can be used to assess the accuracy of the water vapor results. The positioning error may also reflect the variation of the measurement environment contributing to the water vapor bias (Skone et al., 2006). The correlation between position errors and the water vapor will be discussed in Chapter 7.

The daily coordinates in the ITRF 2000 reference frame from the Scripps Orbit and Permanent Array Center (SOPAC)[1] will be used as the reference values for the positioning error analysis. Since SOPAC does not provide daily coordinates for the IGS station *BAIE*, the following positioning error analysis has been conducted only at the other *nine* stations. Using the SOPAC coordinates as references, the position errors of those nine stations are calculated.

[1] SOPAC is an International GPS Service (IGS) Global Data Center and Global Analysis Center, which calculates and provides precise near real-time and predicted GPS satellite orbits, determines precise polar motion and Earth rotation variations and generates time series of daily three-dimensional positions for the global and California stations respect to the International Terrestrial Reference Frame (ITRF).

Shown in Figure 5.1 are the *nine*-station positioning errors in the North, East and Up directions. The corresponding statistics of errors of nine stations are given in Table 5.1 and shown in Figure 5.2.

5.2.1.1 Discussion on position errors

(1) Figure 5.1 shows that (i) the *horizontal* position errors (i.e. both *East* and *North* errors) are less than the *vertical* position error; (ii) the *East* position error is the smallest and more stable over time; (iii) the biggest position error occurs in *Up* direction with greater variations; (iv) the *Up* position error (RMS) varied greatly with different stations (Figure 5.1), which could be related with the weather variation state over each individual station (see Section 7.3.2) and the measurement environmental conditions (e.g. multipath error) around each individual station; (v) the biggest position error STD was found at station 5 (i.e. CHUR) in *UP* direction, because the convergence level jumped from -0.03 mm to 0.00 mm in the second day of the dataset duration. Based on many long-time experiments on the near real-time GPS PPP-referred water vapor system, it is found that some stations need two days for the PPP-based solution process to reach the *final* convergence limit. Since the dataset used in this analysis was collected 20 hours later after the starting of the system, the phenomena happened at station 5 is possible.

(2) Table 5.2 summarizes the overall positioning errors for all nine stations which indicate a positioning accuracy of 1.8 cm in the North, 1.1 cm in the East and 4.3 cm in the Up direction, respectively.

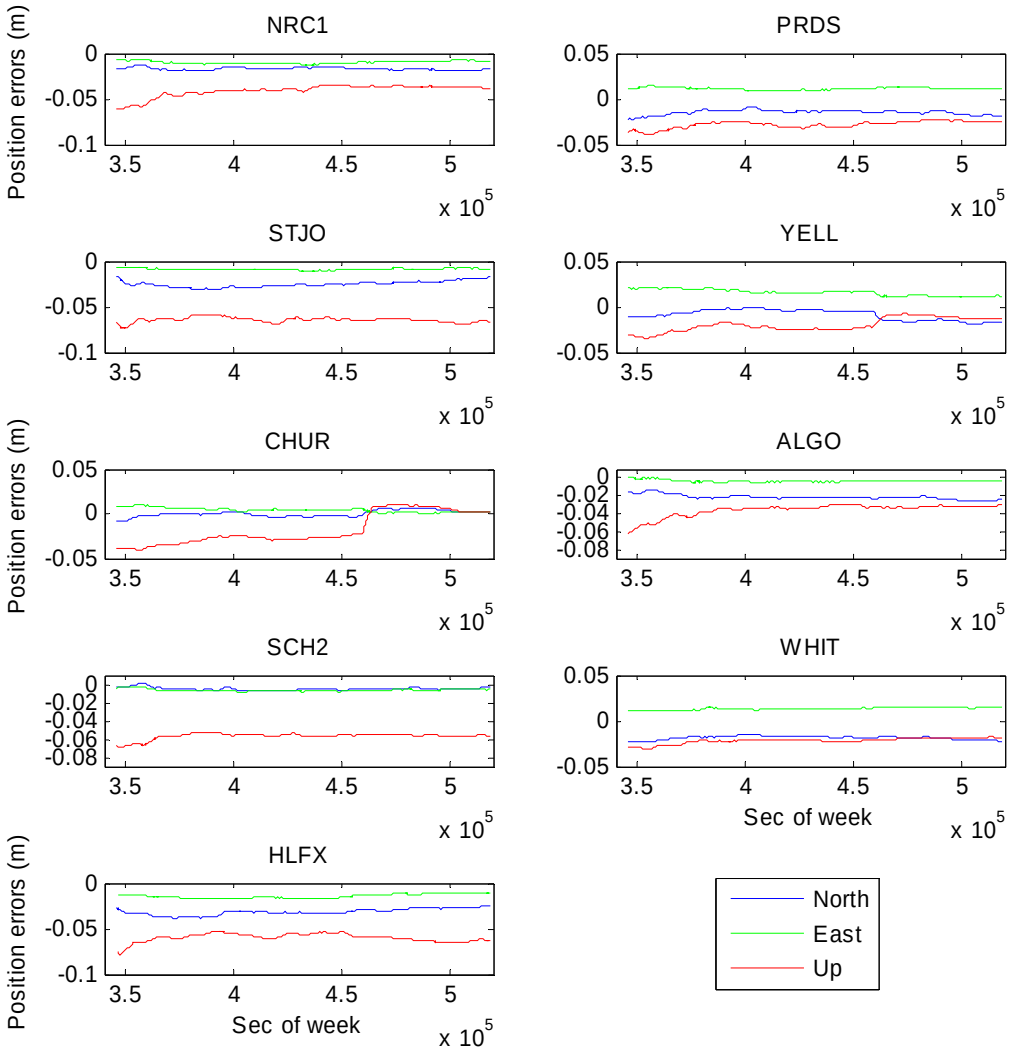

Figure 5.1 Near real-time position errors of nine stations
(The time axis represents the GPS time)

Table 5.1 Statistics of position errors of near real-time system (unit: m)

		Station								
		NRC1	**PRDS**	**STJO**	**YELL**	**CHUR**	**ALGO**	**SCH2**	**WHIT**	**HLFX**
North	*Mean*	-0.017	-0.015	-0.025	-0.009	0.000	-0.021	-0.005	-0.019	-0.032
	Std	0.002	0.003	0.003	0.006	0.004	0.003	0.002	0.002	0.002
	RMS	0.017	0.015	0.025	0.010	0.004	0.022	0.005	0.019	0.032
East	*Mean*	-0.010	0.011	0.009	0.016	0.004	-0.003	-0.006	0.013	-0.014
	Std	0.002	0.001	0.001	0.003	0.002	0.001	0.001	0.001	0.002
	RMS	0.010	0.011	0.009	0.016	0.005	0.003	0.007	0.013	0.015
Up	*Mean*	-0.041	0.028	-0.064	-0.020	-0.018	-0.036	-0.057	-0.022	-0.060
	Std	0.007	0.004	0.003	0.007	0.018	0.007	0.003	0.003	0.005
	RMS	0.042	0.028	0.064	0.021	0.025	0.036	0.057	0.022	0.060

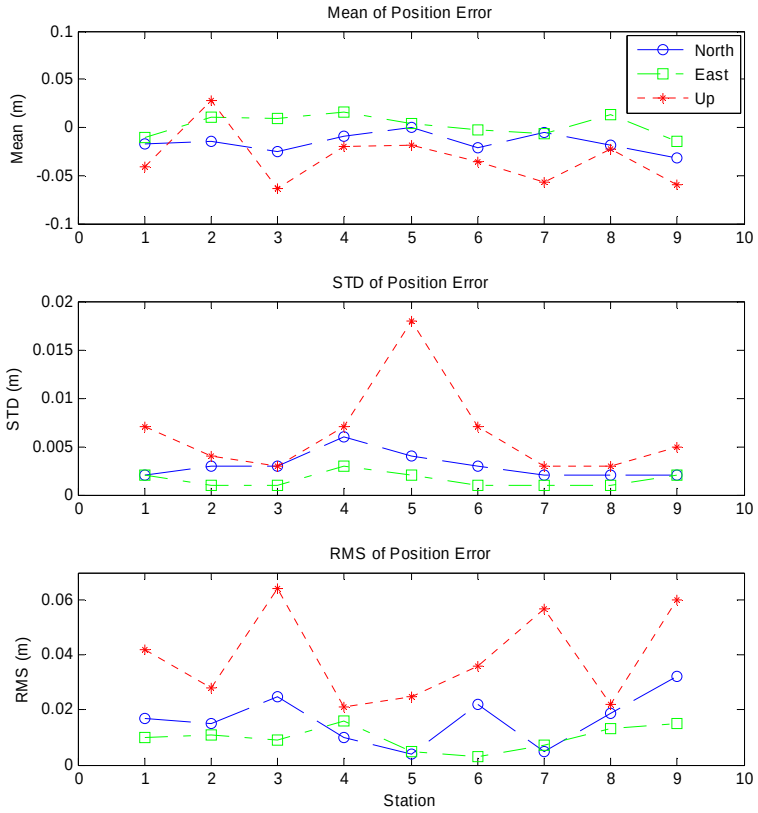

Figure 5.2 STD of station position errors

Table 5.2 Position errors of the real-time system (unit: m)

	RMS of North	**RMS of East**	**RMS of Up**
Mean	0.016	0.010	0.039
Std	0.009	0.004	0.017
RMS	**0.018**	**0.011**	**0.043**

5.2.2 ZTD accuracy

The following two methods can be utilized to assess the real-time system performance on the zenith total delay estimation:

(i) A comparison of the system against independent observations from radiosondes and radiometers;

(ii) A comparison of the system to the IGS tropospheric products.

Since there is no water vapor observation from a radiosonde or radiometer at the ten test stations, the second method has been employed. In this investigation, two types of ZTD solutions are estimated from the near real-time system: the *near real-time* ZTD solution and the *post-mission* ZTD solution. Both will be compared to the IGS's ZTD products.

Because the meteorological data used for tropospheric product calculation has a latency of one hour, the ZTD solutions from the near real-time system are actually the estimates of the water vapor one hour *earlier*. A *one-hour time shift* is therefore applied to the ZTD solutions before they are compared to the IGS ZTD products. Each station's ZTD curves obtained from the near real-time (N.R.T.) processing, the post-mission (P.M.) processing and IGS are shown in Figure 5.3. The ZTD comparison statistics are presented in Table 5.3 and Figure 5.4. A further statistic analysis was conducted on the data shown in Table 5.3. A summary of the system performance is given in Table 5.4.

5.2.2.1 Discussion on ZTD accuracy

(1) Figure 5.3 shows that (i) both N.R.T. ZTD and P.M. ZTD curves have a good agreement with the IGS ZTD in tendency; (ii) both N.R.T. ZTD and P.M. ZTD curves lag behind IGS ZTD for some distance; (iii) the values of '*N.R.T. ZTD – IGS ZTD*' and '*P.M.. ZTD – IGS ZTD'* are affected by the weather variation state: the sharper the variation, the bigger the values of '*N.R.T. ZTD – IGS ZTD'* and '*P.M. ZTD – IGS ZTD*' due to the lag distances between them, which is displayed clearly on the results of ALGO station.

(2) The results given in Table 5.4 indicate that (i) the N.R.T. ZTD has a difference of ~13 mm (RMS) from the IGS ZTD, which is within the accuracy level of current tropospheric products (see Section 5.3); (ii) the N.R.T. ZTD can achieve the accuracy of P.M. ZTD; (iii) the overall accuracy of P.M. ZTD was not better than the accuracy of N.R.T. ZTD, which is questionable and needed to be further validated when real-time meteorological data stream is provided in the future.

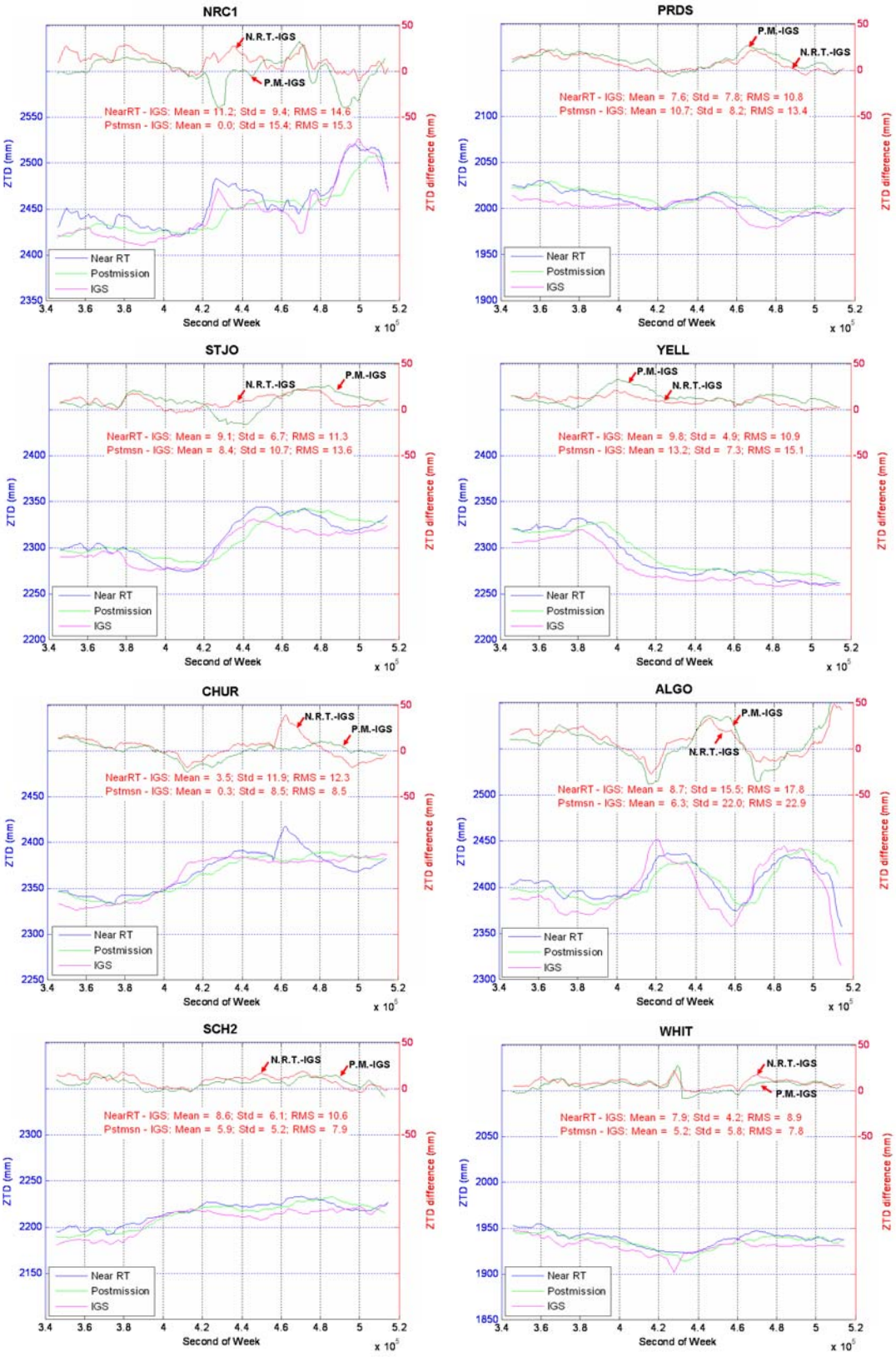

Figure 5.3 Ten station ZTD comparison plots between near real-time, post-mission and IGS (1)
(Unit: mm)

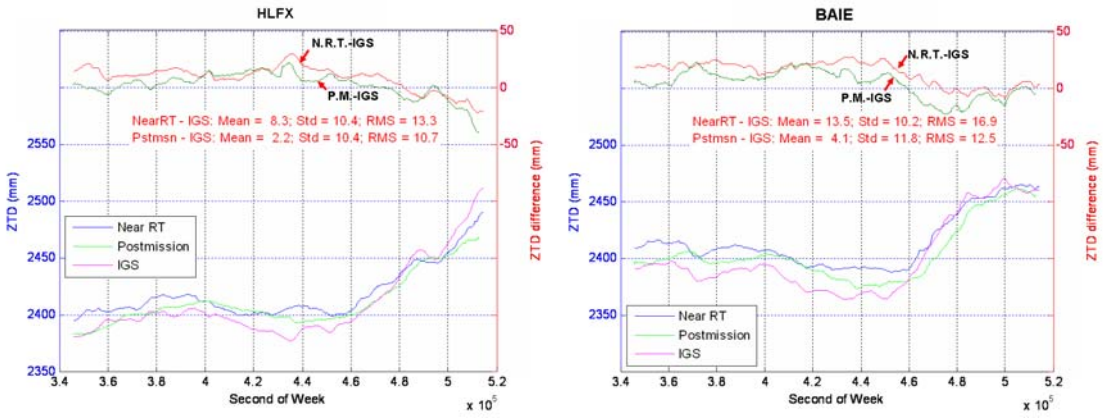

Figure 5.3 Ten station ZTD comparison plots between near real-time, post-mission and IGS (2) (Unit: mm)

Table 5.3Statistics of ZTD comparisons: N.R.T.-IGS and P.M.-IGS (unit: mm)

		Mean	Std	RMS
NRC1	*N.R.T.*	11.2	9.4	14.6
	P.M.	0.0	15.4	15.3
PRDS	*N.R.T.*	7.6	7.8	10.8
	P.M.	10.7	8.2	13.4
STJO	*N.R.T.*	9.1	6.7	11.3
	P.M.	8.4	10.7	13.6
YELL	*N.R.T.*	9.8	4.9	10.9
	P.M.	13.2	7.3	15.1
CHUR	*N.R.T.*	3.5	11.9	12.3
	P.M.	0.3	8.5	8.5
ALGO	*N.R.T.*	8.7	15.5	17.8
	P.M.	6.3	22.0	22.9
SCH2	*N.R.T.*	8.6	6.1	10.6
	P.M.	5.9	5.2	7.9
WHIT	*N.R.T.*	7.9	4.2	8.9
	P.M.	5.2	5.8	7.8
HLFX	*N.R.T.*	8.3	10.4	13.3
	P.M.	2.2	10.4	10.7
MAIE	*N.R.T.*	13.5	10.2	16.9
	P.M.	4.1	11.8	12.5

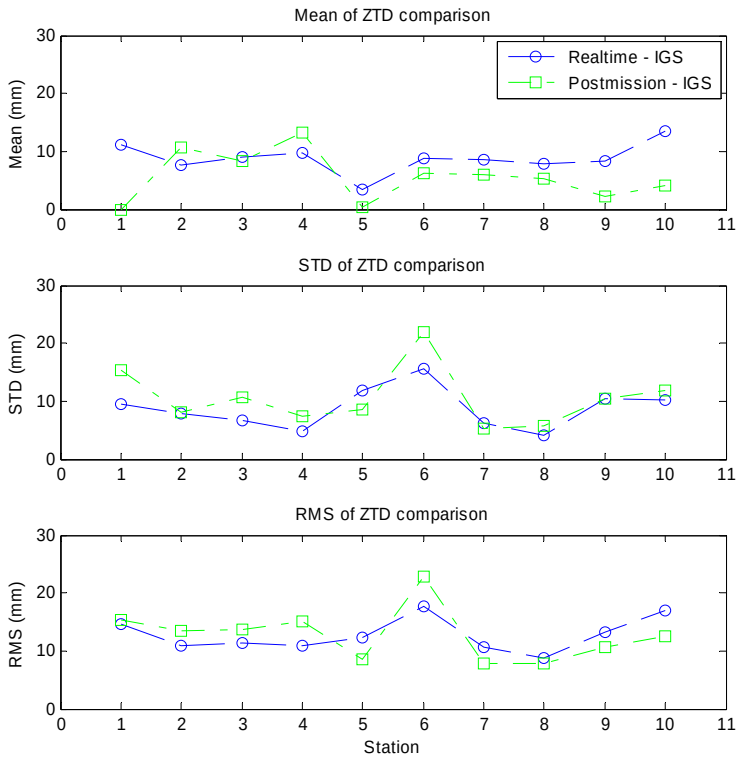

Figure 5.4 Ten station ZTD Mean/STD/RMS plots

Table 5.4 ZTD statistics of N.R.T. system (unit: mm)

	Mean of ZTD Comparison		**STD of ZTD Comparison**		**RMS of ZTD Comparison**	
	N.R.T.	*P.M.*	*N.R.T.*	*P.M.*	*N.R.T.*	*P.M.*
Mean	8.82	5.63	8.71	10.53	12.74	12.77
Std	2.57	4.29	3.47	5.03	2.89	4.55
RMS	**9.15**	6.95	**9.31**	11.56	**13.03**	13.48

5.2.3 PWV accuracy

Since IGS does not provide the PWV product, the IGS PWV values are obtained by subtracting the ZHD (Zenith Hydrostatic Delay) from the IGS ZTD and then dividing the resulting ZWD by a conversion coefficient (both ZHD (Equation 2.19) and the conversion coefficient (= 6.5 (Equation 2.38)) are given in the GPS PPP-inferred water vapor model). Each station's PWV curves from the near real-time (N.R.T.), the post-mission (P.M.) and IGS are shown in Figure 5.5. The PWV comparison statistics are

presented in Table 5.5 and Figure 5.6. A further PWV analysis is conducted on the statistical data presented in Table 5.5 and a summary of the system PWV performance is provided in Table 5.6. The PWV results look consistent to the results obtained for the ZTD estimates. The results show that the near real-time system PWV differs from the IGS PWV in ~2 mm, which is within the accuracy level of current tropospheric products (see Section 5.3). But, the overall accuracy of P.M. PWV was not better than the accuracy of N.R.T. PWV, which is questionable and needed to be further validated when real-time meteorological data stream is provided in the future.

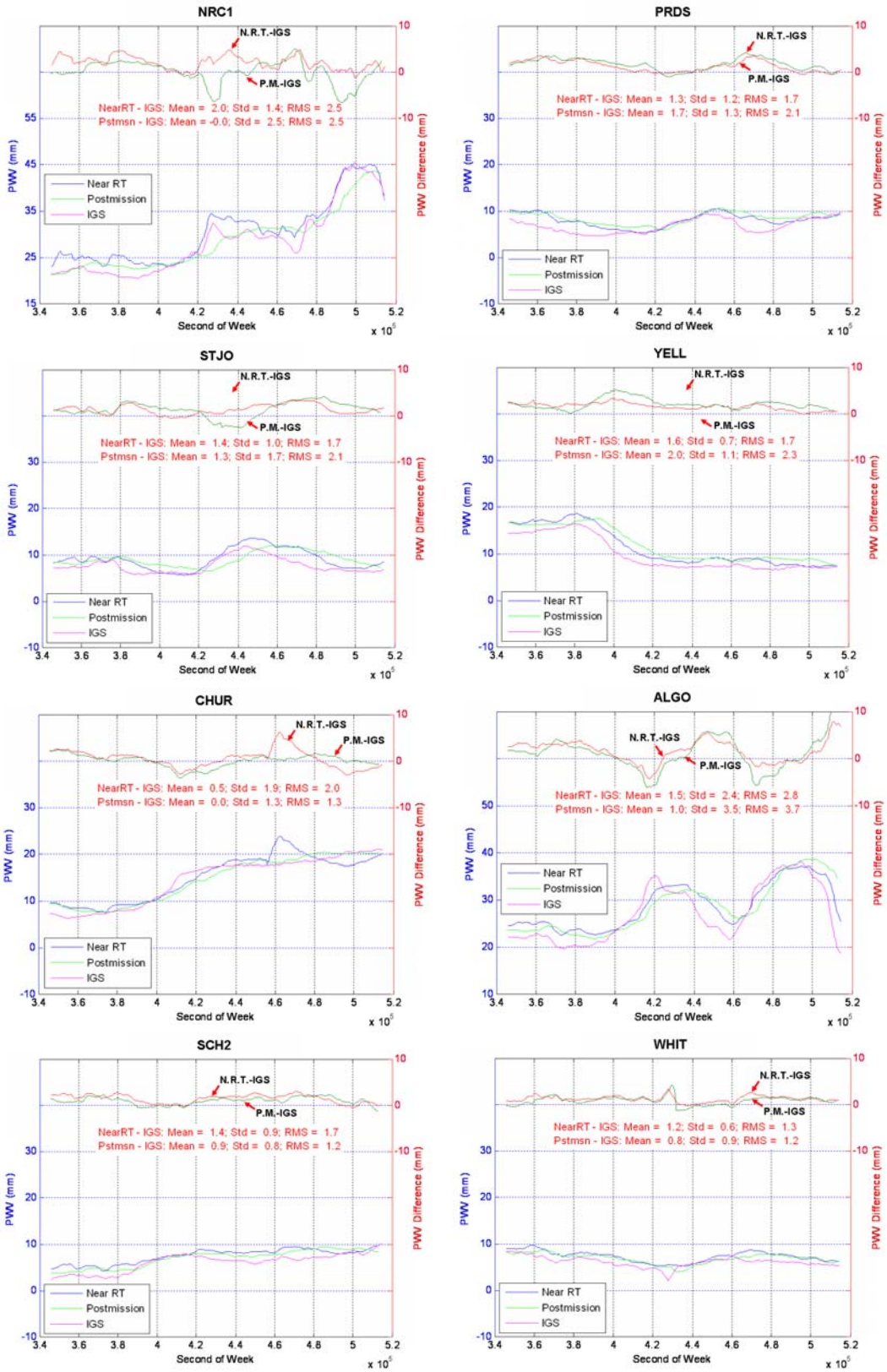

Figure 5.5 Ten station PWV comparison plots between near real-time, post-mission and IGS (1)
(Unit: mm)

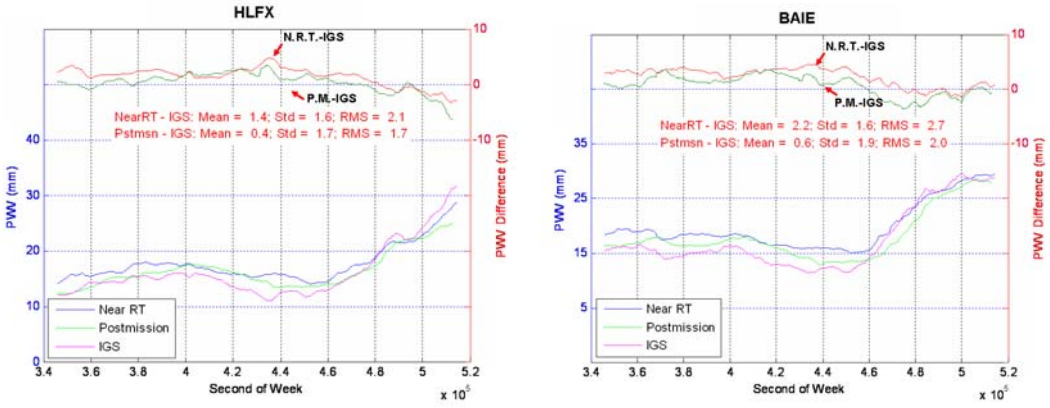

Figure 5.5 Ten station PWV comparison plots between near real-time, post-mission and IGS (2) (Unit: mm)

Table 5.5 Statistics of PWV comparisons: N.R.T.-IGS and P.M.-IGS (unit: mm)

		Mean	Std	RMS
NRC1	*N.R.T.*	2.0	1.4	2.5
	P.M.	0.0	2.5	2.5
PRDS	*N.R.T.*	1.3	1.2	1.7
	P.M.	1.7	1.3	2.1
STJO	*N.R.T.*	1.4	1.0	1.7
	P.M.	1.3	1.7	2.1
YELL	*N.R.T.*	1.6	0.7	1.7
	P.M.	2.0	1.1	2.3
CHUR	*N.R.T.*	0.5	1.9	2.0
	P.M.	0.0	1.3	1.3
ALGO	*N.R.T.*	1.5	2.4	2.8
	P.M.	1.0	3.5	3.7
SCH2	*N.R.T.*	1.4	0.9	1.7
	P.M.	0.9	0.8	1.2
WHIT	*N.R.T.*	1.2	0.6	1.3
	P.M.	0.8	0.9	1.2
HLFX	*N.R.T.*	1.4	1.6	2.1
	P.M.	0.4	1.7	1.7
BAIE	*N.R.T.*	2.2	1.6	2.7
	P.M.	0.6	1.9	2.0

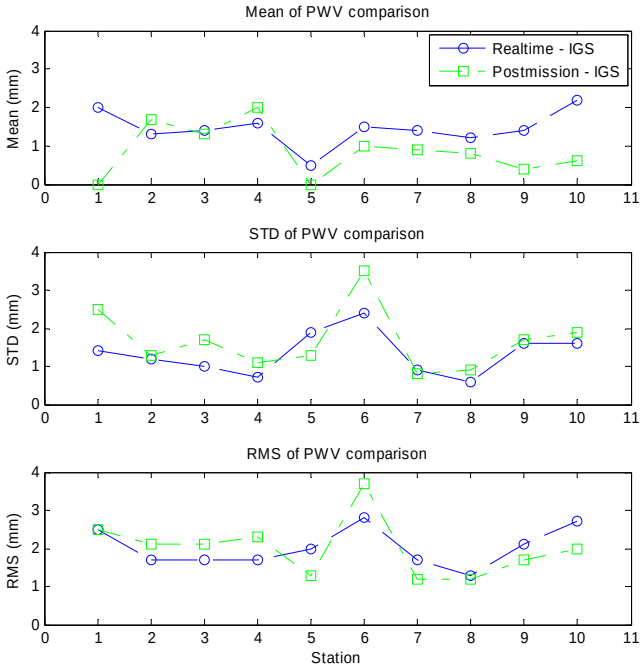

Figure 5.6 Ten station PWV Mean/STD/RMS plots

Table 5.6 PWV statistics of near real-time system (unit: mm)

	Mean of PWV Comparison		**STD of PWV Comparison**		**RMS of PWV Comparison**	
	N.R.T.	*P.M.*	*N.R.T.*	*P.M.*	*N.R.T.*	*P.M.*
Mean	1.45	0.87	1.33	1.67	2.02	2.01
Std	0.46	0.66	0.56	0.82	0.50	0.75
RMS	**1.51**	1.07	**1.43**	1.84	**2.07**	2.13

5.3 Accuracy comparison with external results

The accuracy of the GPS-derived ZTD products largely depends on the processing method used. The current accuracy level of the GPS ZTD estimation is in the order of 10~15 mm. This is translated into an accuracy level of GPS-derived PWV estimation in the order of 1~2 mm (Deblond et al., 2005; Haan, 2006). In order to have a general assessment of the accuracy of the PPP-derived ZTD products, shown in Table 5.7 is an accuracy comparison of the real-time system with some operational GPS network ZTD

products (Haan, 2006). Since this study has no numerical weather prediction model (NWPM) values, the ZTD accuracy results of the real-time GPS PPP-inferred water vapor are from the comparison with IGS. The results show that the real-time GPS PPP-inferred water vapor system can reach a comparable accuracy level with other operational GPS networks for water vapor estimation.

Table 5.7 ZTD statistics between GPS operational models**

Processing Center	Number of Comparison	Bias (mm)	RMS (mm)	STD (mm)	Comparison Model
ASI (Italy)	7994	-5.58	11.74	10.32	NWPM*
BKG (Germany)	9632	-6.66	12.04	10.03	NWPM
GFZ (Germany)	9205	-4.76	9.94	8.73	NWPM
KNMI (Netherlands)	1377	-2.39	7.14	6.73	NWPM
LPT (Switzerland)	10286	-5.87	11.39	9.76	NWPM
METO (U.K.)	8766	-3.75	10.81	10.14	NWPM
SGN (France)	8354	7.57	13.60	11.29	NWPM
(Near) Real-time GPS PPP-inferred water vapor system	3162	9.15	13.03	9.31	IGS

* Numerical Weather Prediction Model

** The statistics of the first seven processing centers was over the period: 2005/10/05 – 2006/02/21; the statistics of (near) real-time GPS PPP-inferred water system was over the period 2007/10/18 – 2007/10/19

5.4 Summary

The performance evaluation shows that (i) the position errors of the (near) real-time GPS PPP-inferred water vapor system is within sub-decimeter (RMS = 0.0l1 ~ 0.043 m); (ii) the significant position error happens in the Up direction which has relation to the un-modeled atmospheric errors; (iii) the ZTD and PWV accuracies of the current (near) real-time water vapor system are ~13 mm and ~2 mm, respectively, which should be further validated when the real-time meteorological data stream is available to the system.

Chapter Six: PWV Prediction and Interpolation

Prediction of local and regional PWV and quantitative description of its distribution over Canada is an essential aspect of the real-time GPS PPP-inferred water vapor system. The geostatistical interpolation method of *kriging* is a unique tool to deal with this issue. Geostatistics is oriented to the analysis of spatially distributed variables and in particular the estimation or prediction of values at unsampled locations. Geostatistical technologies underlie most attempts to create surface maps based on point samples or observations (Nelson et al., 1999). Three basic components of geostatistics are:

- (Semi)variogram analysis – characterization of spatial correlation
- Kriging – optimal interpolation; generation of best linear unbiased estimate at each location with semivariogram model
- Stochastic simulation – generation of multiple equiprobable images of the variable with semivariogram model (Bohling, 2005)

In this chapter, firstly, the geostatistical methodology is briefly described. And then, how this method is implemented in a program to derive the desired interpolated map of PWV is explained. At last, the products and analytic results of the program executed on one-day 24-hour datasets from the real-time GPS PPP-inferred water vapor system are presented.

6.1 Geostatistical methodology

6.1.1 Introduction

The basic object the geostatistics considers is the spatial data, which is usually viewed as a real-valued *stochastic process* (i.e. a random function (*RF*)) $\left\{Z(\vec{s}) : \vec{s} \in D \subset R^d\right\}$ where D is a subset of R^d (d-dimensional Euclidean space, d = 1, 2, 3, …). For example, $Z(\vec{s})$ may represent the concentration of atmospheric water vapor (PWV) at a specific location $\vec{s}$. Some geostatistics-related concepts are introduced as follows.

- *Strictly stationary process*

Let $\mu(\vec{s}) = E\{Z(\vec{s})\}$ and $\sigma^2(\vec{s}) = \text{var}\{Z(\vec{s})\}$ denote the mean value and the variance value, respectively. The process Z is said to be (*strictly*) *stationary* if its statistical properties of *Z* are invariant to a shift of the origin (Fuentes, 2002): $\mu(\vec{s}) = \mu(\vec{s} + \vec{h}) = \mu$ and $\sigma^2(\vec{s}) = \sigma^2(\vec{s} + \vec{h}) = \sigma^2$ for all $\vec{s}$ and any $\vec{h}$.

- *Second-order stationary process*

Let $cov\{Z(\vec{s}_i), Z(\vec{s}_j)\} = cov\{\vec{s}_i - \vec{s}_j\}$ (for all $\vec{s}_i \in D$, $\vec{s}_j \in D$) denote the covariance of this process at any two particular points $\vec{s}_i$ and $\vec{s}_j$. The process Z is called *second-order stationary* or *weakly stationary* if $\mu(\vec{s}) \equiv \mu$ (constant), *i.e.*, the mean is the same for all $\vec{s}$, and $cov\{Z(\vec{s}_i), Z(\vec{s}_j)\} = cov\{Z(\vec{s}) - Z(\vec{s} + \vec{h})\} = cov(\vec{h})$, for all $\vec{s}_i \in D$, $\vec{s}_j \in D$. This means that $\text{cov}\{Z(\vec{s}_i), Z(\vec{s}_j)\}$ depends on the vector difference, $\vec{h}$, between $\vec{s}_i$ and $\vec{s}_j$. $\text{cov}(\bullet)$ is referred as to the *covariogram* of the process, for short, $\text{cov}(\bullet)$ is written as $C(\bullet)$.

- *Variogram and semivariogram*

Suppose $\mu(\vec{s})$ is a constant and then define

$$var\{Z(\vec{s} + \vec{h}) - Z(\vec{s})\} = 2\gamma(\vec{h}), \tag{6.1}$$

for all $\vec{s}$, $\vec{s} + \vec{h} \in D$. The statement (6.1) means that the differences of variables lagged $\vec{h}$-apart vary in a way that depends only on $\vec{h}$. The quantity $2\gamma(\vec{h})$, which is a function only of $\vec{h}$, is called the *variogram* and $\gamma(\vec{h})$ the *semivariogram*. The semivariogram is a plot of the structure function which decribes the relationship between measurements taken some distance (*h*) apart (Figure 6.1). Semivariograms defines the range or distance over which spatial dependence exists.

Semivariogram is central to geotatistics - it is the key to understanding, describing and predicting spatial variation quantitatively (McBratney et al., 1986).

- *Isotropic process*

The process Z is *isotropic* if its $2\gamma(\vec{h}) = 2\gamma^0(\|\vec{h}\|)$, for $\vec{h} \in R^d$, i.e. (semi)variogram depends on *only* the distance $\|\vec{h}\|$ between locations; otherwise it is *anisotropic*. Anisotropies are caused by the underlying physical process evolving differentially in space (Cressie, 1994).

- *Intrinsic stationary process*

If the process Z satisfies the properties: $E\{Z(\vec{s}+\vec{h}) - Z(\vec{s})\} = 0$ and $\mathrm{var}\{Z(\vec{s}+\vec{h}) - Z(\vec{s})\} = 2\gamma(\vec{h})$, then it is called *intrinsically stationary*. That is, the process Z is defined through a constant mean and constant variance in the location difference $\vec{h}$.

A process which is both intrinsically *stationary* and *isotropic* is also called *homogeneous*.

Generally speaking, intrinsic stationary assumption is mostly required by much of the theory of spatial processes. Based on this point of view, the stronger forms of stationary are not needed (Fuentes, 2002).

- *The relation between covariogram and variogram*

For a stationary process, it can be verified that

$$\begin{aligned}
&\mathrm{var}\{Z(\vec{s}_i) - Z(\vec{s}_j)\} \\
&= \mathrm{var}\{Z(\vec{s}_i)\} + \mathrm{var}\{Z(\vec{s}_j)\} - 2\,\mathrm{cov}\{Z(\vec{s}_i), Z(\vec{s}_j)\} \\
&= 2\,\mathrm{cov}(\vec{0}) - 2\,\mathrm{cov}(\vec{h}) \qquad (6.2)
\end{aligned}$$

thus

$$\gamma(\vec{h}) = \mathrm{cov}(\vec{0}) - \mathrm{cov}(\vec{h}) = \sigma^2 - \mathrm{cov}(\vec{h}) \quad (\because \mathrm{cov}(\vec{0}) = \sigma^2). \qquad (6.3)$$

So, for a stationary spatial process the covariogram and vairogram provide similar information in a different form.

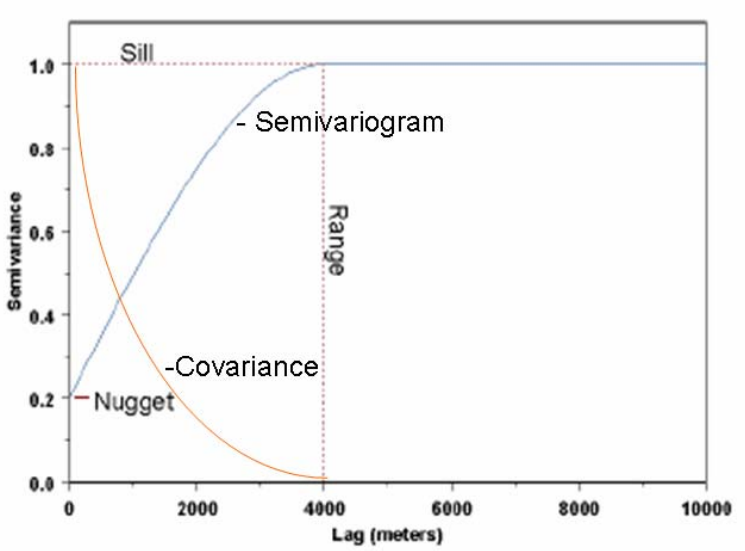

Figure 6.1 Characteristics of the semivariogram and relation between semivariogram and covariance ((1) *Sill* is the upper bound of variogram, i.e. maximum variogram; when the (semi)variogram reaches it the graph flattens. The sill estimates a quantity known as the *a prior* variance of the random variable. (2) *Range* is the lag value at which the variograms reaches its sill. Range is the limit of spatial dependence; beyond it the variance bears no relation to the separated distance) (Adapted from Basu et al. (1997))

6.1.2 Geostatistical approach

Geostatistics is the standard approach in disciplines such geology and hydrology, in which the aim is to generate the best estimates in the sense of unbiasedness and minimum mean squared error and where it is desirable to have a realistic evaluation of the estimation variance. As seen above, the geostatistical approach is stochastic and considers the phenomenon under study as a random function (RF), a random field or a stochastic process and the experimental data are realizations of the RF. The geostatistical approach consists of three stages (Pardo-Iguzquiza et al., 2005):

1) ***Model selection***. The most practical model should explain the data satisfactorily and have a simple model form as well. For instance, it must be decided whether the stochastic process has the constant mean or a specially variable mean for a realistic purpose; a decision must be made on the spatial covariance is the isotropic or anisotropic.
2) ***Parameter inference***. The values of parameters which defines the model are unknown and need to be estimated using the sample data. For instance, the semi-variogram is defined by the parameters such as: the *range* of correlation, *sill* and *nugget* variance.

3) ***Interpolation***. This stage includes the *estimation* of the values of the variable at the un-sampled points and a quantification of the magnitude of the error (i.e. its variance) incurred in the estimation. This process is performed by *kriging*.

The three stages are related: what kind of kriging to be used depends upon the resulting model at stage 1 and the application of kriging requires the model parameters to be estimated at stage 2. Once stages 1 and 2 are completed, kriging (stage 3) is just a process of a well-known computing algorithm.

6.1.2.1 Stage one: Model selection

1. The process model

The process of model selection consists of deciding which, among a family of possible models, best explains the data on the basis of given criteria. The family of models must be sufficiently flexible to cover most of the situation encountered in practical applications. In particular:

1) The family of models must include both constant mean and spatially varying mean.
2) The statistical function that describes spatial variability must have sufficient parameters to model different degree of continuity of the RF.

In practice, the most useful model, and one that has physical interpretation, is an RF: $Z(\vec{s})$ that has two components, namely (Bailey et al., 1995):

$$Z(\vec{s}) = \mu(\vec{s}) + U(\vec{s}) \tag{6.4}$$

where $\mu(\vec{s})$ is a trend surface representing mean, a large scale or first order component, *i.e.* $E(Z(\vec{s})) = \mu(\vec{s})$, where $E(\bullet)$ is the mathematical expectation operator; $U(\vec{s})$ represents a local or second order component, which is a zero-mean stationary RF with covariance function $C(\vec{h})$, i.e., $E(U(\vec{s})) = 0$ and $E[U(\vec{s}) \cdot U(\vec{s} + \vec{h})] = C(\vec{h})$.

When the process to be predicted, $Z(\vec{s})$, has a constant mean value, *i.e.* $\mu(\vec{s}) = \mu$, RF: $Z(\vec{s})$ has a simplest form:

$$Z(\vec{s}) = \mu + U(\vec{s}) \tag{6.5}$$

and RF $Z(\vec{s})$ is itself then *second-order stationary*. This case is sometimes referred to as a model without *drift*.

If the mean of the process is not constant then it is assumed to vary in space and may be represented in a low-order polynomial form. For instance, linear for a drift of order 1:

$$\mu(\vec{s}) = \beta_0 + \beta_1 x_1(\vec{s}) + \beta_2 x_2(\vec{s}) \tag{6.6}$$

This model captures the local trend of the attribute besides the global trend. Equation (6.4) can be rewritten in matrix notation:

$$Z = \vec{x}^T(\vec{s}) \cdot \beta + U(\vec{s}) \tag{6.7}$$

where

$$Z^T = [z_1, ..., z_n],$$

$$\vec{x}^T = \begin{bmatrix} 1, ..., 1 \\ x_1(s_1), ..., x_1(s_n) \\ x_2(s_1), ..., x_2(s_n) \end{bmatrix},$$

$$\beta^T = [\beta_0, \beta_1, \beta_2],$$

$$U^T = [U_1, ..., U_n],$$

and *n* is the number of sample data. The realistic type of kriging for this model is *universal kriging*.

In this thesis, it is assumed that the process (PWV) to be predicted is *second-order stationary* and the realistic type of kriging is *ordinary kriging*.

2. Semivariogram model

For interpolation purpose, the covariance $C(\vec{h})$ must be estimated. Assuming second-order stationary (see section 1.1.1), the relation of covariance and semivariogram is given in Equation 6.3:

$$\gamma(\vec{h}) = \text{cov}(\vec{0}) - \text{cov}(\vec{h}) = \sigma^2 - \text{cov}(\vec{h});$$

and the covariance and the semivariogram can be regarded as equivalent statistical tools. Instead the appropriate semivariogram model must be selected for the process to be predicted.

Among the families of valid (semi)variogram models (Webster et al., 2004), three most commonly used for stationary processes are:

(1) *The spherical model:*

$$\gamma(h)=\begin{cases} c_0+c\left[\dfrac{3h}{2a}-\dfrac{1}{2}\left(\dfrac{h}{a}\right)^2\right], & 0<h\le a \\ c_0+c, & h>a \\ 0, & h=0 \end{cases} \tag{6.8}$$

where c_0 is the nugget effect, c_0+c is the sill and *a* is the range.

(2) *The exponential model*:

$$\gamma(h)=\begin{cases} c_0+c\left[1-\exp\left(-\dfrac{3h}{a}\right)\right], & h>0 \\ 0, & h=0 \end{cases} \tag{6.9}$$

(3) *The Guassian model*:

$$\gamma(h)=\begin{cases} c_0+c\left[1-\exp\left(-\dfrac{3h^2}{a^2}\right)\right], & h>0 \\ 0, & h=0 \end{cases} \tag{6.10}$$

The plots of these three theoretical semivariogram models are shown in Figure 6.2. The different models represent different degrees of continuity of the process (RF) to be predicted. The range of the semivariogram is equivalent to the correlation scale, i.e. it gives the maximum distance for which the data are correlated (see Figure 6.1). The nugget effect (see Figure 6.1) allows discontinous phenomena to be modeled; the discontinuity may be caused by monitoring errors or by the structures of variability at scales smaller than the smallest distances between sample locations (Pardo-Iguzquiza et al., 2005).

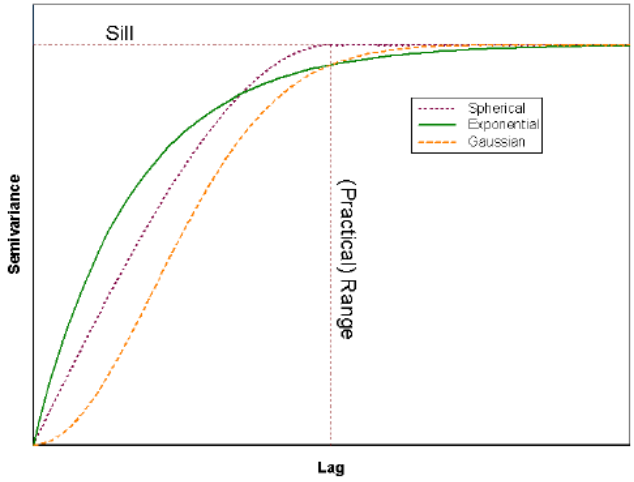

Figure 6.2 Three common semivariogram models (without nugget effect)
(Different models have different shapes with different sills and ranges)

In this thesis, spherical model, Gaussian model and exponential model are fitted with the hourly PWV experimental semivariogarm using nonlinear weighted least-squares method (see Section 6.1.2.2). The best fit model is determined with cross-validation method.

6.1.2.2 Stage two: Estimate semivariogram model

Estimating semivariogram is usually a two-step process: (i) calculate/estimate experimental semivariogram from the sample data and (ii) fit a theoretical semivariogram model to the experimental estimate.

1. Calculate/Estimate experimental semivariogram

The simplest estimator is the *method of moment* (MoM) estimator. In the case where N sampling points $\vec{s}_1$, $\vec{s}_2$, … $\vec{s}_N$ lie on a *regular* lattice, for any given separation $\vec{h}$ the formula is defined by (Bailey and Gatrell, 1995)

$$\hat{\gamma}(\vec{h}) = \frac{1}{2\left|N(\vec{h})\right|} \sum_{(\vec{s}_i,\vec{s}_j)\in N(\vec{h})} \left\{Z(\vec{s}_i) - Z(\vec{s}_j)\right\}^2, \tag{6.11}$$

where $N(\vec{h})$ denotes all pairs $(\vec{s}_i, \vec{s}_j)$ for which $\vec{s}_i - \vec{s}_j = \vec{h}$ and $|N(\vec{h})|$ denotes the number of $N(\vec{h})$; $\sum(\cdot)$ is over all pairs of observed data points with a vector separation of $\vec{h}$. In the case where *N* points *irregularly* located, $N(\vec{h})$ is defined as

$$N(h) = \{(\vec{s}_i, \vec{s}_j) : \vec{s}_i - \vec{s}_j \in T(\vec{h})\}, \tag{6.12}$$

where $T(\vec{h})$ denotes small neighbourhood or tolerance region around $\vec{h}$. $\hat{\gamma}(\vec{h})$ is experimental semivariogram. An example plot of $\hat{\gamma}(\vec{h})$ is shown in Figure 6.2.

The experimental semivariogram summarizes the spatial relations in the data. However, it is subject to error. This error arises largely from sampling fluctuation and gives experimental variogram a more or less erratic appearance (Webster et al., 2004). The experimental semivariogram is to be used to estimate the *true* variogram to describe the variance of the region (see next section). To get statistically more reliable results, a certain amount of observations is required to calculate the experimental semivariogram. Some papers suggest this number should be greater than 20~30 (IHF, 2008).

2. Fitting semivariogram models

Fitting variogram model means choosing a suitable theoretic function and fitting it to the semivariogram $\gamma(\vec{h})$ in a statistical way. This is an important procedure in geostatistics, which makes it possible to estimate or predict values at unsampled places and in larger region optimally by kriging.

There are two categories of statistic methods to achieve this task: *maximum likelihood* (ML) and *least squares* (LS). The former has two main drawbacks: (1) it relies heavily on the Gaussian distributional assumption, and (2) the estimations are biased (Jian et al., 1996). And so, the semivariogram model fitting is usually performed by LS.

Let $\hat{\gamma}(\vec{h})$ donate the vector of experimental semivariogram estimates, $\gamma(\vec{h}, \theta)$ the vector with values of semivariogram model of interest with a finite unknown parameter vector. $\theta = \lfloor \theta_1, \theta_2, ..., \theta_p \rfloor$ The best set of parameters is the one that minimizes the sum

of the squares differences, *R*, between the experimental values and those predicted by the model, $R = \left[\hat{\gamma}\left(\vec{h}\right) - \gamma\left(\vec{h};\ \theta\right)\right]^T V^{-1}\left[\hat{\gamma}\left(\vec{h}\right) - \gamma\left(\vec{h};\ \theta\right)\right]$.

There are three well-known versions of nonlinear least squares estimators:

- *Oridnary least squares* (OLS), in which *V* is a indentity matrix *I* , *i.e.*, $V = I$.
- *Generalized least squares* (GLS), in which *V* is the variance matrix of the experimental semivariogram. Usually *V* is unknown and it must be assumed.
- *Weighted least squares* (WLS), in which $V = W(\theta)$, the diagonal matrix whose diagonal entries are the variances of variance of the entries of $\hat{\gamma}\left(\vec{h}\right)$ (Fuentes, 2002). This approach is a special situation of weighted least squares (Jian et al., 1996).

Among these three estimators, the increasing order of efficiency is OLS, WLS, GLS and the decreasing order of convenience to use is OLS, WLS, GLS (Fuentes, 2002). Based on simulation studies, Zimmerman and Zimmerman (1991) have found that the weighted least squares is the most favourable approach for semivariogram-model fitting of others (Zimmerman and Zimmerman, 1991). In this thesis, WLS is the one employed.

Let $\hat{\gamma}(h(j))$ be the experimental semivariogram estimated from the sample data at discrete lags $h(1),\ h(2),\ \ldots,\ h(k)$. Let $\gamma(h(j),\ \theta)$ denote the semivariogram model with the vector of parameters θ. The weighted least squares estimates θ which minimizes the objective (cost) function:

$$F(\theta) = \sum_{j}^{k} w(j) \cdot [\hat{\gamma}(h(j)) - \gamma(h(j),\theta)]^2 , \tag{6.13}$$

where $w(j)$ is a weight function. Five weight functions can be applied to equation (6.13) (Pardo-Iguzqiza, 1999):

(1) $w(j) = 1.0$. (6.14)

This is a constant weight which is given to the ordinary squares fitting.

(2) $w(j) = N_{h(j)}$. (6.15)

This weight function considers the number of data pair only, so that the more weight is applied to the experimental variogram points where more data points are used, which gives a more statistically reliable result.

(3) $w(j) = [\gamma(h(j), \theta)]^{-2}$. (6.16)

This weight function considers the theoretical semivariogram only, so that the more weight is given to those experimental variogram points which are close to the origin than those far from the origin.

(4) $w(j) = N_{h(j)} \cdot [\gamma(h(j), \theta)]^{-2}$. (6.17)

This weight function, suggested by Cresis (1985), is the combination of weight functions given in (2) and (3), so that it has advantages from both: being statistical reliable and a good fitting the semivariogram near the origin. The latter is an attractive property. Stein and Handcock has shown that if the semivariogram model is applied to the kriging, then the fit of the model near the origin is more important than the fit at larger lags (Stein et al.,1989). However, there are some drawbacks with this weight function (Zhang et al., 1995): (i) it is a function of the parameters to be determined by the optimization program and the sum of weights differs in the iterations, which can cause problems such as slow convergence, local convergence or divergence; (ii) objective function (6.13) does not yield the same cost for a positive or a negative deviation.

(5) $w(j) = N_{h(j)} \cdot h(j)^{-2}$. (6.18)

This weight function was promoted by Zhang et al. (1995). Analogous to weight function given in (4), it emphasizes “a good fit near the origin”; but it utilizes the factor $h(j)$ instead of the theoretical semivariogram $\gamma(h(j), \theta)$. Since there is no statistical argument for introducing the factor $h(j)$, the weights $N_{h(j)} \cdot h(j)^{-2}$ in the objective function are constant during the iterations. Thus, this weight function overcomes the drawbacks of the fourth weight function, but keeps the merits of it.

This thesis utilizes the fifth weight function for semivariogram modeling.

The convergence criterion for nonlinear regression process is set to be (Nielsen, 2007):

$$\frac{\vec{k}^T P \vec{k}}{\hat{v}^T P \hat{v}} < 1.00001 \quad (6.19)$$

where $\vec{k}$ is a vector of variables: $\vec{l} - F(\theta^*)$ ($\vec{l}$ is a vector of observations; $\vec{\theta}^*$ is a vector of estimated parameters at current iterative step; $F(\theta^*)$ is the value of a theoretic parametric model for $\vec{\theta}^*$), P is the weight matrix and $\hat{v}$ is a vector of estimated residual error (Nielsen, 2007). The experiments show that the iterative numbers of the convergence for those three theoretic models are usually 2 to15.

An example of estimating semivariogram process is shown in Figure 6.3.

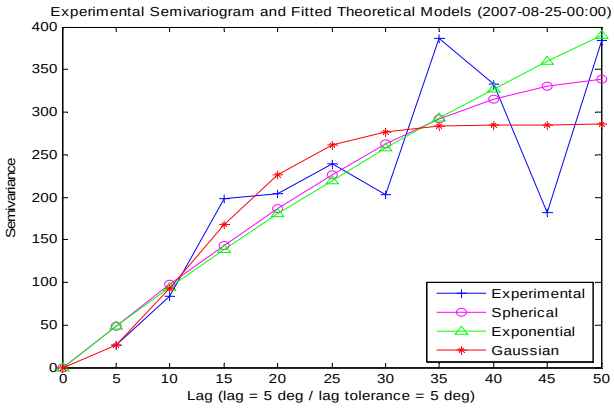

Figure 6.3 An example plot of estimating semivariogram process

3. Best fitted semivariogram model determination

In regular regression case, the least RMSE (Root Mean Squared Error) could be used as the test criteria, *i.e.* the best model is chosen from those models which have the least RMSE. In our nonlinear regression, the experimental values are weighted in proportion to the numbers of pairs contributing to them, but pay no attention to the lag. Thus, the model determined according to RMSE is not necessarily the best for kriging since the points near the target point get more weight than more distant ones (Webster et al., 2001).

The cross-validation process is a practical way to evaluate this issue. It is performed in three steps (Webster et al., 2001):

(1) An experimental semivariogram is computed from the whole sample dataset and the different theoretical models are fitted to it (as it is done above).

(2) For each model, each sample data value $z(\vec{x}_i)$ is deleted in turn and then Z is estimated at each sampling point is estimated from the rest of the data. The kriging variance $\hat{\sigma}^2(x_i)$ is also calculated.

(3) Three diagnostic statistics are calculated from the results:

(a) the mean deviation or mean error, ME:

$$ME = \frac{1}{N}\sum_{i=1}^{N}[z(x_i) - \hat{z}(x_i)]; \tag{6.20}$$

(b) the mean squared error, MSE:

$$MSE = \frac{1}{N}\sum_{i=1}^{N}[z(x_i) - \hat{z}(x_i)]^2; \tag{6.21}$$

(c) the mean squared deviation ratio, MSDR, which is calculated from the squared errors and kriging variance, $\hat{\sigma}^2(x_i)$, by:

$$MSDR = \frac{1}{N}\sum_{i=1}^{N}\frac{[z(x_i) - \hat{z}(x_i)]^2}{\hat{\sigma}^2(x_i)}. \tag{6.22}$$

The ME should be 0 since kriging is unbiased. However, the calculated ME is not a strong diagnostic because kriging is not sensitive to inaccuracies in the semivariogram (Webster et al., 2001). The less the MSE is, the more accurate the fitted model is. If the fitted model is accurate then MSE should be equal to the kriging variance and the MSDR should be 1. In this thesis, the diagnostic MSE is mainly used to choose the best fitted model for ordinary kriging.

Another way to evaluate the fitted model performance with kriging is to plot the scatterplot of the true values versus their estimated values (obtained in the above step (2)) and do regression analysis between them. In the best situation, it is expected that the estimator is conditionally unbiased, i.e. (Webster et al., 2001)

$$E\left[Z(\vec{x}_0) \mid \hat{Z}(\vec{x}_0)\right] = \hat{Z}(\vec{x}_0). \tag{6.23}$$

Based on this, it follows that the regression of $Z(\vec{x}_0)$ on $\hat{Z}(\vec{x}_0)$ is 1 (*i.e.* slope = 1). For ordinary kriging, the regression coefficient is somewhat less than 1 (Webster et al., 2001).

In this thesis, both *diagnostic statistics* and *scatterplots* are examined to evaluate each semivariogram model performance and then determine the best one for kriging.

6.1.2.3 Stage three: Prediction and interpolation

After structure analysis (*i.e.* semivariogram modeling/estimating), predictions at unsampled locations are made by ordinary kriging. Kriging is an "optimal prediction" (Bailey et al., 1995). It provides a solution to the problem of estimation based on a continuous model of stochastic spatial variation, such as semivariogram model. Among the geostatitical interpolation procedures, "ordinary kriging" is the most common type of kriging in practice. In this section, the basic of kriging is briefly presented.

1. Theory of kriging

Ordinary kriging assumes that the process to be predicted, $Z(\vec{s})$, has a unknown, constant mean value μ. It estimates the unknown value at an un-sampled point $\vec{s}$ by $\hat{Z}(\vec{s})$ using a weighted linear combination of the available sample (Bailey et al. 1995):

$$\hat{Z}(\vec{s}) = \sum_{i=1}^{n} \omega_i(\vec{s}) Z(\vec{s}_i) \tag{6.24}$$

where $\omega_i(\vec{s})$ are weights assigned to each sample point $\vec{s}_i$ (see Figure 6.4) and

$$\sum_{i=1}^{n} \omega_i(\vec{s}) = 1. \tag{6.25}$$

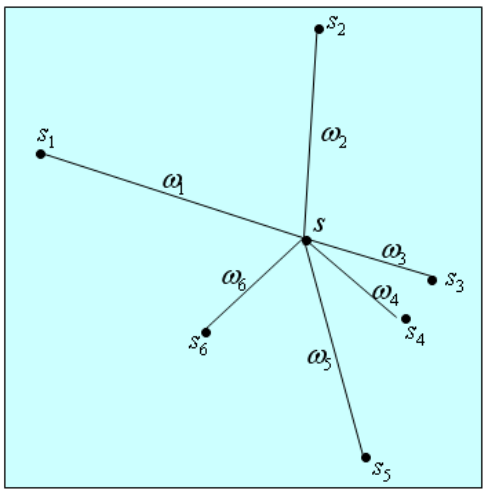

Figure 6.4 Kriging weighting scheme

The error variance is:

$$
\begin{aligned}
& E\left\{\left[\hat{Z}(\vec{s})-Z(\vec{s})\right]^2\right\} \\
& = E\left[\hat{Z}^2(\vec{s})\right]+E\left[Z^2(\vec{s})\right]-2E\left[Z(\vec{s})\hat{Z}^2(\vec{s})\right] \\
& = \sum_{i=1}^{n}\sum_{j=1}^{n}\omega_i(\vec{s})\cdot\omega_j(\vec{s})\cdot C(\vec{s}_i,\vec{s}_j)+\sigma^2-2\sum_{i=1}^{n}\omega_i(\vec{s})\cdot C(\vec{s},\vec{s}_i) \\
& = \omega^T(\vec{s})\cdot C\cdot\omega(\vec{s})+\sigma^2-2\omega^T(\vec{s})\cdot c(\vec{s}) \qquad (6.26)
\end{aligned}
$$

where C is the $(n\times n)$ matrix of covariance, $C(\vec{s}_i,\ \vec{s}_j)$ between all possible pairs of the *n* sample points and $c(\vec{s})$ is an $(n\times 1)$ column vector of covariances, $C(\vec{s},\ \vec{s}_i)$, between the predicted point $\vec{s}$ and each of the *n* sample point $\vec{s}_i$.

Just like the least-squares variance, ordinary kriging minimizes the error variance, subject to (6.25). This is achieved by Lagrance multiplier approach. Consider the following Langrangian

$$L=\omega^T(\vec{s})\cdot C\cdot\omega(\vec{s})+\sigma^2-2\omega^T(\vec{s})\cdot c(\vec{s})+2\left(\omega^T\vec{1}-1\right)\cdot\nu(\vec{s}) \qquad (6.27)$$

where $\nu(\vec{s})$ is the Lagrange multiplier and σ^2 is the *maximum semivariance* (*i.e. sill*) . Differentiating (6.27) with respect to both $\nu(\vec{s})$ and $\omega(\vec{s})$

$$
\begin{aligned}
& \frac{\partial L}{\partial\omega(\vec{s})}=0, \\
& \frac{\partial L}{\partial\nu(\vec{s})}=0,
\end{aligned}
$$

leads to

$$
\begin{aligned}
& \omega^T\cdot\vec{1}=1 \\
& C\cdot\omega(\vec{s})+\vec{1}\cdot\nu(\vec{s})=c(\vec{s})
\end{aligned}
$$

which can be also represented in a matrix form:

$$C_+\cdot\omega_+=c_+ \qquad (6.28)$$

where

$$C_+ = \begin{bmatrix} C(\vec{s}_1,\vec{s}_1)C(\vec{s}_1,\vec{s}_2) & ... & C(\vec{s}_1,\vec{s}_n) & 1 \\ C(\vec{s}_2,\vec{s}_1)C(\vec{s}_2,\vec{s}_2) & ... & C(\vec{s}_2,\vec{s}_n) & 1 \\ . \quad . & ... & . \quad . & . \\ . \quad . & ... & . \quad . & . \\ C(\vec{s}_n,\vec{s}_1)C(\vec{s}_n,\vec{s}_2) & ... & C(\vec{s}_n,\vec{s}_n) & 1 \\ 1 \quad 1 & ... & 1 \quad 0 & \end{bmatrix}, \ \omega_+ = \begin{bmatrix} \omega_1(\vec{s}) \\ \omega_2(\vec{s}) \\ . \\ . \\ \omega_n(\vec{s}) \\ \nu(s) \end{bmatrix} \text{ and } c_+ = \begin{bmatrix} C(\vec{s},\vec{s}_1) \\ C(\vec{s},\vec{s}_2) \\ . \\ . \\ C(\vec{s},\vec{s}_n) \\ 1 \end{bmatrix}.$$

Matrix C_+ is inverted, and the weights and the Lagrange multiplier are obtained as

$$\omega_+ = C_+^{-1} \cdot c_+ . \tag{6.29}$$

Note: (i) that C_+ would be unknown and it has to be derived from the estimated semivariogram model according to $C(h) = \sigma^2 - \gamma(h)$, where σ^2 is the maximum semivariance (*i.e.*, *sill*), which that shows how the semivariogram model is applied to kriging process; (ii) that through entire kriging process matrix C_+ only has to be done once, since it is not dependent on the prediction point $\vec{s}$; (iii) that for each new point $\vec{s}$ the only calculation is the change of c_+.

The ordinary kriging variance is given by

$$\sigma_e^2 = \sigma^2 - c_+^T C_+^{-1} c_+ . \tag{6.30}$$

To obtain the prediction, $\hat{Z}(\vec{s})$, the weight vector $\omega(\vec{s})$ is further extracted from ω_+, equation (6.29), and then substituted into equation (6.29) and solved.

The ordinary kriging equations (6.28) and (6.29) can be represented using semivariogram as below:

$$\omega_+ = \Gamma_+^{-1} \gamma_+ \tag{6.31}$$

and

$$\sigma_e^2 = \gamma_+^T \Gamma_+^{-1} \gamma_+ \tag{6.32}$$

where

$$\Gamma_+ = \begin{bmatrix} \gamma(\vec{s}_1,\vec{s}_1)\gamma(\vec{s}_1,\vec{s}_2) & \ldots & \gamma(\vec{s}_1,\vec{s}_n) & 1 \\ \gamma(\vec{s}_2,\vec{s}_1)\gamma(\vec{s}_2,\vec{s}_2) & \ldots & \gamma(\vec{s}_2,\vec{s}_n) & 1 \\ . \quad . & \ldots & . \quad . & . \\ . \quad . & \ldots & . \quad . & . \\ \gamma(\vec{s}_n,\vec{s}_1)\gamma(\vec{s}_n,\vec{s}_2) & \ldots & \gamma(\vec{s}_n,\vec{s}_n) & 1 \\ 1 \quad 1 & \ldots & 1 \quad 0 & \end{bmatrix}, \quad \omega_+ = \begin{bmatrix} \omega_1(\vec{s}) \\ \omega_2(\vec{s}) \\ . \\ . \\ \omega_n(\vec{s}) \\ \nu(s) \end{bmatrix} \text{ and } \gamma_+ = \begin{bmatrix} \gamma(\vec{s},\vec{s}_1) \\ \gamma(\vec{s},\vec{s}_2) \\ . \\ . \\ \gamma(\vec{s},\vec{s}_n) \\ 1 \end{bmatrix}.$$

6.2 Implementation of ordinary kriging

The preceding geostatistical approach process has been implemented in a Matlab program, which derives hourly PWV maps using the support from the real-time GPS PPP-inferred water vapor system.

The program flowchart is shown in Figure 6.5, where each function is matched with a Matlab file:

(1) Calculate/Estimate experimental semivariogram,

(2) Fitting theoretical semivariogram models,

(3) Selecting the best fitted model by cross-validation,

(4) Interpolating with ordinary kriging, and

(5) Output hourly PWV maps and associated kriging standard error maps.

The current ordinary kriging program does not take account of the difference of elevation.

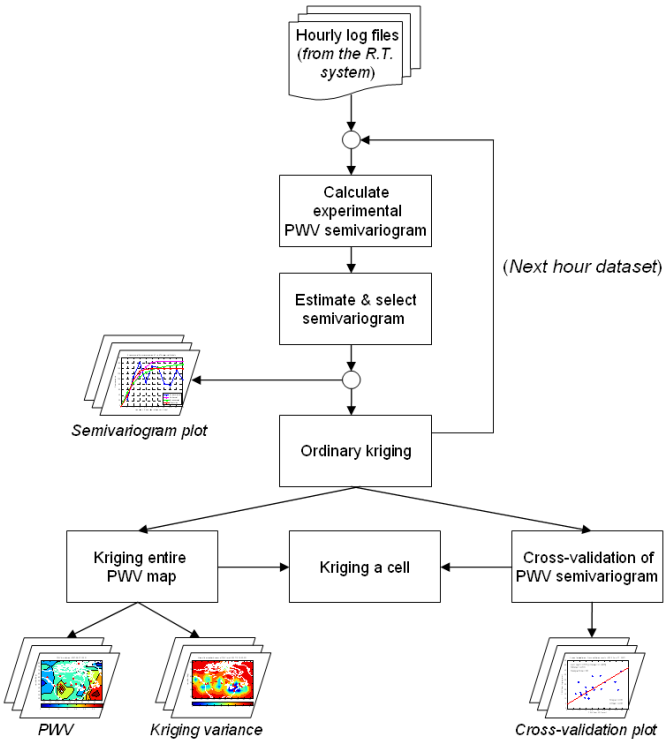

Figure 6.5 Flowchart for ordinary kriging program
(This program includes: (1) calculating experimental semivariogram, (2) fitting semivariograms, (3) selecting best fitted semivariogram model by cross-validation, (4) ordinary kriging interpolation, and (5) producing hourly PWV maps and associated standard error maps.)

6.3 Results and analysis

As it was mentioned in section 6.1.2.2, a statistically more reliable semivariogram needs a certain amount of observations for calculation. In the current Canada geodetic GPS network, (i) *19* out of *21* stations send both *GPS* and *MET* data in real-time stream and (ii) *NRC1* and *NRC3* share the same coordinates. The maximum number of the available observations used to estimate the PWV semivariogram is *18*. However, the current Canadian ground GPS station network is not working stably. Usually the available observation number is 15 ~ 17. In this section, the ordinary kriging program is executed on *24*-hour *18*-station datasets from the real-time GPS PPP-inferred water vapor system on August 25, 2007. The following analysis was performed hour by hour and the average values of each hour dataset were used. The analytic results include *semivariogram plots*,

cross-validation for PWV semivariogram performance, and *hourly PWV maps* and associated *kriging standard error maps*.

6.3.1 Semivariogram plots

The experimental semivariogram is calculated under the Latitude-Longitude coordinates system. The range of study area is between Longitudes -145° to -45° and Latitudes 28° to 85°. The optimal lag step length is determined to be 5-degree. Also, a 5-degree tolerance is selected since the observations are irregularly spaced in the study area. This means the number ($N_{h(j)}$) of observation pairs used to compute the semivariogram $\hat{\gamma}(h(j))$ for the lag $h(j)$ is calculated according to equation (6.9). The maximum lag is the half of the Longitude dimension of the study area ($-145^\circ \sim -45^\circ$), *i.e.* 50°. Figure 6.6 shows the pair numbers for each lag intervals. The 24-hour calculated experimental semivariograms are plotted in blue colour in Figure 6.8.

After hourly experimental semivariogram is computed, three theoretical models are fitted with it. Figure 6.8 shows hourly fitted models with the associated experimental semivariogram for 24 hour datasets. The zoomed in figure of fitted models is shown in Figure 6.7.

The fitted models' sills, ranges and RMSEs for 24-hour datasets are plotted in Figure 6.9, Figure 6.10 and Figure 6.11, respectively.

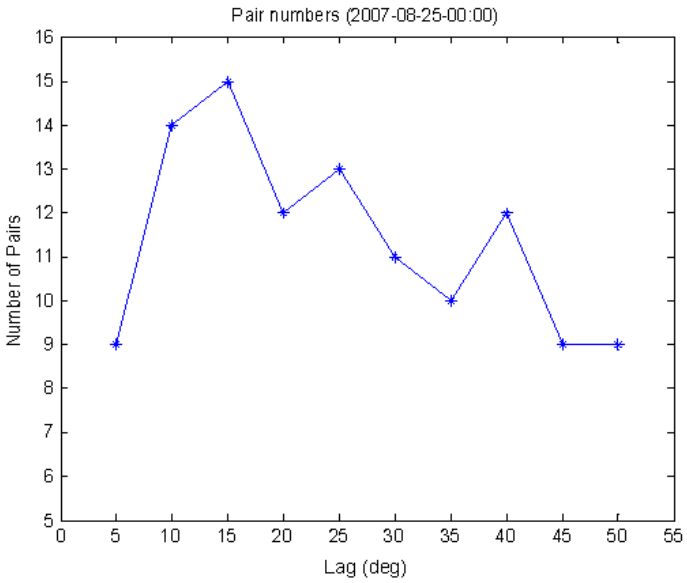

Figure 6.6 Plot of pair number for 2007-08-25-00:00 hour dataset

(The observations are irregularly spaced. The lag step is 5 degree. Lag tolerance is 5 degree. Maximum lag is 5 degree. The plot shows that the pair number decrease as the lag value increases)

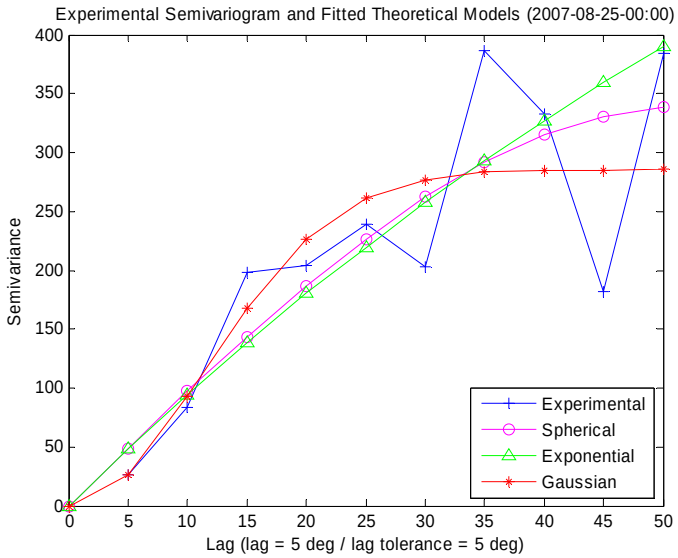

Figure 6.7 Semivariogram plot for 2007-08-25-00:00 dataset

(This plot is based on the optimal lag (5 degree) and Lag tolerance (5 degree). The plot shows that the Gaussian model is best fitted close to the origin and the Exponential and Spherical models are best fitted in the middle segment of the experimental semivariogram.)

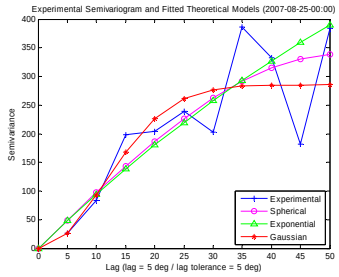

00:00

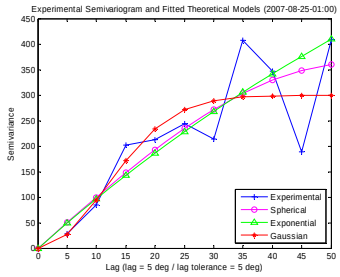

01:00

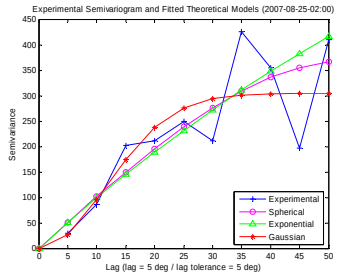

02:00

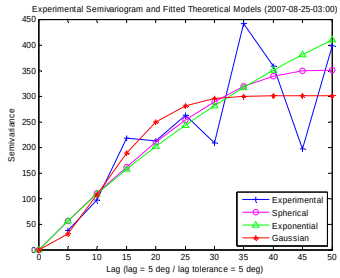

03:00

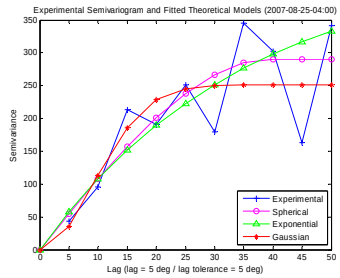

04:00

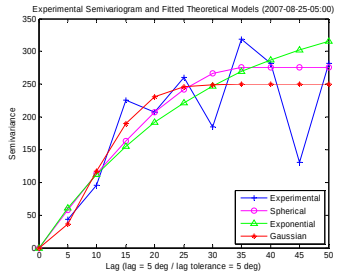

05:00

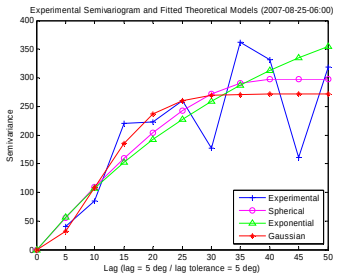

06:00

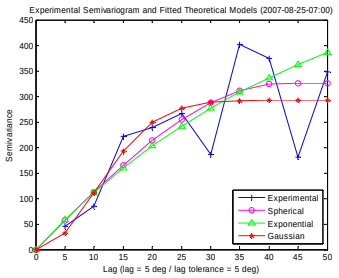

07:00

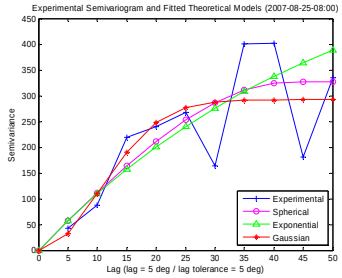

08:00

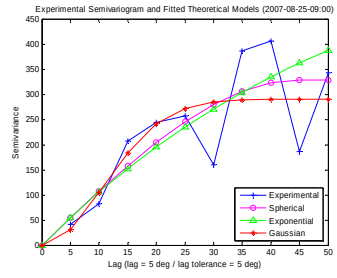

09:00

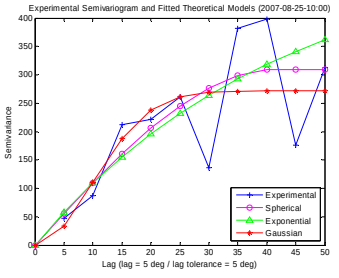

10:00

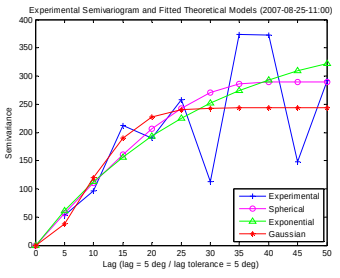

11:00

Figure 6.8 Hourly PWV experimental semivariogram plots (1)

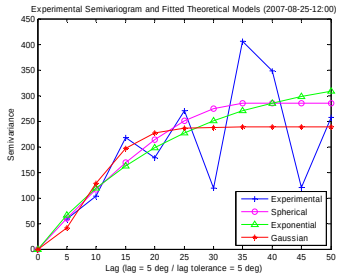

12:00

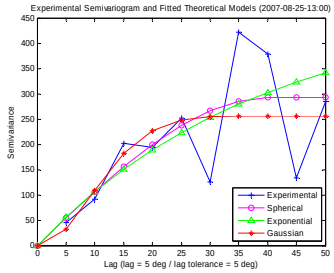

13:00

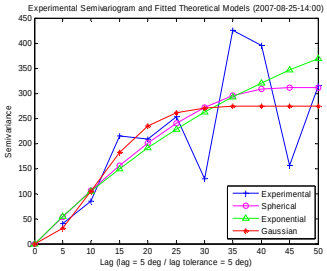

14:00

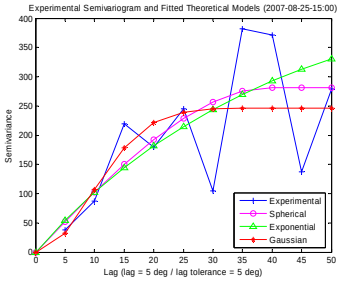

15:00

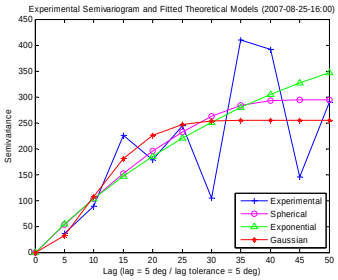

16:00

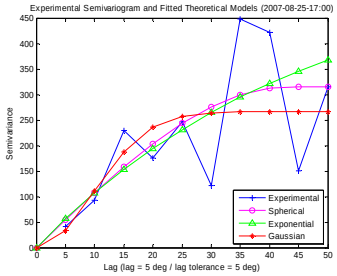

17:00

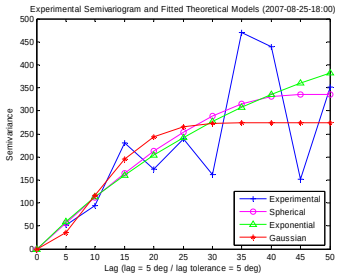

18:00

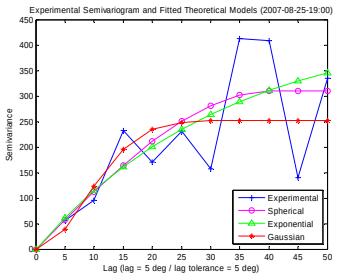

19:00

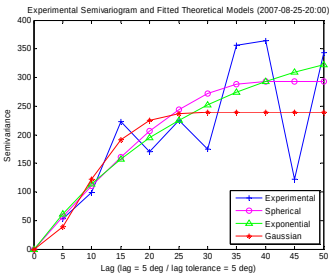

20:00

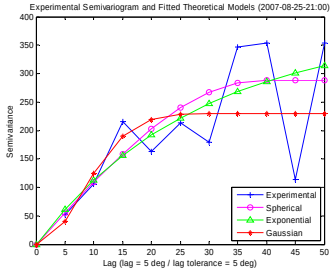

21:00

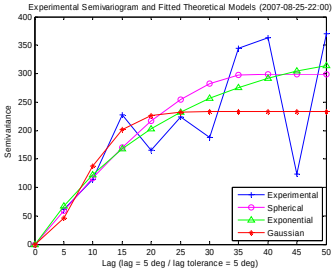

22:00

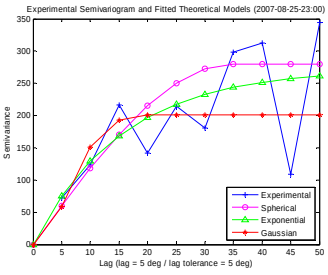

23:00

Figure 6.8 Hourly PWV experimental semivariogram plots (2)

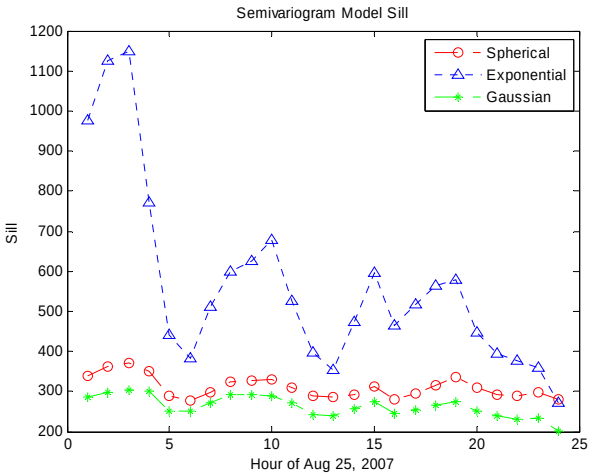

Figure 6.9 Sill plots of 24 hourly fitted semivariogram models

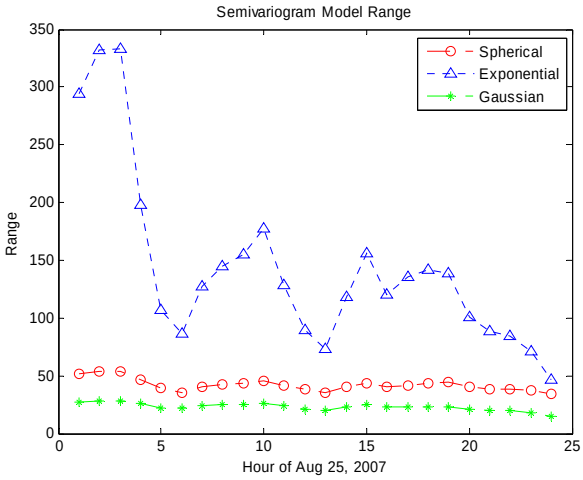

Figure 6.10 Range plots of 24 hourly fitted semivariogram models

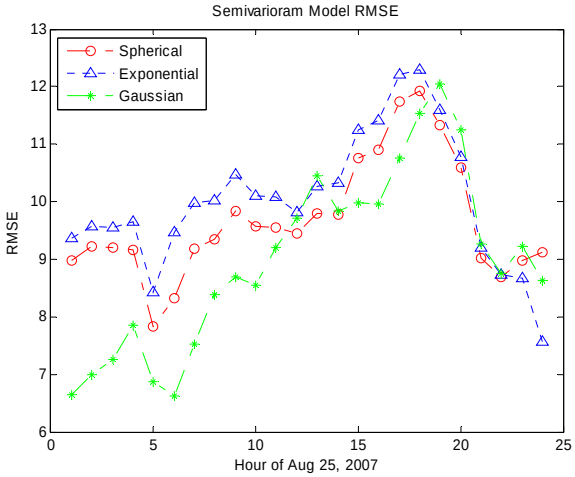

Figure 6.11 RMSE plots of 24 hourly fitted semivariogram models

Figure 6.7 and 6.8 show that (i) *Gaussian model* is fitted much more agreeably with the experimental semivariogram *near* the origin area than both *spherical* and *exponential models* are, (ii) *exponential model* is more agreeable with the *middle* segment of the experimental semivariogram than other two models are, and (iii) *spherical model* is fitted less than other two models are. It is common in geologic applications where there are correlations at different length scales. At small lag distances *h*, the smaller scale correlations dominate, while the large scale correlations dominate at larger lag distances (Webster and Oliver, 2001). Both (i) and (ii) indicate that a combination (nested model) of two semivariogram models, a *Gaussian model* and an *exponential model*, would be needed for better representation of the variance structure of PWV, the former is for small lag distance and the latter for the big lag distance, such as:

$$\gamma(h) = \begin{cases} c_1 \left[1 - exp\left(-\dfrac{3h}{a_1} \right)^2 \right] & for\ \ 0 < h \le a_1, \\ c_2 \left[1 - exp\left(-\dfrac{3h}{a_2} \right) \right] & for\ \ a_1 < h < a_2, \\ c_1 + c_2 & for\ \ h > a_2, \end{cases} \tag{6.33}$$

where c_1 and a_1 are the sill and range of the small lag distance (short-range component) of the variation, and c_2 and a_2 are the sill and range of the big lag distance (long-range component).

Figure 6.9 and Figure 6.10 indicate that (i) both *spherical* and *Gaussian models* have relatively stable sills and ranges (since both models reached their sills and ranges), and (ii) *exponential model*s have fluctuating sills and ranges. Since most of *exponential model*s did *not* reach their sill and range within the X-axis range, the Weighted Least Squares process estimated the sill and range under such condition which would not represent the flattening sill and corresponding range. A more reasonable sill/range value of the *exponential model* could be found at hour 23:00 where the *exponential model* almost reached its flattening sill state (see Figure 6.8 (2) and Figure 9 ~ 10).

Figure 6.11 indicates that (i) RMSE's varies greatly with hourly spatial data structure due to the low precision of the *small*-sample-size semivariogram; (ii) the order of RMSEs

of three models varies with the hourly data spatial structure, *i.e.* the data spatial structure affects each model differently; and (iii) the RMSE may be used to evaluate the agreement of a model fitness; but it can not be used to validate the best semivariogram model for kriging since in the above case of nonlinear regression the experimental values are weighted in proportion to the numbers of pairs contributing to them (Equation 6.15), without paying attention to the lag. The obtained model determined according to RMSE is not necessarily the best for kriging since the points near the target point get more weight than those far away from the target points (Webster and Oliver 2001).

Figure 6.9, 6.10 and 6.11 were obtained under small-sample data environment and the results from large-sample datasets need to be further tested.

6.3.2 Cross-validation for PWV semivariogram model performance

In this thesis, both diagnostic statistics and scatterplots are utilized to examine the performance of each fitted model and then select the best fitted model for ordinary kriging.

Through the experiments, it was found that for dataset dated on August 25, 2007, *all* 24 hourly kriged PWV maps from *spherical model* displayed negative values (see Figure 6.12); this obvious sign indicated that this model did not represent the true semivariogram for 24-hour PWV datasets. So, this model was deleted and the comparisons between *exponential* and *gaussion models* are conducted during the cross-validation process.

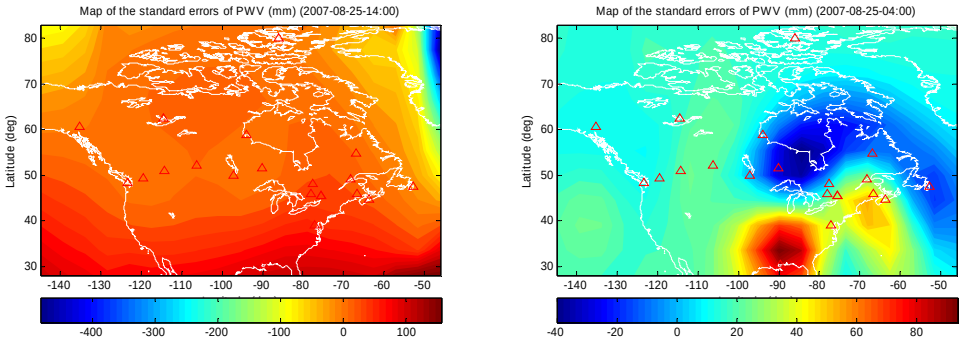

Figure 6.12 Negative kriged PWV maps from the Spherical model (left) and Gaussian model (right) (Negative PWV values indicate that the semivariogram model used for kriging is not reasonable for this hourly dataset)

- Cross-validation by three diagnostic statistics

24-hour diagnostic statistics are given in Table 6.1, where hourly MSEs for the better model are highlighted. The 24-hour diagnostic statistics are also plotted in Figure 6.13.

Table 6.1 Comparison of 24-hour diagnostic statistics from *exponential-model-based* and *Gaussian-model-based* ordinary kriging interpolations (on August 25, 2007).
(The MSE value of the better model is highlighted) (unit: mm)

	00:00			01:00			02:00		
	ME	MSE	MSDR	ME	MSE	MSDR	ME	MSE	MSDR
Exp. Mdl.	-1.85	**57.89**	0.32	-1.88	**60.76**	0.33	-1.82	**65.15**	0.38
Gusn. Mdl	-3.58	330.58	23.0	-4.98	531.24	34.64	-7.0	861.71	59.4

	03:00			04:00			05:00		
	ME	MSE	MSDR	ME	MSE	MSDR	ME	MSE	MSDR
Exp. Mdl.	-1.80	**77.80**	0.48	-1.46	**79.84**	0.56	-1.52	**83.19**	0.60
Gusn. Mdl	-7.36	825.95	46.25	-6.72	511.58	24.76	-4.98	235.00	13.24

	06:00			07:00			08:00		
	ME	MSE	MSDR	ME	MSE	MSDR	ME	MSE	MSDR
Exp. Mdl.	-1.53	**78.83**	0.58	-1.49	**81.82**	0.57	-1.49	**75.47**	0.50
Gusn. Mdl	-6.23	482.81	27.52	-7.83	761.41	44.90	-7.02	523.58	22.34

	09:00			10:00			11:00		
	ME	MSE	MSDR	ME	MSE	MSDR	ME	MSE	MSDR
Exp. Mdl.	-1.37	**70.74**	0.50	-1.32	**71.83**	0.51	-1.24	**79.06**	0.53
Gusn. Mdl	-7.01	534.52	33.50	-5.32	304.55	14.88	-4.68	279.44	8.45

	12:00			13:00			14:00		
	ME	MSE	MSDR	ME	MSE	MSDR	ME	MSE	MSDR
Exp. Mdl.	-1.21	**90.06**	0.57	-1.46	**71.06**	0.45	-1.45	**58.67**	0.38
Gusn. Mdl	-5.50	365.29	9.94	-6.30	475.81	21.26	-6.23	404.70	30.81

	15:00			16:00			17:00		
	ME	MSE	MSDR	ME	MSE	MSDR	ME	MSE	MSDR
Exp. Mdl.	-1.52	**57.99**	0.37	-1.62	**57.67**	0.34	-1.67	**63.17**	0.35
Gusn. Mdl	-3.50	113.96	3.91	-3.22	78.74	1.91	-2.82	64.63	0.99

	18:00			19:00			20:00		
	ME	MSE	MSDR	ME	MSE	MSDR	ME	MSE	MSDR
Exp. Mdl.	-1.61	**67.67**	0.37	-1.48	**65.30**	0.39	-1.50	**59.36**	0.37
Gusn. Mdl	0.43	187.91	15.41	0.09	146.18	7.17	0.18	110.97	4.80

	21:00			22:00			23:00		
	ME	MSE	MSDR	ME	MSE	MSDR	ME	MSE	MSDR
Exp. Mdl.	-1.54	**60.34**	0.37	-1.49	66.61	0.40	-1.16	81.48	0.51
Gusn. Mdl	0.44	118.54	5.79	-1.72	**45.17**	0.59	-1.68	**42.69**	0.51

Figure 6.13 shows that three diagnostic statistics of *exponential-model-based ordinary kriging interpolation* of PWV are much stable while those of *Gaussian-model-based ordinary kriging interpolation* varied through the day since the Gaussian model was well fitted only for short-range component (see Section 6.3.1). MSE behaviours shows that (i) from 00:00 to 21:00, *exponential-model-based ordinary kriging interpolation* was better than *Gaussian-model-based ordinary kriging interpolation* from 00:00 to 21:00; (ii) from 22:00 to 23:00, in reverse, *Gaussian-model-based ordinary kriging interpolation* is better than *exponential-model-based ordinary kriging interpolation*, and (iii) during 22:00 to 23:00, the MSE from *Gaussian-model-based ordinary kriging interpolation* is 42.69 ~ 45.17 mm, the smallest out of 24-hour datasets.

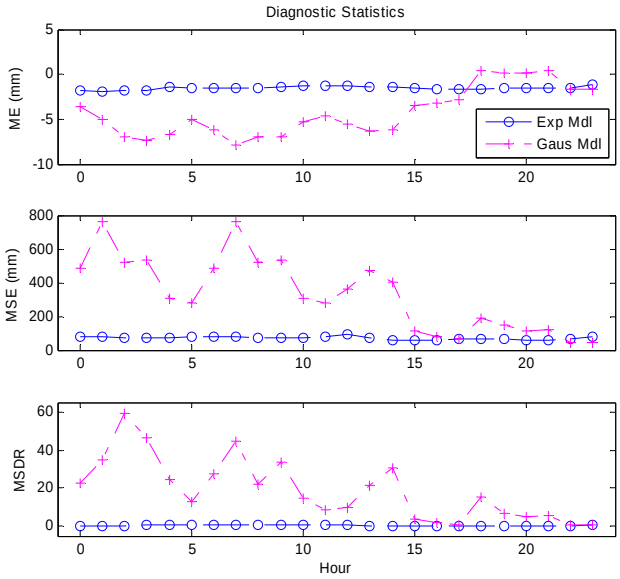

Figure 6.13 Plots of 24-hour diagnostic statistics (ME, MSE, MSDR) associated with

- Cross-validation by scatterplots

The 24-hour cross-validation scatterplots for both models are shown in Figure 6.14, where the left column is for *exponential-model-based ordinary kriging interpolation* and the right column is for *Gaussian-model-based ordinary kriging interpolation*. The associated linear regression parameters and statistics are printed on these figures. The linear regression parameters and statistics of the 24-hour cross-validation scatterplots are summarized in Table 6.2 and are also plotted in Figure 6.15.

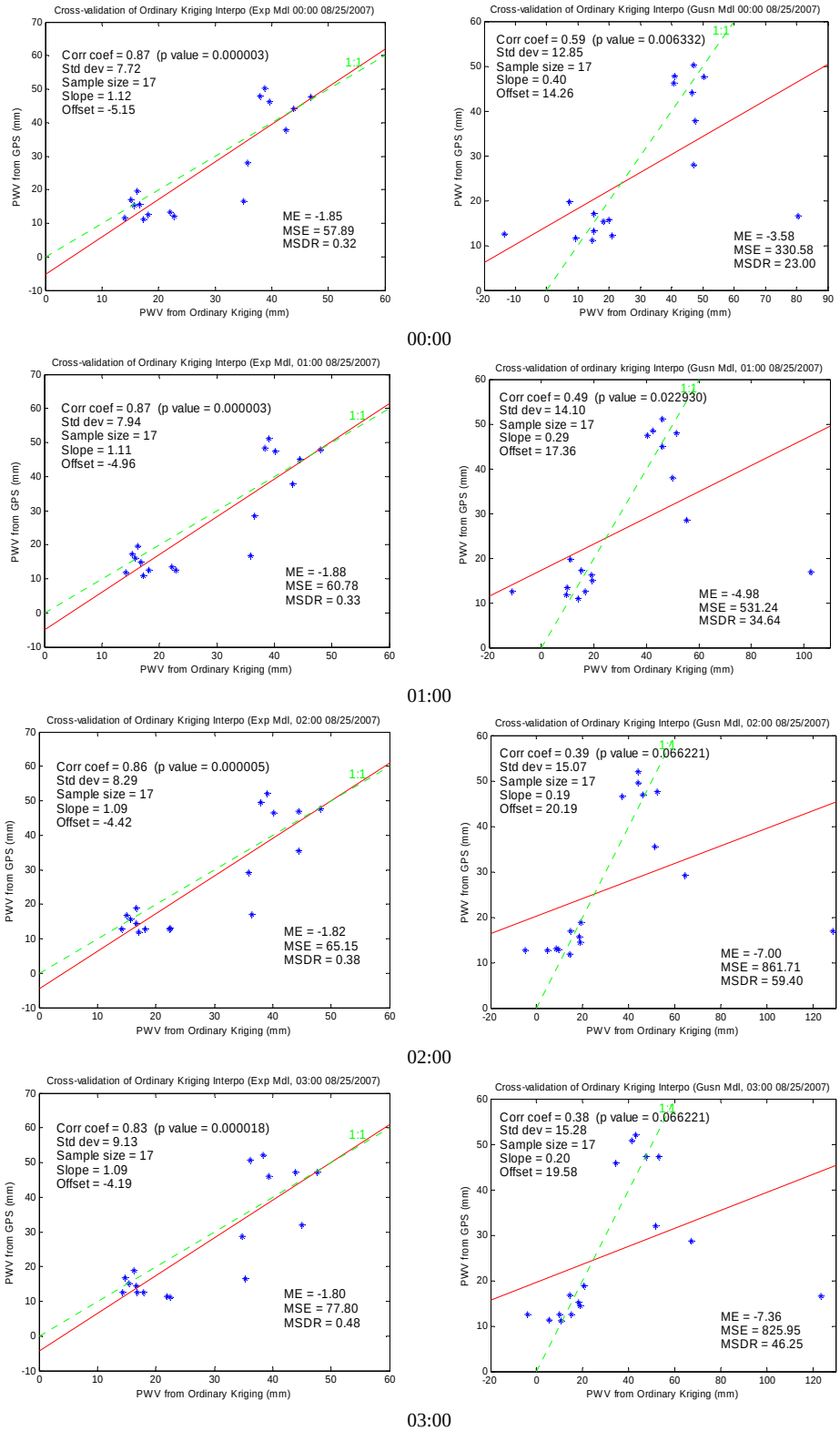

Figure 6.14 Scatterplots of cross-validation for Exponential model (left) and Gaussian model (right) (1)

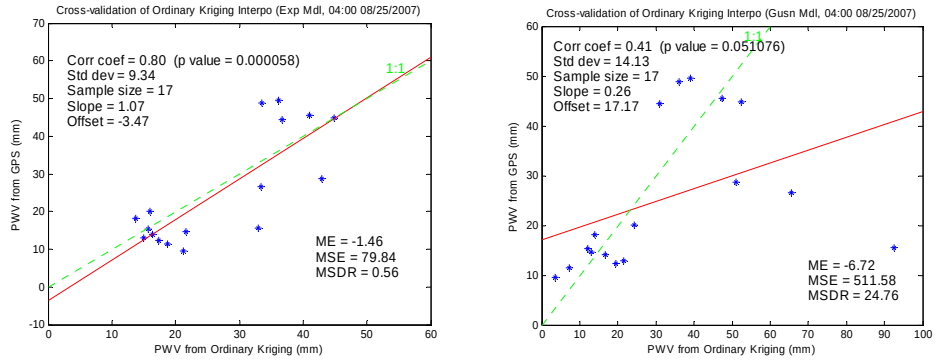

04:00

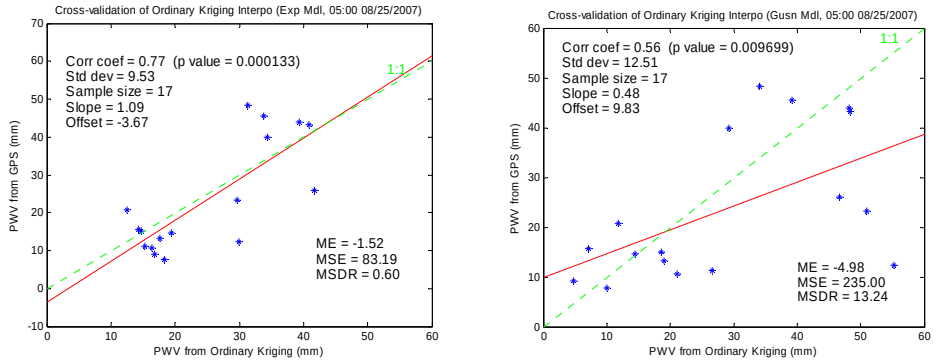

05:00

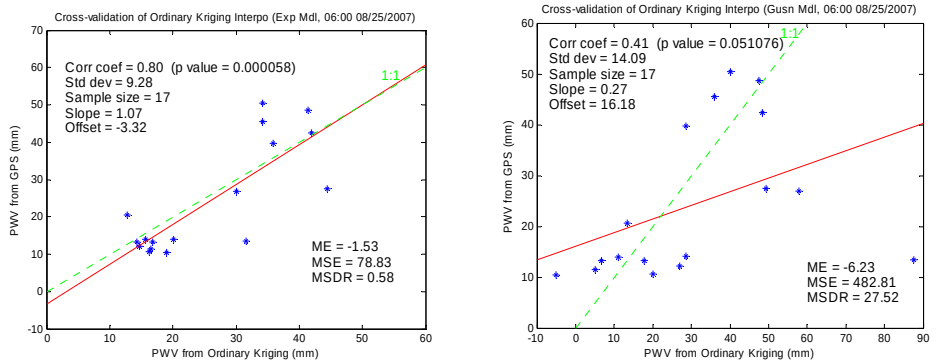

06:00

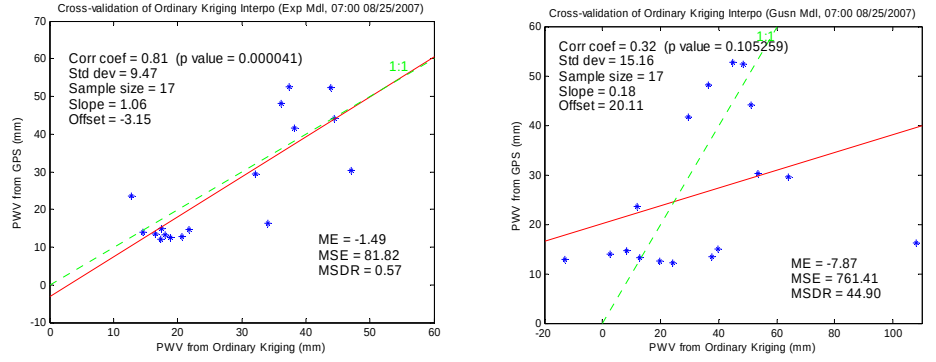

07:00

Figure 6.14 Scatterplots of cross-validation for exp. model (left) and Gaussian model (right) (2)

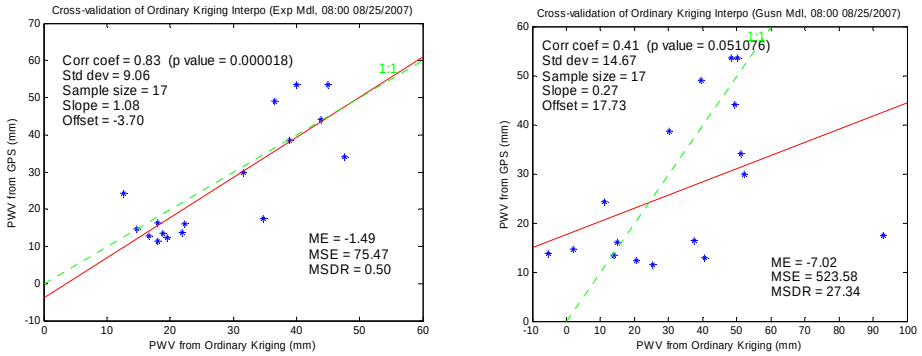

08:00

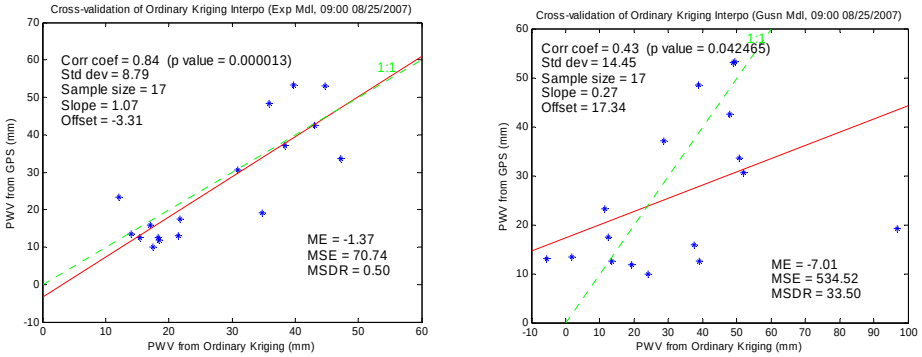

9:00

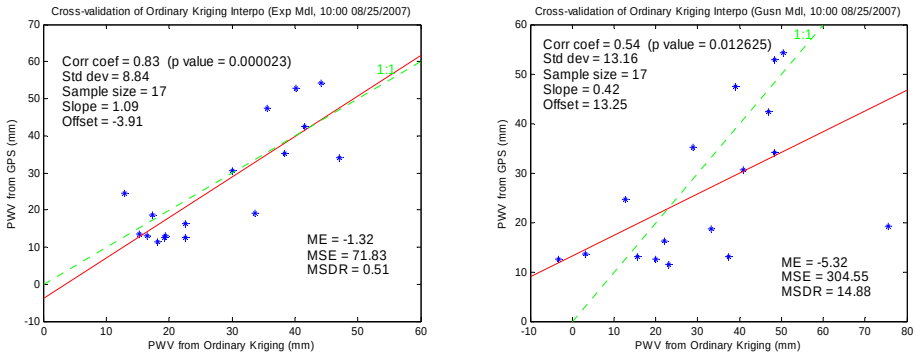

10:00

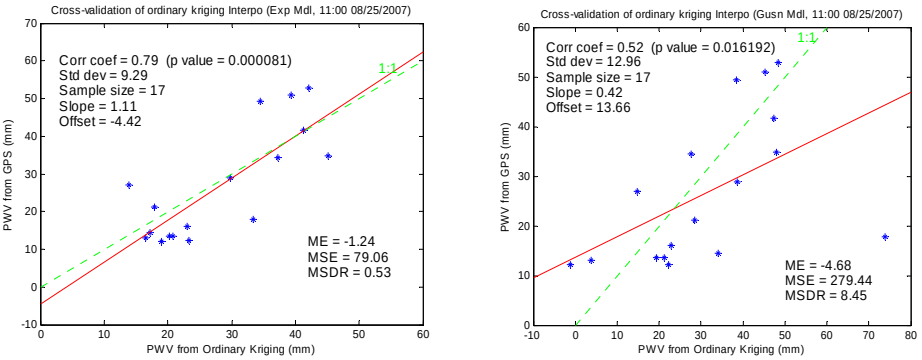

11:00

Figure 6.14 Scatterplots of cross-validation for Exponential model (left) and Gaussian model (right) (3)

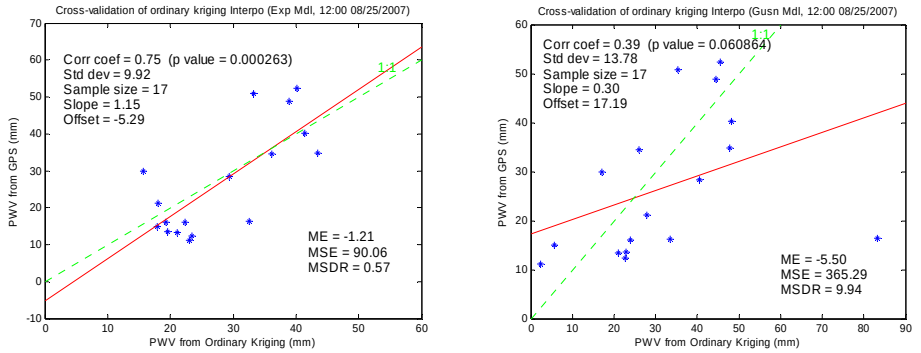

12:00

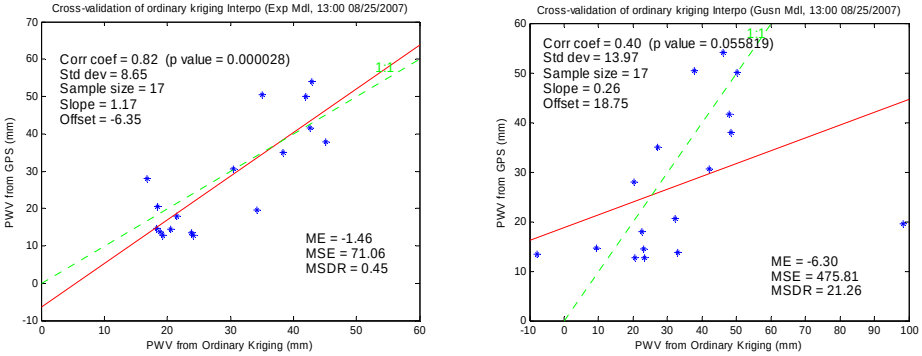

13:00

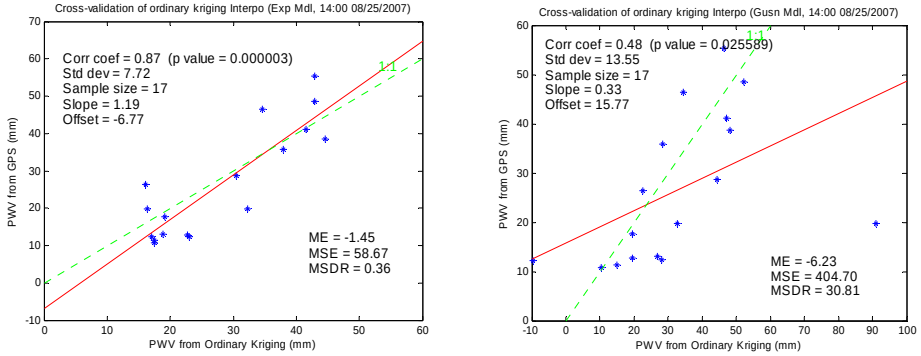

14:00

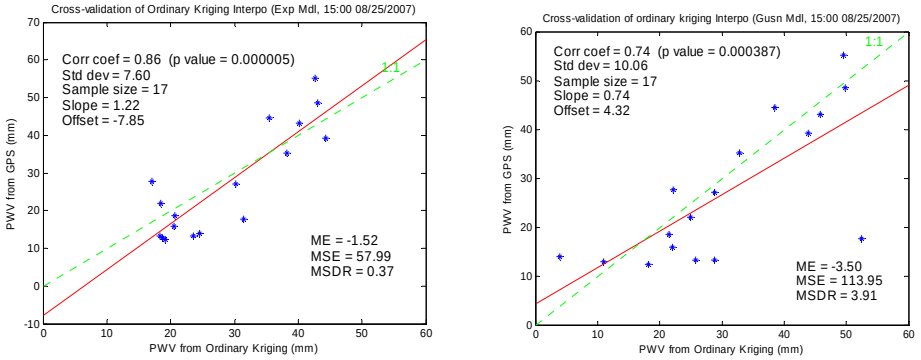

15:00

Figure 6.14 Scatterplots of cross-validation for Exponential model (left) and Gaussian model (right) (4)

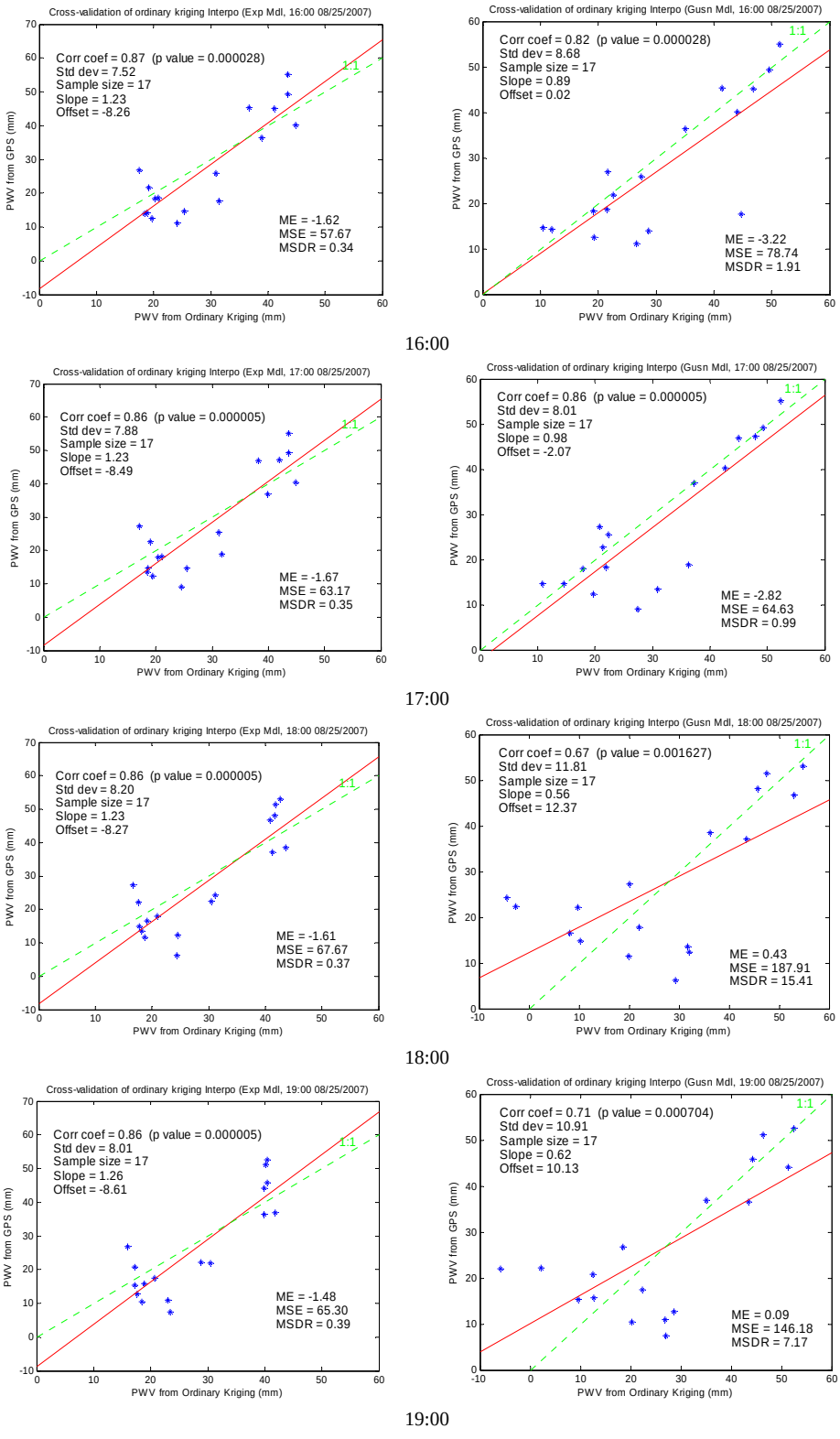

Figure 6.14 Scatterplots of cross-validation for Exponential model (left) and Gaussian model (right) (5)

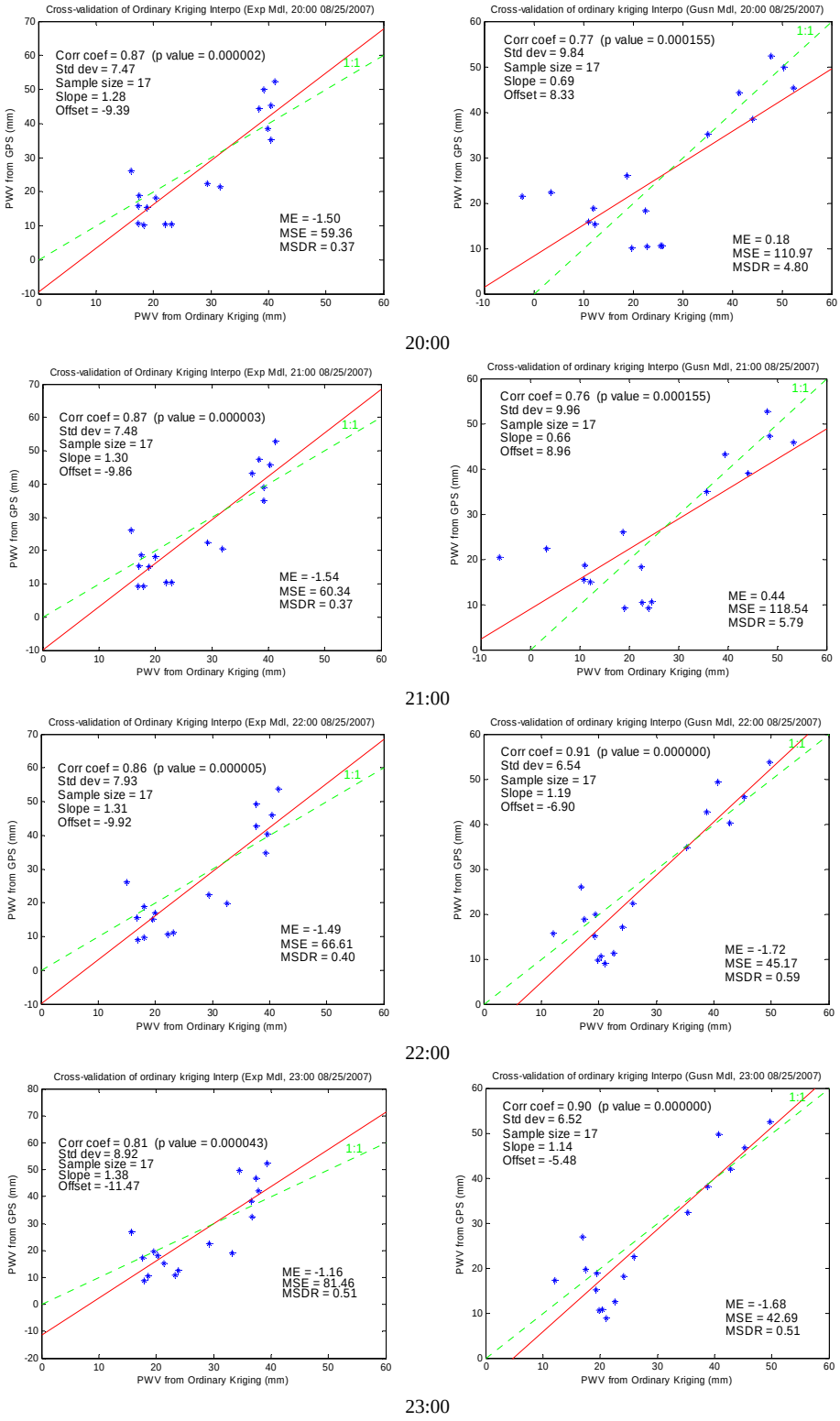

Figure 6-14 Scatterplots of cross-validation for Exponential model (left) and Gaussian model (right) (6)

Table 6.2 Comparison of linear regression parameters of 24-hour cross-validation scatterplots from *exp.-model-based OK interpolation* and *Gaussian-model-based OK interpolation* (on August 25, 2007).
(The STD value of the better model is highlighted) (unit: mm)

	00:00			01:00			02:00		
	Cor.Co	Std	Slope	Cor.Co	Std	Slope	Cor.Co	Std	Slope
Exp. Mdl.	0.87	**7.72**	1.12	0.87	**7.94**	1.11	0.86	**8.29**	1.09
Gusn. Mdl	0.59	12.85	0.40	0.49	14.10	0.29	0.39	15.07	0.19

	03:00			04:00			05:00		
	Cor.Co	Std	Slope	Cor.Co	Std	Slope	Cor.Co	Std	Slope
Exp. Mdl.	0.83	**9.13**	1.09	0.80	**9.34**	1.07	0.77	**9.53**	1.09
Gusn. Mdl	0.38	15.28	0.20	0.41	14.13	0.26	0.56	12.51	0.48

	06:00			07:00			08:00		
	Cor.Co	Std	Slope	Cor.Co	Std	Slope	Cor.Co	Std	Slope
Exp. Mdl.	0.80	**9.28**	1.07	0.81	**9.47**	1.06	0.83	**9.06**	1.08
Gusn. Mdl	0.41	14.09	0.27	0.32	15.16	0.18	0.41	14.67	0.27

	09:00			10:00			11:00		
	Cor.Co	Std	Slope	Cor.Co	Std	Slope	Cor.Co	Std	Slope
Exp. Mdl.	0.84	**8.79**	1.07	0.83	**8.84**	1.09	0.79	**9.29**	1.11
Gusn. Mdl	0.43	14.45	0.27	0.54	13.16	0.42	0.52	12.96	0.42

	12:00			13:00			14:00		
	Cor.Co	Std	Slope	Cor.Co	Std	Slope	Cor.Co	Std	Slope
Exp. Mdl.	0.75	**9.92**	1.15	0.82	**8.66**	1.17	0.87	**7.72**	1.19
Gusn. Mdl	0.39	13.78	0.30	0.40	13.97	0.26	0.48	13.55	0.33

	15:00			16:00			17:00		
	Cor.Co	Std	Slope	Cor.Co	Std	Slope	Cor.Co	Std	Slope
Exp. Mdl.	0.86	**7.60**	1.22	0.87	**7.52**	1.23	0.86	**7.88**	1.23
Gusn. Mdl	0.74	10.06	0.74	0.82	8.68	0.89	0.86	8.01	0.98

	18:00			19:00			20:00		
	Cor.Co	Std	Slope	Cor.Co	Std	Slope	Cor.Co	Std	Slope
Exp. Mdl.	0.86	**8.20**	1.23	0.86	**8.01**	1.26	0.87	**7.47**	1.28
Gusn. Mdl	0.67	11.81	0.56	0.71	10.91	0.62	0.77	9.84	0.69

	21:00			22:00			23:00		
	Cor.Co	Std	Slope	Cor.Co	Std	Slope	Cor.Co	Std	Slope
Exp. Mdl.	0.87	**7.48**	1.30	0.86	7.93	1.31	0.81	8.92	1.38
Gusn. Mdl	0.76	9.96	0.66	0.91	**6.54**	1.19	0.90	**6.52**	1.14

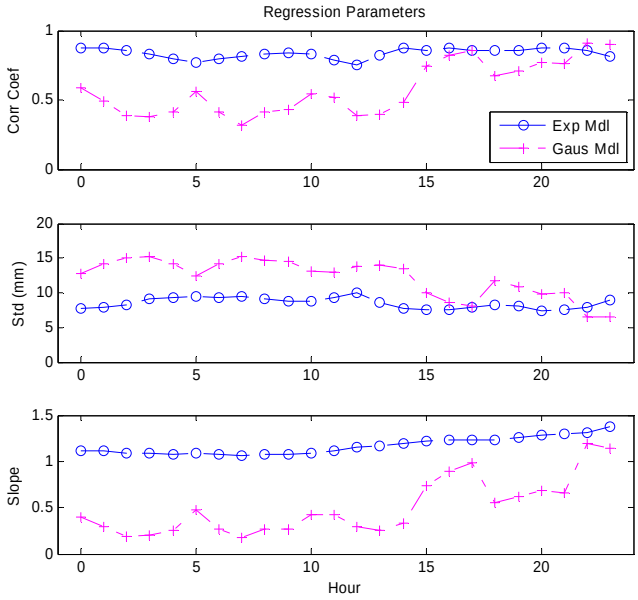

Figure 6.15 Plots of linear regression parameters of 24-hour cross-validation scatterplots
(The blue line is from Exponential.-model-based Ordinary Kriging interpolation and the pink line is from Gaussian-model-based OK interpolation. According to STD criterion, Exponential model is the better model for 00:00 to 21:00 datasets and Gaussian model is the better model for 22:00 to 23:00 datasets)

Figure 6.14 and 6.15 show that (i) The STD (regression standard error) decreases as the regression coefficient (slope of regression line) is close to 1 (in Figure 6.14, 'regression coefficient = 1' means that ordinary kriging-derived PWVs is totally consistent with the GPS-derived PWVs); in reverse, the regression standard error increase as the regression coefficient departs from 1 in either positive direction or negative direction; (ii) The regression coefficient is somewhat less than 1 for the ordinary kriging in the *best* case; (iii) According to STD, it derives the same conclusion as MSE does: (a) from 00:00 to 21:00, exponential model outperformed Gaussian model in ordinary kriging interpolation and (b) from 22:00 to 23:00, Gaussian model outperformed exponential model; (iv) Gaussian-model-based ordinary kriging interpolations from 22:00 to 23:00 provide the best results: Correlation coefficient = 0.90 ~ 0.91, Standard error = 6.52 ~ 6.54 and Slope = 1.14 ~ 1.15.

Based on both cross-validation results above, it was determined that the *exponential model* is for ordinary kriging from 00:00 to 21:00 and the *guassian model* from 22:00 to 23:00.

6.3.3 Kriginged PWV maps and associated kriging standard error maps

The 24-hour best-model-based ordinary kriginged PWV maps are shown in Figure 6.16, i.e. the kriginged PWV maps from 00:00 to 21:00 were based on exponential semivariogram model and the kriginged PWV maps from 22:00 to 23:00 were based on Gaussian semivariogram model.

These maps demonstrate the spatial and temporal natures of PWV overlaying Canada from coast to coast during this study period. Notice that the PWV maps from 22:00 to 23:00 show more details than the PWV maps from 00:00 to 21:00 do, since Gaussian model is fitted more agreeably with the experimental semivariogram near the origin than exponential model does (see Figure 6.7).

The 24-hour associated kriging standard error maps are shown in Figure 6.17. Figure 6.17 indicates that the higher accurate areas are found in area between Longitudes -125° to -60° and Latitudes 44° to 54° where most of GPS stations located and that the other areas outside have lower accuracy level due to the lack of information data, i.e. the area close to GPS station show high accuracy level.

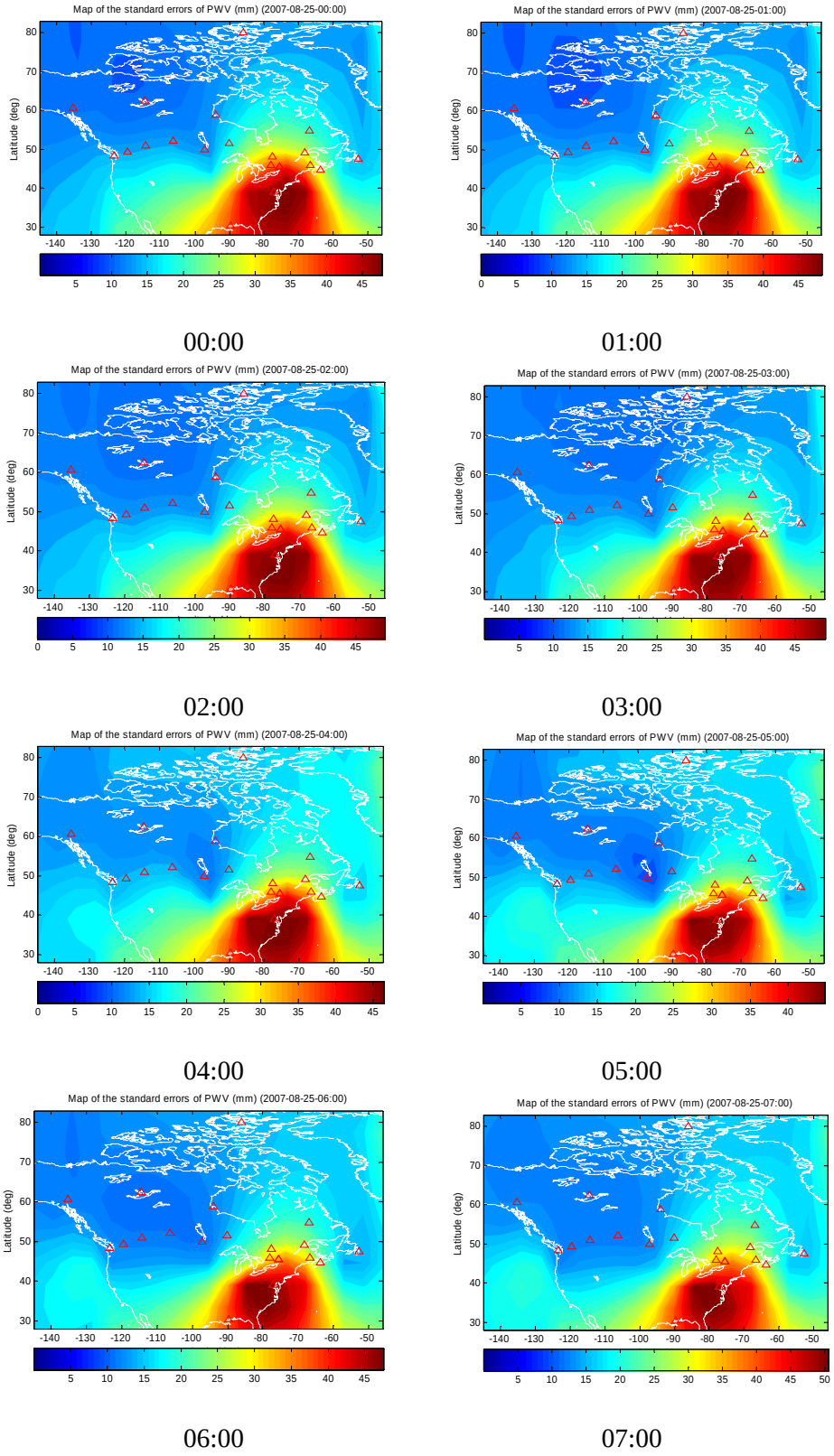

Figure 6.16 Hourly kriginged PWV maps (Horizontal axis = Longitude) (1)

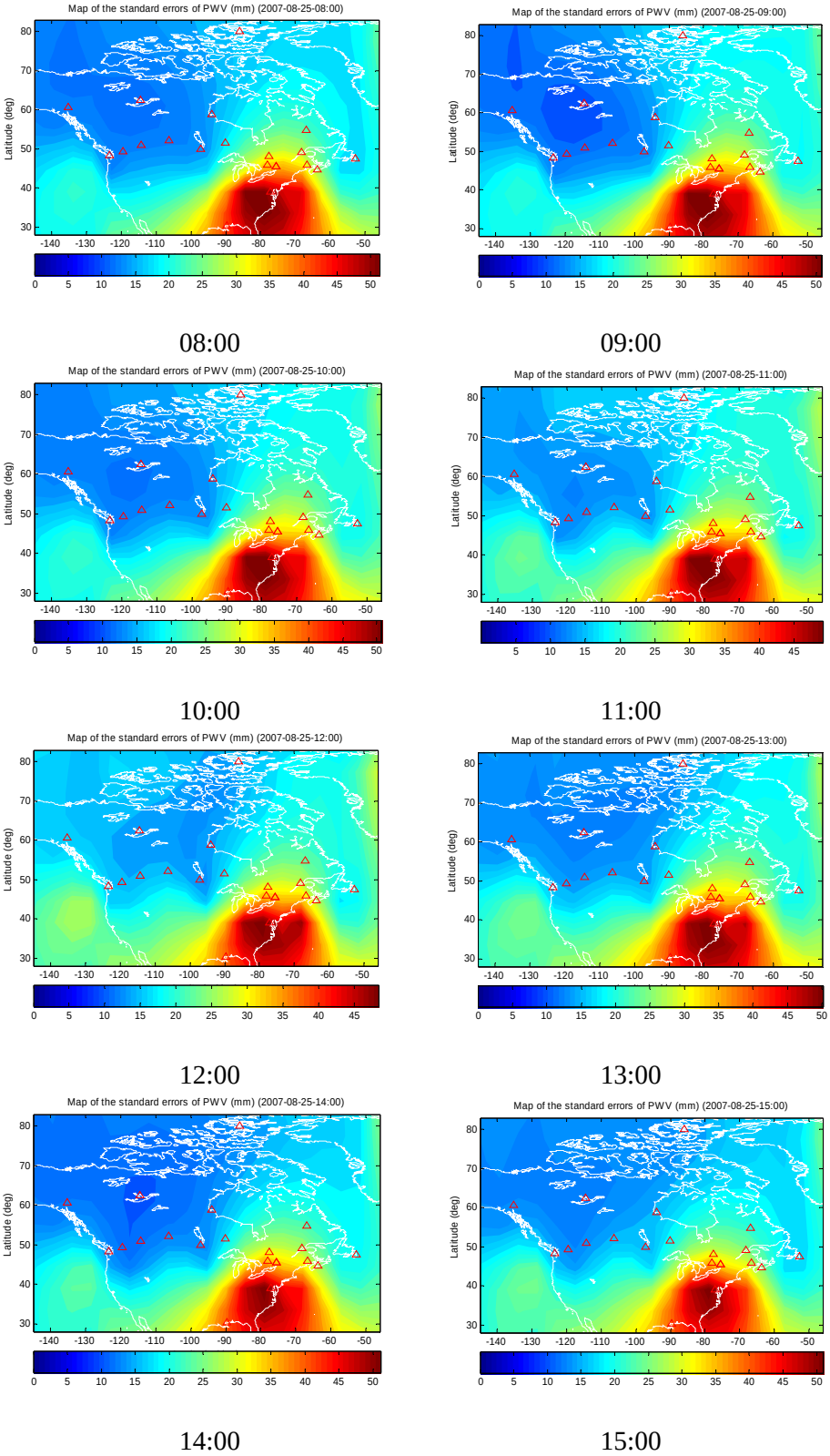

Figure 6.16 Hourly kriginged PWV maps (Horizontal axis = Longitude) (2)

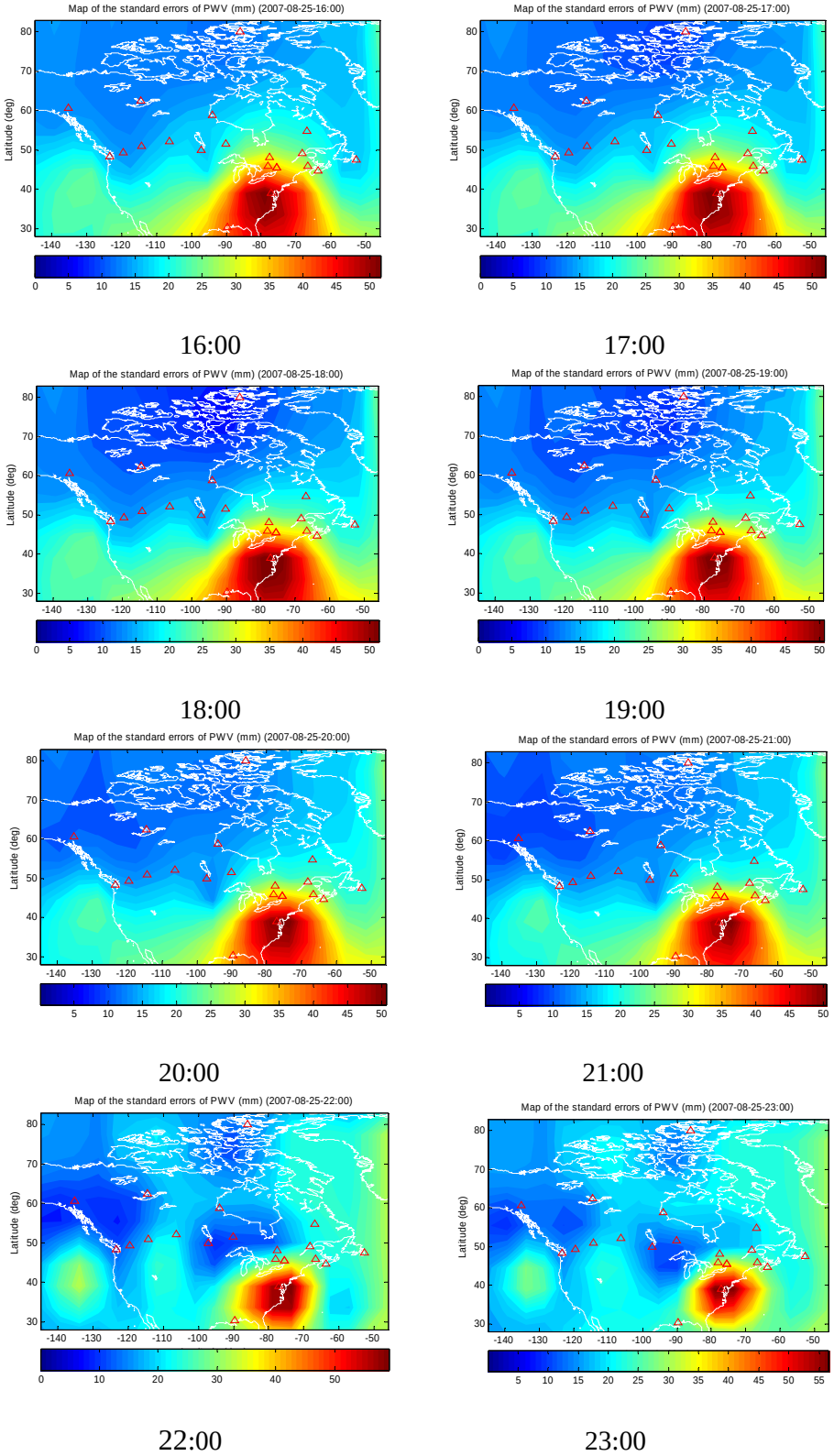

Figure 6-16 Hourly kriginged PWV maps (Horizontal axis = Longitude) (3)

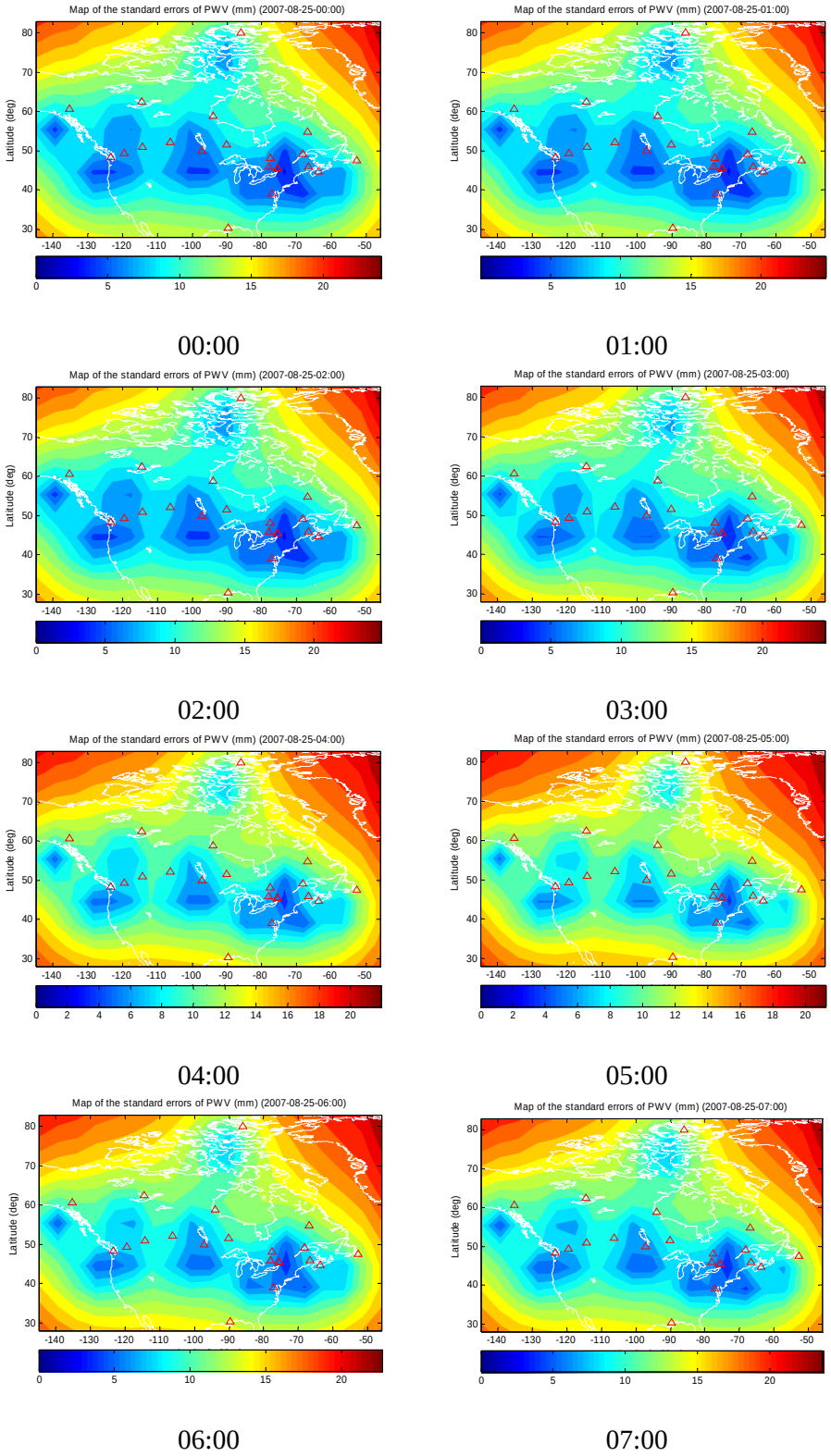

Figure 6.17 Hourly kriginged standard error maps (Horizontal axis = Longitude) (1)

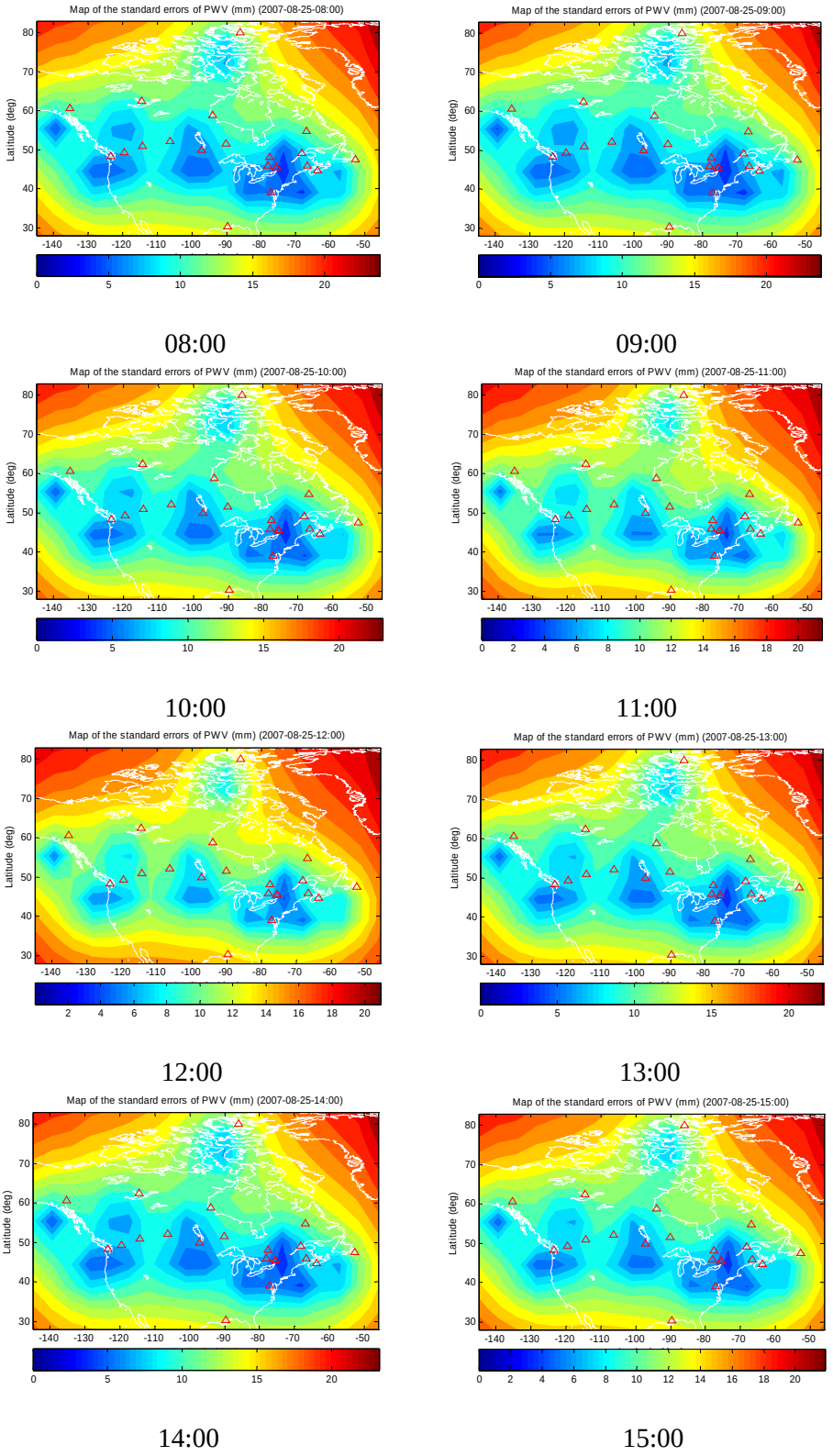

Figure 6.17 Hourly kriging standard error maps (Horizontal axis = Longitude) (2)

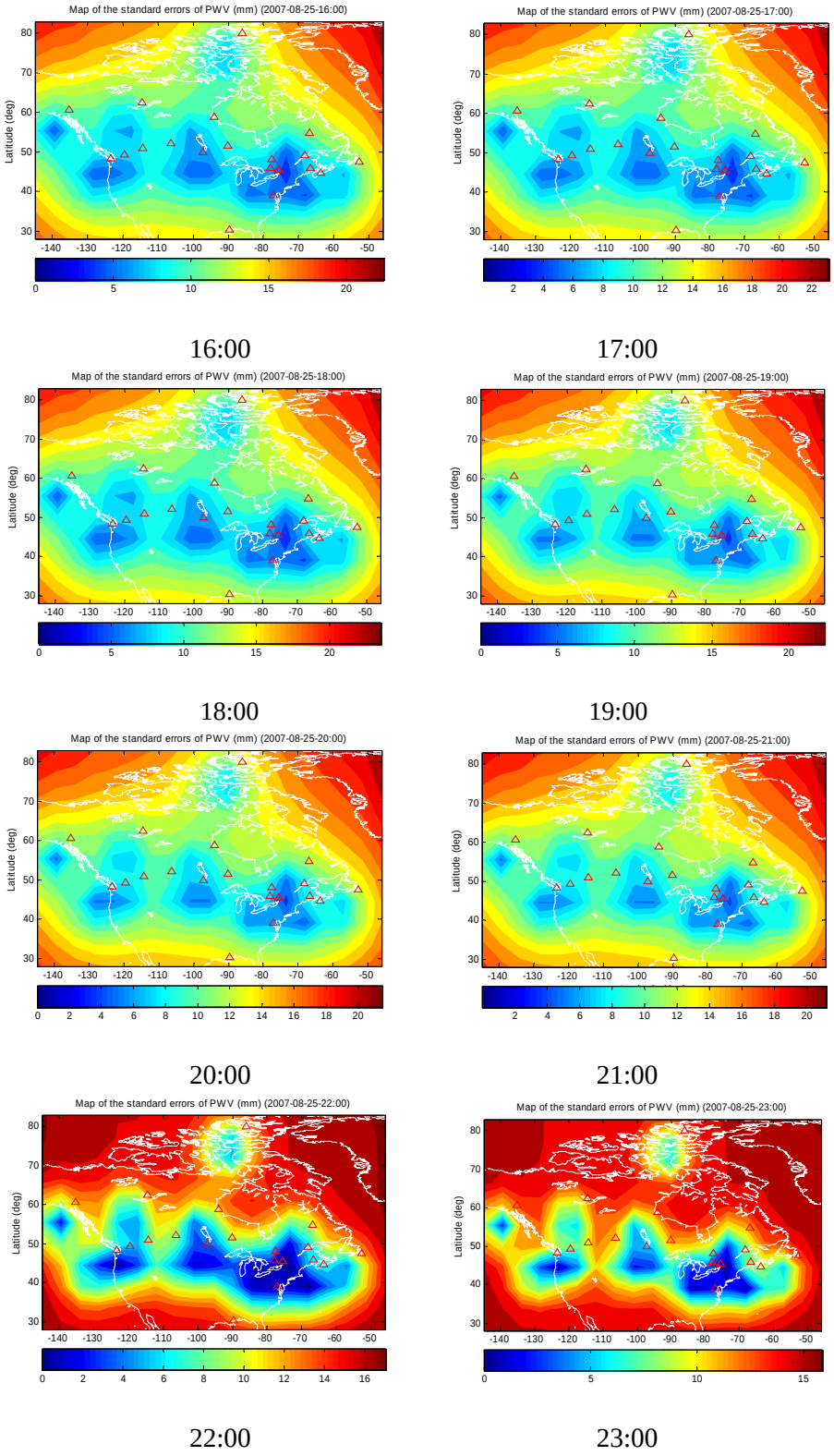

Figure 6-17 Hourly kriging standard error maps (Horizontal axis = Longitude) (3)

6.4 Summary

The geostatistical technique of kriging is a practical tool to analyze and predict values of a variable distributed in space or in time, which has been implemented in a Matlab program in this study to explore the PWV spatial structure, estimate PWV semivariogram and produce interpolated PWV maps.

The Matlab program consists of following steps (functions):

(1) Calculate experimental semivariogram,

(2) Estimate semivariogram model (model fitting), and

(3) Estimate surface map of PWV by ordinary kriging.

In step *one*, the factors to be considered are lag distance (5°), lag tolerance (5°) and maximum lag distance (50°) and the reliability of the calculated experimental semivariogram affects the accuracy of kriging interpolation. In step *two*, three different semivariogram models are fitted by nonlinear weighted least-squares and the best fitted model is determined by cross-validation process. In step *three*, ordinary kriging interpolating process is hourly performed to produce near real-time maps of PWV and the associated kriging standard error maps.

Both PWV maps and associated kriging standard error maps are created using limited sample datasets, which is valuable information to broad applications.

The accuracy of the estimated PWV values does not depend directly on the observation values but on the semivariogram and the configuration of the sample points (IHF, 2008). The current Canada GPS network has a low number of real-time GPS stations and its configuration is not balanced in Canada domain. Improving its configuration by increasing the number of GPS stations and properly deploying them within the network will increase the accuracy of semivariogram model and accordingly increase the accuracy of the estimated PWV maps.

Chapter Seven: Principal Component Analysis of GPS Water Vapor Dataset

The datasets from the real-time GPS PPP-inferred water vapor system consists of variables of observations/measurements, satellite geometry factors and meteorological parameters. There often exist special correlations between these variables. It is needed to discover the hidden relationships among them and extract meaningful variables for further effective data analysis. This thesis dealt with this issue in two steps: (i) *Principal component analysis* (PCA) was carried out to simplify the description of the GPS water vapor dataset; (ii) *Correlation analysis* was further performed to explain and summarize the inter-correlations between the four types of variables of the GPS water vapor dataset.

In this chapter, firstly, a brief introduction to the principal component analysis is presented. Then, the PCA process and its derived principal components of the near real-time GPS PPP-inferred water vapor system are explained. Next, the numerical analytic results of the between-subset (between-type) relation found between four types of variables of the system by correlation analysis are shown and discussed. At last, the summary of the analysis results are given.

7.1 Introduction of principal component analysis

Principal component analysis is mathematically an orthogonal linear transformation that transform a dataset from the original coordinate system to a new coordinate system, known as the *principal subspace*, such that the greatest variance of the projected data is reflected on the first coordinate (called the *first principal component*, or the *first domain*), the second greatest variance on the second coordinate (called the *second principal component*, or the *second domain*), and so on. PCA can be applied to dimension reduction in a dataset by keeping the lower-order principal components which contain the "most important" aspects of the dataset and ignoring the succeeding higher-order principal components (Bishop, 2006).

7.1.1 Maximum variance formulation of PCA

PCA can be defined by either *maximum variance formulation* or *minimum-error formulation*; both formulations derive the same algorithm of PCA (Bishop, 2006). In this section, the maximum variance formulation is shown below based on the book: *Pattern Recognition and Machine Learning* by Christopher M. Bishop.

Let $\{\vec{x}_n\}$ be a data set of vector samples in *D*-dimensional space, where $n = 1, \ldots, N$. The primary goal of PCA is to project the data onto a *M*-dimension space ($M < D$) while maximizing the variance of the projected data, i.e. the data is most 'spread out' in the directions of new *M*-dimensional space.

When $M = 1$, that is the projection onto a *one*-dimensional space. The direction of this space is defined using a *D*-dimensional unit vector $\vec{u}_1$ ($\vec{u}_1^T \vec{u}_1 = 1$) (see Figure 7.1). Each data point $\vec{x}_n$ is projected onto a scalar value $\vec{u}_1^T \vec{x}_n$ and the mean of the whole projected data is $\vec{u}_1^T \bar{\vec{x}}$ where $\bar{\vec{x}}$ is the sample set mean given by

$$\bar{\vec{x}} = \frac{1}{N} \sum_{n=1}^{N} \vec{x}_n \tag{7.1}$$

and the variance of projected data is given by

$$\frac{1}{N} \sum_{n=1}^{N} \left\{ \vec{u}_1^T \vec{x}_n - \vec{u}_1^T \bar{\vec{x}} \right\}^2 = \vec{u}_1^T S \vec{u}_1 \tag{7.2}$$

where *S* is the data covariance matrix defined by

$$\frac{1}{N} \sum_{n=1}^{N} \left(\vec{x}_n - \bar{\vec{x}} \right) \left(\vec{x}_n - \bar{\vec{x}} \right)^T . \tag{7.3}$$

To maximize the projected variance $\vec{u}_1^T S \vec{u}_1$ with respect to $\vec{u}_1$ under the constraint $\vec{u}_1^T \vec{u}_1 = 1$, a Lagrange multiplier λ_1 is introduced and makes an unconstrained maximization:

$$max: \ \vec{u}_1^T S \vec{u} + \lambda_1 \left(1 - \vec{u}_1^T \vec{u}_1 \right).$$

Making the first derivative with respect to $\vec{u}_1$ and setting it equal to zero:

$$\frac{\partial}{\partial \vec{u}_1} \left(\vec{u}_1^T S \vec{u} + \lambda_1 \left(1 - \vec{u}_1^T \vec{u}_1 \right) \right) = S \vec{u}_1 - \lambda_1 \vec{u}_1 = 0$$

then:

$$S\vec{u}_1 = \lambda_1 \vec{u}_1,$$

or

$$\vec{u}_1^T S\vec{u}_1 = \lambda_1$$

which means that (i) $\vec{u}_1$ must be an eigenvector of S, and (ii) the variance of the projected data will be a maximum when $\vec{u}_1$ is set to be equal to the eigenvector with the largest eigenvalue λ_1. This eigenvector is called as the *first* principal component.

Following the above process, an additional principal component can be defined by choosing each new direction which maximizes the projected variance among all possible directions orthogonal to those considered. In the general case of an *M*-dimensional space, the optimal linear projection for which the variance of the projected data is maximized is now defined by the M eigenvectors $\vec{u}_1$, $\vec{u}_2$, …, $\vec{u}_M$ of the data covariance matrix S corresponding to the M largest eigenvalues λ_1, λ_2, …, λ_M.

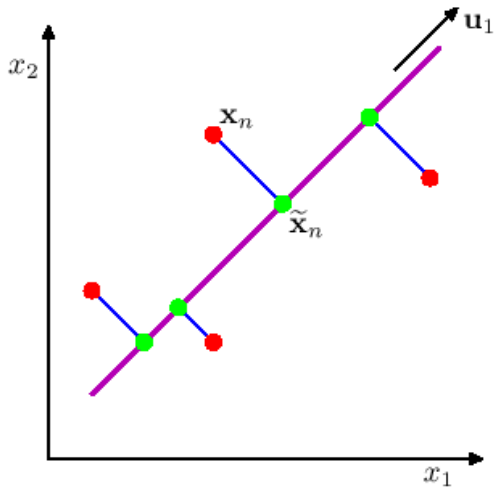

Figure 7.1 Schematic diagram of principal component analysis (PCA)
(Bishop, 2006)

7.2 Principal component analysis of GPS water vapor dataset

This section intends to simplify the description of the GPS water vapor dataset using principle component analysis.

7.2.1 Data preparation

7.2.1.1 Data categorizing

The dataset used for this analysis was from Chapter 5, which is a nine-station two-day post-processed GPS water vapor dataset from October 18 ~ 19, 2007. There are totally *seventeen* variables in this dataset. According to their attributes, the *seventeen* variables of the dataset are sorted into four categories: *Measurement*, *Satellite geometric factor*, *Meteorological parameter* and *Position error* (see Table 7.1) (since the actual GPS receiver clock time were not provided at these stations, *GPS receiver clock error* variable was not included in this analysis).

Table 7.1 Original GPS water vapor dataset

Category of Variables	Description
Measurement	ZTD (X_1)
	ZDD (X_2)
	ZWD (X_3)
	PWV (X_4)
	PWV bias (X_5)
Satellite Geometry Factor	# SAT (X_6)
	GDOP (X_7)
	PDOP (X_8)
	HDOP (X_9)
	VDOP (X_{10})
	TDOP (X_{11})
Meteorological Parameter	Pressure (X_{12})
	Temperature (X_{13})
	Relative Humidity (X_{14})
Position Error	East Error (X_{15})
	North Error (X_{16})
	Up Error (X_{17})

7.2.1.2 Outlier removing

Considering the impact of the outliers to PCA (Krzanowski 1988), thirteen outliers were detected using the scatterplots of dilution of precision (DOP) and removed.

7.2.1.3 Data standardizing

Since the seventeen original variables were measured in various different units and had significantly different variability, they need to be standardized prior to principal component analysis (Krzanowski, 1988). Standardization is achieved by considering each variable separately, subtracting the variable sample mean from each observation and then dividing the result by that variable's sample standard deviation such that each individual variable had *zero* mean and *unit* variance. The data standardization was carried out *station by station* considering the topographic difference of each individual station. Since the original dataset was standardized, the following PCA analysis is equivalent to analyzing the *correlation matrix* instead of the *covariance matrix*. When the principal components are derived from the correlation matrix, the interpretation becomes easier in two ways (Afifi et al., 2004):

(i) The total variance is simply the number of variables *P*, and the proportion explained by each principal component is the corresponding eigenvalue divided by *P*.

(ii) The correlation between the *i*th principal component C_i and the *j*th variable x_j is

$$r_{ij} = a_{ij} \cdot \left(\mathrm{Var}\, C_i\right)^{\frac{1}{2}} \tag{7.4}$$

where a_{ij} is the coefficient of the *j*th variable x_j for *i*th principal component C_i; ' $\mathrm{Var}\, C_i$ ' means 'the variance (eigenvalue) of component C_i'.

Therefore for a given component C_i the a_{ij} can be compared to qualify the relative degree of dependence of C_i on each of the standardized variables.

At last, the standardized datasets of the nine stations were merged into one data matrix with size (4980 × 17), where the seventeen data items of *each epoch* are aligned in a row.

7.2.2 Analytic results

Matlab PCA function is utilized to execute the principal component analysis on the standardized data matrix (Section 7.2.1). The output results are shown in Figure 7.2. In Figure 7.2, (i) *COEFF* is a 17-by-17 PCA coefficient matrix where each column represents a new component/domain of the GPS water vapor dataset and each row represents each original variable's coefficient (i.e. loading or contribution from an original variable) to each component/domain and the columns of COEFF are in order of decreasing component variance; (ii) *latent* is a 17-by-1 eigenvalue vector where each row element represents the eigenvalue (i.e., variance) of the corresponding component listed in *COEFF*. The total variance of the seventeen components is equivalent to 17, i.e. the number of the components.

```
COEFF =

  Columns 1 through 9

    0.0496   -0.4449    0.3364   -0.0864    0.0657   -0.0633   -0.0464    0.1270   -0.0333
   -0.0193    0.2468    0.5416   -0.2887    0.0960    0.1547   -0.0728    0.0543    0.0529
    0.0381   -0.5238    0.1756    0.0346    0.0158    0.0042   -0.0272    0.0959   -0.0362
    0.0398   -0.5252    0.1682    0.0230    0.0182   -0.0016   -0.0354    0.0954   -0.0384
   -0.0383    0.0165    0.2505    0.2766   -0.4475   -0.2395   -0.5790   -0.5025    0.1068
   -0.3183    0.0007    0.0487    0.1510    0.2236    0.1727   -0.1147   -0.2142   -0.7092
    0.4311    0.0497    0.0272    0.0833    0.0563    0.0478   -0.0282   -0.0429   -0.1416
    0.4309    0.0529    0.0251    0.0781    0.0567    0.0333   -0.0240   -0.0394   -0.1244
    0.3830    0.0586    0.0308    0.0970   -0.0135   -0.0676    0.0295    0.0529    0.3345
    0.4127    0.0435    0.0201    0.0603    0.0786    0.0709   -0.0419   -0.0782   -0.3170
    0.4239    0.0400    0.0282    0.0867    0.0489    0.0797   -0.0296   -0.0487   -0.1692
   -0.0194    0.2478    0.5420   -0.2873    0.0957    0.1516   -0.0726    0.0554    0.0521
    0.1032   -0.2609   -0.2021   -0.4468    0.1355   -0.1990   -0.2393   -0.1351    0.0454
   -0.0480   -0.1675    0.2238    0.4185   -0.0413    0.3765    0.4764   -0.3117    0.2353
   -0.0366    0.1343    0.2528    0.3366   -0.1439   -0.5950    0.1724    0.4724   -0.2263
    0.0765   -0.0250    0.0917   -0.4266   -0.3511   -0.3123    0.5571   -0.4275   -0.2333
    0.0511   -0.0480   -0.0933   -0.1482   -0.7398    0.4579   -0.0881    0.3539   -0.1914

  Columns 10 through 17

   -0.0781   -0.0347    0.8022   -0.0161   -0.0020   -0.0017    0.0010    0.0128
    0.0622   -0.0054   -0.1196    0.0016    0.0012    0.0201   -0.7065   -0.0010
   -0.1595    0.0423   -0.3839    0.0206    0.0037    0.0026   -0.0012   -0.7111
   -0.1460    0.0387   -0.4056    0.0173    0.0009   -0.0005   -0.0003    0.7028
   -0.0086    0.0479    0.0058   -0.0008   -0.0006   -0.0012   -0.0005    0.0003
   -0.0047   -0.4801   -0.0115    0.0326    0.0043   -0.0016    0.0003   -0.0009
    0.0183    0.0229    0.0025    0.0205    0.3214    0.8190    0.0244    0.0024
    0.0191    0.0163    0.0078    0.3288    0.6308   -0.5253   -0.0138    0.0009
   -0.1923   -0.7654   -0.0403    0.1445   -0.2712   -0.0208   -0.0015    0.0001
    0.1043    0.3423    0.0238    0.3936   -0.6453   -0.0650   -0.0040   -0.0007
   -0.0026    0.0225   -0.0221   -0.8439   -0.0935   -0.2187   -0.0056   -0.0027
    0.0589   -0.0043   -0.1216    0.0032   -0.0026   -0.0205    0.7071   -0.0021
    0.7081   -0.1948   -0.0715   -0.0222   -0.0003   -0.0010    0.0021   -0.0159
    0.4692   -0.0252    0.0256    0.0037   -0.0025   -0.0020    0.0018    0.0050
    0.3420   -0.0460   -0.0715   -0.0216    0.0000   -0.0008   -0.0016   -0.0017
   -0.1782   -0.0470   -0.0281   -0.0030    0.0066    0.0032   -0.0005    0.0000
    0.1444   -0.1248    0.0302    0.0219    0.0014   -0.0002    0.0011   -0.0006

latent =

    5.1459
    3.2466
    2.1112
    1.6092
    1.0907
    0.9818
    0.8455
    0.6733
    0.5087
    0.3688
    0.2322
    0.1055
    0.0402
    0.0075
    0.0038
    0.0016
    0.0002
```

Figure 7.2 Output of 17 variable PCA analysis

(*COEFF* is a 17-by-17 matrix, each column containing coefficients for one principal component and the columns of COEFF are in order of decreasing component variance. *latent* is a 17-by-1 vector containing the eigenvalues of the covariance matrix of the GPS water vapor dataset.)

7.2.2.1 Validation of principal components

Number of components retained

As mentioned earlier, one of the objectives of PCA is dimension reduction. The purpose of the dimension reduction is to make analysis and interpretation easier, while at the same

time retaining most of the information (variation) contained in the data. Since the principal components are arranged in decreasing order of variance, the leading principal components would be selected as representatives of the original set of variables.

There are various rules proposed to estimate the number of components to retain in a principal component analysis, but none of them appear to work well in all circumstances (Afifi et al., 2004). *One* rule is to keep a sufficient number of principal components to explain a certain percentage of the total variance. One common cutoff point for this rule is 80%. *Another* rule is to discard principal components which have a variance less than 70/*P* (*P*: the number of variables) percent of the total variance. In this study, the principal component which has a variance of *less than 5%* of the total variance is *not* retained.

Table 7.2 summarizes the first *seven principal components* from Figure 7.2, where a new domain (a column) is retained when its variance/eigenvalue is greater than 5% of the total variance. The principal component 7 is included, although it has a variance close to 5% (i.e., 4.97%). These seven components explain 88.59% of the total variance (i.e., the number of the variables = 17). The values (coefficients/loadings) contained in Table 7.2 illustrate the strength of the relationship between each variable and the new components/domains.

Table 7.2 PCA loading for original GPS water vapor dataset

Original Variable	Principal Component (Domain)						
	1 (Size of DOP)	**2** (Size of Total Delay)	**3** (Vol of ZDD)	**4** (?)	**5** (Vol of Up Posi Err)	**6** (East-Up Posi Err Contr)	**7** (PWV Bias-Nor Posi Err Contr)
X1	0.0496	**-0.4449**	0.3364	-0.0864	0.0657	-0.0633	-0.0464
X2	-0.0193	0.2468	**0.5416**	-0.2887	0.0960	0.1547	-0.0728
X3	0.0381	**-0.5238**	0.1756	0.0346	0.0158	0.0042	-0.0272
X4	0.0398	**-0.5252**	0.1682	0.0230	0.0182	-0.0016	-0.0354
X5	-0.0383	0.0165	0.2505	0.2766	-0.4475	-0.2395	**-0.5790**
X6	**-0.3183**	0.0007	0.0487	0.1510	0.2236	0.1727	-0.1147
X7	**0.4311**	0.0497	0.0272	0.0833	0.0563	0.0478	-0.0282
X8	**0.4309**	0.0529	0.0251	0.0781	0.0567	0.0333	-0.0240
X9	**0.3830**	0.0586	0.0308	0.0970	-0.0135	-0.0676	0.0295
X10	**0.4127**	0.0435	0.0201	0.0603	0.0786	0.0709	-0.0419
X11	**0.4239**	0.0400	0.0282	0.0867	0.0489	0.0797	-0.0296
X12	-0.0194	0.2478	**0.5420**	-0.2873	0.0957	0.1516	-0.0726
X13	0.1032	-0.2609	-0.2021	**-0.4468**	0.1355	-0.1990	-0.2393
X14	-0.0480	-0.1675	0.2238	**0.4185**	-0.0413	0.3765	0.4764
X15	0.0366	0.1343	0.2528	0.3366	-0.1439	**-0.5950**	0.1724
X16	0.0765	-0.0250	0.0917	**-0.4266**	-0.3511	-0.3123	**0.5571**
X17	0.0511	-0.0480	-0.0933	-0.1482	**-0.7398**	**0.4579**	-0.0881
Eigenvalue or Var *Ci*	5.1459	3.2466	2.1112	1.6092	1.0907	0.9818	0.8455
Variance explained	30.27%	19.10%	12.42%	9.47%	6.42%	5.78%	4.97%
Cumulative proportion	30.27%	49.37%	61.79%	71.25%	77.67%	83.44%	**88.42%**
$0.5/(\mathrm{Var}\ C_i)^{\frac{1}{2}}$	0.2204	0.2775	0.3441	0.3942	0.4788	0.5046	0.5438

Interpretation of principal component

When the principal components are selected, they are interpreted in the context of the variables with high coefficients. For each principal component the variables with a correlation greater than 0.5 with that component are regarded as significantly contributing variables (Afifi et al., 2004). In this study, this value (0.5) is taken as a cutoff point. Since the correlation $r_{ij} = a_{ij} \cdot (\mathrm{Var}\, C_i)^{\frac{1}{2}}$ (Equation 7.4), a coefficient a_{ij} in Table 7.2 is highlighted by bold typeface if it exceeds $0.5/(\mathrm{Var}\, C_i)^{\frac{1}{2}}$ (Table 7.2).

As Table 7.2 shows, *six* Satellite Geometry Factor variables are highly correlated (greater than 0.5) with the first principal component. Thus, the first component C_1 can be approximately represented as $C_1 = 0.4(X_7 + X_8 + X_9 + X_{10} + X_{11}) - 0.3X_6$. The most extreme positive value on this component will be taken by a GPS satellite configuration that has large values for X_7 through X_{11} (i.e., all large DOPs) but small values for X_6 (i.e., small number of available satellites). At the other extreme, a large negative value for C_1 will be taken by a GPS satellite configuration that has a large number (X_6) of available satellites but small values for all DOPs (i.e., X_7 through X_{11}). Hence C_1 is identified as a measure of 'Satellite availability' or *Size of DOP*.

Component C_2 shows a high correlation with X_1(ZTD), X_3 (ZWD) and X_4 (PWV) and it is approximately of the form $C_2 = -0.5(X_1 + X_3 + X_4)$. As it is known, ZWD contributes to ZTD and PWV contributes to ZWD. The previous combination indicates that C_2 measures the *Size of Total Delay*.

Component C_3 is defined by X_2(ZDD) and X_{12} (Pressure) and it is approximately of the form $C_3 = -0.5(X_2 + X_{12})$. Since X_{12} contributes directly to X_2 (see Equation 2.19), C_3 is identified as a measure of ZDD. Thus, C_3 will be interpreted as the *Volume of ZDD*.

Component C_4 is defined by a cluster of X_{13}(Temperature) , X_{14} (Humidity) and X_{16} (North Position Error) and it is approximately of the form $C_4 = 0.4(X_{14} - X_{13}) - 0.4X_{16}$. The first term shows the contrast between *Temperature* and *Humidity*; but the second term represents the negative contribution of *North Position Error*. In this context, component C_4 does not have a clear-up physical interpretation. The question mark is put under component C_4 in Table 7.2.

Component C_5 is uniquely defined by a single variable X_{17} (Up Position Error). C_5, therefore, is interpreted as a measure of the position error in up direction and will be called *Volume of Up (Position) Error*.

Component C_6 is defined by two position error metrics, X_{15} (East Position Error) and X_{17} (Up Position Error), which can be proximately represented as $C_6 = 0.5(X_{17}) - 0.6(X_{15})$. This form indicates the negative association between two position error metrics. C_6 will be called the *East-Up (Position) Error Contrast.*

Component C_7 is defined by two different kind of error metrics, X_5 (PWV bias) and X_{16} (North (Position) Error) and is approximately given by $C_7 = 0.6(X_{16} - X_5)$. The form represents the negative association between *PWV Bias* and *North (Position) Error*. Like Component C_6, C_7 will be called *PWV Bias-North (Position) Error Contrast.*

7.2.2.2 Remodelling of principal components

There are some problems with the component structure above (Table 7.2):

(i) *Component duplication* exits between C_2 (*Size of Total Delays*) and C_3 (*Volume of ZDD*). In fact, C_3 is included in C_2 because *ZTD* (X_1) is computed in formula: $ZTD = ZDD + ZWD$ and $\mathrm{ZDD} \approx 0.9 \times \mathrm{ZTD}$.

(ii) Some correlated original variables cause *noises* in the component structure, which blurs some principal component identifications. One noise component is ZTD (X_1) since it is highly correlated with ZDD. Another noise component is PWV (X_4) since it is highly correlated with ZWD (i.e., $PWV = ZWV / Q$, where Q is conversion factor: Q = 5.9 ~ 6.5).

Hence *ZDD* (X_1) and *PWV* (X_4) are removed from the original GPS water vapor dataset. Analyzing the *reduced* fifteen-variable GPS water vapor dataset again by principal component analysis, the new, concise component structure is derived and shown in Table 7.3 (The whole PCA results are shown in Figure 7.3), where the values of the contributing variables are highlighted by bold typeface.

```
COEFF =

  Columns 1 through 9

   -0.0149   -0.5718   -0.2510   -0.2027    0.1882   -0.0941    0.0891    0.1261   -0.0223
    0.0164    0.2920    0.1419   -0.6148    0.2576    0.1585    0.1415    0.3803    0.1461
   -0.0392   -0.1770    0.3101   -0.2737   -0.4127    0.1779    0.6559   -0.3747   -0.1425
   -0.3186   -0.0450    0.1508    0.0686    0.2394   -0.1366    0.1295   -0.2935    0.6768
    0.4327   -0.0435    0.0816    0.0236    0.0595   -0.0395    0.0306   -0.0566    0.1367
    0.4327   -0.0447    0.0757    0.0295    0.0551   -0.0262    0.0264   -0.0522    0.1196
    0.3849   -0.0550    0.0936    0.0329   -0.0384    0.0559   -0.0352    0.0666   -0.3429
    0.4142   -0.0343    0.0589    0.0218    0.0881   -0.0559    0.0484   -0.1018    0.3137
    0.4252   -0.0366    0.0867    0.0077    0.0633   -0.0690    0.0313   -0.0661    0.1626
   -0.0149   -0.5728   -0.2498   -0.2011    0.1867   -0.0916    0.0887    0.1265   -0.0218
    0.0947    0.3508   -0.4218   -0.1467    0.1700    0.2691    0.3343    0.1122    0.0491
   -0.0552   -0.0019    0.4832   -0.4633    0.2467   -0.1970   -0.3795   -0.1720   -0.2092
   -0.0337   -0.2850    0.3406    0.0799   -0.2963    0.5244   -0.2002    0.4784    0.3169
    0.0749   -0.0320   -0.3933   -0.3691   -0.2456    0.3858   -0.4623   -0.4819    0.1611
    0.0503    0.1075   -0.1461   -0.2810   -0.6149   -0.5991   -0.0374    0.2618    0.2266

  Columns 10 through 15

    0.0256   -0.0109   -0.0006    0.0009   -0.0199    0.7064
   -0.4849    0.0562    0.0234    0.0028   -0.0006    0.0006
    0.0288    0.0473   -0.0008   -0.0006    0.0012    0.0005
   -0.0406   -0.4789    0.0325    0.0043    0.0017   -0.0003
    0.0132    0.0227    0.0206    0.3215   -0.8189   -0.0245
    0.0168    0.0160    0.3288    0.6307    0.5254    0.0138
   -0.1810   -0.7640    0.1439   -0.2713    0.0209    0.0015
    0.0951    0.3414    0.3938   -0.6453    0.0650    0.0040
   -0.0137    0.0229   -0.8441   -0.0935    0.2186    0.0056
    0.0222   -0.0098    0.0009   -0.0029    0.0208   -0.7072
    0.6305   -0.2057   -0.0238   -0.0005    0.0012   -0.0022
    0.4805   -0.0311    0.0035   -0.0025    0.0020   -0.0018
    0.2447   -0.0516   -0.0229   -0.0001    0.0010    0.0015
   -0.1381   -0.0469   -0.0036    0.0066   -0.0032    0.0005
    0.1069   -0.1241    0.0224    0.0014    0.0002   -0.0011


latent =

    5.1348
    2.3885
    1.6091
    1.2458
    1.0624
    0.9669
    0.8344
    0.6124
    0.5033
    0.3336
    0.2317
    0.0402
    0.0075
    0.0038
    0.0016
```

Figure 7.3 Output of fifteen-variable PCA analysis

(COEFF is a 15-by-15 matrix, each column containing coefficients for one principal component and the columns of COEFF are in order of decreasing component variance. latent is a 15-by-1 vector containing the eigenvalues of the covariance matrix of the GPS water vapor dataset.)

Table 7.3 PCA loading of fifteen-variable GPS water vapour dataset

Original Variable	Principal Component (Domain)						
	1 (Size of DOP)	**2** (Vol of ZDD)	**3** (Moisture Content)	**4** (Vol of ZWD)	**5** (Vol of Up Posi Err)	**6** (East-Up Posi Err Contr)	**7** (Vol of PWV Bias)
X2	-0.0149	**-0.5718**	-0.2510	-0.2027	0.1882	-0.0941	0.0891
X3	0.0164	0.2920	0.1419	**-0.6148**	0.2576	0.1585	0.1415
X5	-0.0392	-0.1770	0.3101	-0.2737	-0.4127	0.1779	**0.6559**
X6	**-0.3186**	-0.0450	0.1508	0.0686	0.2394	-0.1366	0.1295
X7	**0.4327**	-0.0435	0.0816	0.0236	0.0595	-0.0395	0.0306
X8	**0.4327**	-0.0447	0.0757	0.0295	0.0551	-0.0262	0.0264
X9	**0.3849**	-0.0550	0.0936	0.0329	-0.0384	0.0559	-0.0352
X10	**0.4142**	-0.0343	0.0589	0.0218	0.0881	-0.0559	0.0484
X11	**0.4252**	-0.0366	0.0867	0.0077	0.0633	-0.0690	0.0313
X12	-0.0149	**-0.5728**	-0.2498	-0.2011	0.1867	-0.0916	0.0887
X13	0.0947	0.3508	**-0.4218**	-0.1467	0.1700	0.2691	0.3343
X14	-0.0552	-0.0019	**0.4832**	**-0.4633**	0.2467	-0.1970	-0.3795
X15	-0.0337	-0.2850	0.3406	0.0799	-0.2963	**0.5244**	-0.2002
X16	0.0749	-0.0320	-0.3933	-0.3691	-0.2456	0.3858	-0.4623
X17	0.0503	0.1075	-0.1461	-0.2810	**-0.6149**	**-0.5991**	-0.0374
Eigenvalue or Var *Ci*	5.1348	2.3885	1.6091	1.2458	1.0624	0.9669	0.8344
Variance explained	34.23%	15.92%	10.73%	8.31%	7.08%	6.45%	5.56%
Cumulative proportion	34.23%	50.16%	60.88%	69.19%	76.27%	82.72%	**88.30%**
$0.5/(\mathrm{Var}\ C_i)^{\frac{1}{2}}$	0.2207	0.3235	0.3941	0.4480	0.4851	0.5085	0.5474

The new component structure (Table 7.3) has the following changes.

(i) Two 'noisy' variables X_1 (*ZTD*) and X_4 (*PWV*) were removed from the component structure.

(ii) Component *Size of Delays* is absent, i.e. no more component duplication.

(iii) Components C_1, C_5 and C_6 remain in their definitions and their positions.

(iv) Component *Size of ZDD* remains in its definition, but it is moved up the position Component C_2 with respect to the variance it explains.

(v) In the case of Component C_3, which is equivalent to the Component C_4 of the previous component structure (Table 7.2), variable X_{16} (-0.3933) is no longer highly correlated with C_3. Thus C_3 is straight defined by the *two* meteorological variables X_{13} (Temperature) and X_{14} (Relative Humidity) and is proximately of the form $C_3 = 0.4(X_{14} - X_{13})$. This *contrast form* expresses the Temperature-Relative Humidity negative correlation, which represents the state of water vapor in the troposphere. Component C_3 is, therefore, identified as a measurement of Moisture Content.

(vi) Component C_4 is a new domain and it is defined by variables X_3 (ZWD) and X_{14} (Relative Humidity). Since X_{14} contributes to X_3, C_4 is identified as the domain of Size of ZWD.

(vii) Component C_7, which was defined by both X_5 (*PWV Bias*) and X_{16} (*North Position Error*) in the previous component structure (Table 7.2), is defined by the single position measurement, X_5 (PWV Bias), which measures the PWV offset from the true value. Component C_7 is, therefore, identified as the domain of Size of PWV Bias.

(viii) Variable X_{16} does not contribute to any components; thus total number of contributing variable is 14 (i.e. without ZTD, PWV and North Position Error).

The above analysis arrives at the *seven* domain structure, which indicates that the removal of correlated variables X_1 and X_4 makes the component structure represent the net contribution of each domain more effectively and precisely. The variants *Size of ZDD* and *Size of ZWD* are mapped to Component C_2 and C_4, respectively. Components C_3 and C_7 are defined uniquely by fewer (one or two) contributing variables. The percentage of total variance (88.30%) explained by the *seven* principal component model

is almost the same as the one (88.42%) explained by the previous component model *even through* the number of variables is decreased.

The variance explained by each component in Table 7.3 also shows that *Size of DOP* is the largest variant factor (34.23%) in the GPS water vapour measurement system and its value is changing regularly, but almost a *constant* for each day. The variances for the rest of components in decreasing order are *Volume of ZDD* (15.92%), *Moisture Content* (10.73%), *Volume of ZWD* (8.31%), *Volume of Up (Position) Error* (7.08%), *East-Up (Position) Error Contrast* (6.45%) and *Volume of PWV Bias* (5.56%); these components vary with each day's atmosphere conditions.

7.3 Correlation analysis of GPS water vapor dataset

This section will present the correlation analysis of the four types of variables listed in Table 7.1. The purpose of this analysis is to explain and summarize the relationship of between-subset (i.e. type) of variables in the GPS water vapor dataset using scatter plot and linear regression techniques. *Seven* correlations are to be investigated, which are shown in Figure 7.4. The dataset for analyzing is still the same one described in Section 7.2.1.

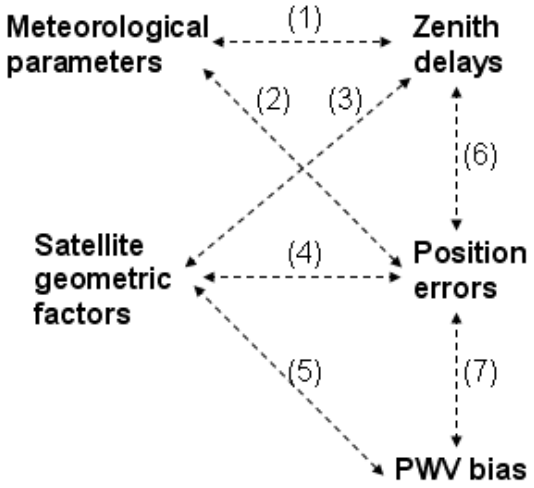

Figure 7.4 Seven variable correlations of the system

7.3.1 Correlation between zenith delays and meteorological parameters

This between-subset relation represents the influence of meteorological variables over the GPS signal delays. Table 7.4 gives the correlation coefficients between these two types and their significant correlation tests. Figure 7.5 shows the scatter plots between them and corresponding regression lines, where each cluster represents a site sample data distribution pattern.

Table 7.4 Correlation Coefficients of zenith delays and MET data

Correlation coefficient (r)				**Correlation test** $(N = 4980, \alpha = 0.01)$					
Zenith Delay	**Meteorological parameter**			*PR*		*TD*		*RH*	
	PR	*TD*	*RH*	Sample value	Popul-ation value	Sample value	Popul-ation value	Sample value	Popul-ation value
ZTD	0.9578	0.6652	0.2560	235.105	2.4121	62.857	2.4121	18.685	2.4121
ZDD	1.0000	0.4922	0.1705	∞	2.4121	39.894	2.4121	12.208	2.4121
ZWD	0.4558	0.8310	0.3679	36.130	2.4121	105.4	2.4121	27.915	2.4121

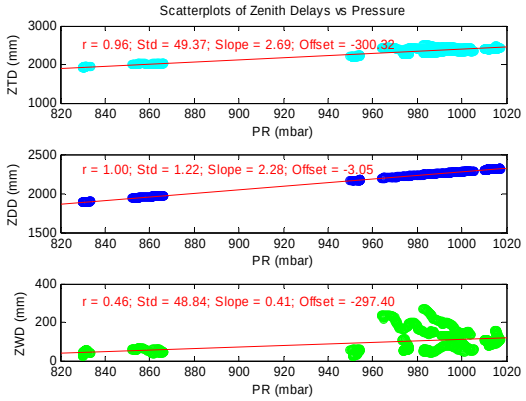

(a) *Zenith delays vs pressure*

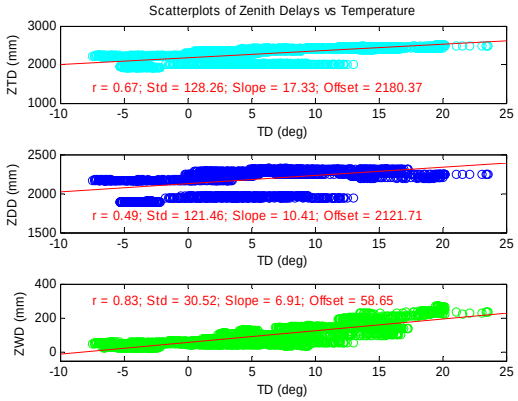

(b) *Zenith delays vs temperature*

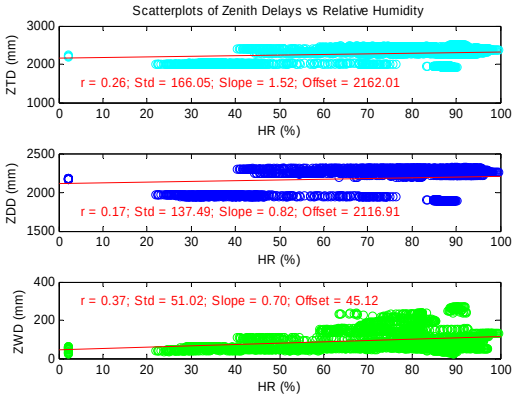

(c) *Zenith delays vs relative humidity*

Figure 7.5 Scatterplots between zenith delays and meteorological parameters

The analytical results show that:

(1) All delays *positively* associate with all meteorological variables;

(2) Scatter plots show that: (i) most associations (except the association of ZDD versus pressure) present the forms of *function of multi variables* where each individual function value represent each sample site association pattern; (ii) most associations (except the association of ZWD versus pressure) are approximately *linear* and indicate the *additivity* of effect among different site values, *i.e.*, different site data clusters parallel with one another, which means that these associations can better summarized by multiple regression (Ott, 1988 (Ch 12)); (iii) the association between ZWD and pressure at each site is *nonlinear*.(see Figure 7.5 (a));

(3) The correlation coefficient between *ZTD* and *pressure* has a high value (r = 0.96), which means *pressure* is the most informative variable for *ZTD*, that is, if a value of *pressure* is given then the corresponding *ZTD* value can be estimated quite accurately (Afifi et al. 2004); the regression coefficient (slope = 2.69) indicates that 1-mbr-increment of pressure leads to ~2.69-mm-increment of ZTD (see Figure 7.5 (a));

(4) The association of *ZDD* versus *pressure* presents the form of one-valued function (r = 1) (Figure 7.5 (a)), i.e., pressure explains 100% of ZDD' variance, which is the *only* one-valued function between these two types and the regression coefficient (2.28) indicates that 1-mbr-increment of pressure leads to ~2.28-mm-increment of ZDD (Dodson et al. (1996) found that a pressure error of 1 mbar pressure error translates to a 2.3 mm ZDD error);

(5) *Temperature* has a very strong association with *ZWD* (r = 0.83), which, as a whole, would cause an increment of ZWD by ~6.91 mm for each unit temperature (Figure 7.5 (b)) (Dodson et al. (1996) found that a *2°C* error in temperature can result in a 12 mm ZWD error);

(6) *Relative humidity* contributes to *ZWD* (0.3676) much less than the *temperature* does to *ZWD* (0.8312); and

(7) Both *humidity* and *temperature* had bigger varying ranges than *pressure* did (this conforms the PCA results).

7.3.2 Correlation between position errors and meteorological parameters

This correlation analysis provides us information how sensitive the system solutions are to the variation of meteorological environment. Table 7.5 gives the correlation coefficients between these two types of variables and their significant correlation test results. Figure 7.6 shows the scatter plots of between these two types of variables. The analytical results show that:

(1) Associations exist between most relations of these two types except the one of north position error versus relative humidity;

(2) Associations between *east position error* and *meteorological variables* (at each site) are approximately linear, while others are nonlinear;

(3) The affection of meteorological variables are mainly reflected on the *east* and *up position errors*;

(4) *Pressure* and *temperature* mainly contributes *negatively* to *east position error* (r = -0.6932 and r = -0.3451, as a whole); and

(5) *Relative humidity* mainly contributes *positively* to *up position error* (r = 0.4709, as a whole).

Table 7.5 Correlation coefficients of position errors and MET data

Correlation coefficient (*r*)				**Correlation test** $(N = 4980, \alpha = 0.01)$					
Position error	**Meteorological parameter**			*PR*		*TD*		*RH*	
	PR	*TD*	*RH*	Sample value	Popul-ation value	Sample value	Popul-ation value	Sample value	Popul-ation value
East	-0.6934	-0.3448	0.2380	-67.896	2.412	-25.917	-2.412	17.289	2.412
North	-0.1892	0.0802	-0.0214	-13.595	-2.412	5.677	2.412	-1.51*	-2.412
Up	-0.3339	-0.1467	0.4703	-24.993	-2.412	-10.464	-2.412	37.60	2.412

*: means that test failed, *i.e.*, no significant correlation

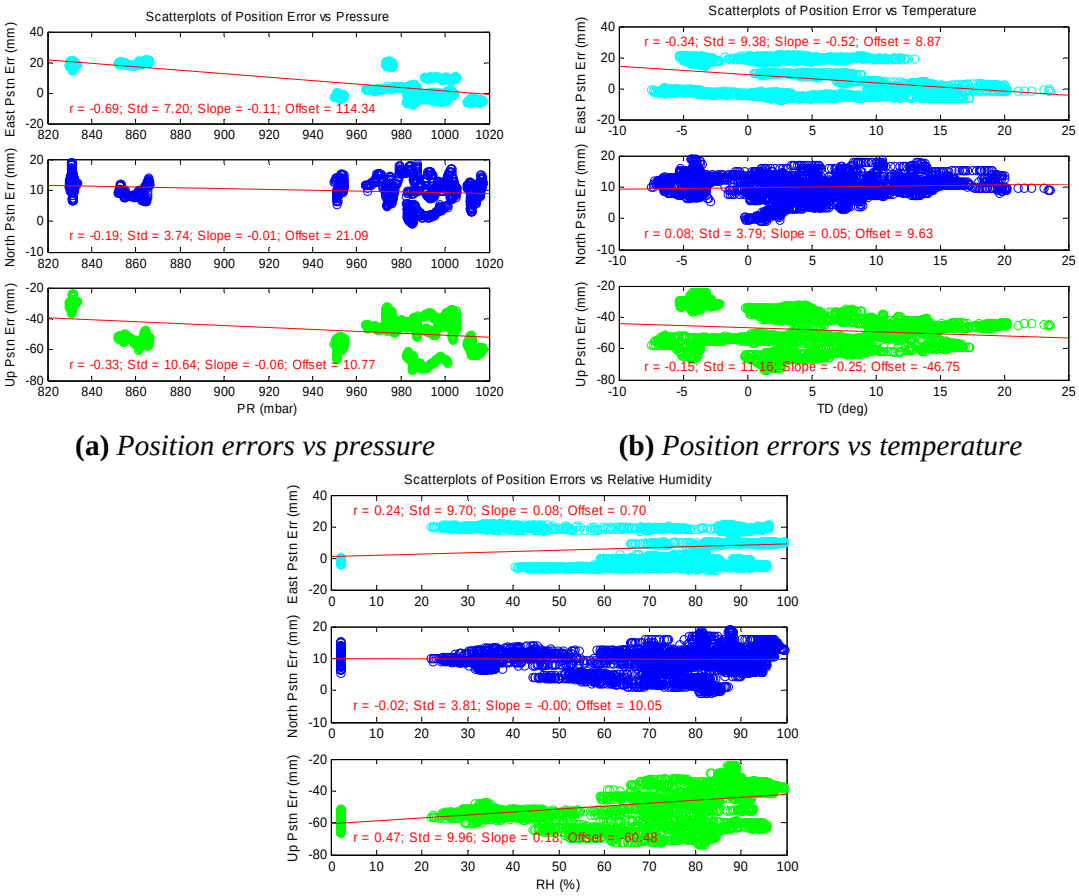

(a) *Position errors vs pressure* **(b)** *Position errors vs temperature*

(c) *Position errors vs relative humidity*

Figure 7.6 Scatter plots of position errors and MET parameters
(Each cluster represents the observation sample from one station)

7.3.3 Correlation between zenith delays and satellite geometrical factors

This correlation analysis investigates the impacts from satellite geometric factors to zenith delays. The correlation coefficients and their significant tests are given in Table 7.6. The scatter plots between them are shown in Figure 7.7. The analytical results show:

(1) That although the correlation coefficients do not show high values, the *weak* associations exist between these two types of variables;

(2) That *all* six satellite geometrical factors have bigger influences over *ZWD* than over *ZTD/ZDD*;

(3) That *all* DOPs have *positive* associations with *zenith delays*; and

(4) That *satellite number* has *negative* associations with *zenith delays*.

Table 7.6 Correlation coefficients between zenith delays and satellite geometric factors

Correlation coefficient (r)				**Correlation Test** $(N = 4980, \alpha = 0.01)$					
Satellite geometric variable	**Zenith delays**			*ZTD*		*ZDD*		*ZWD*	
	ZTD	*ZDD*	*ZWD*	Sample value	Popul-ation value	Sample value	Popul-ation value	Sample value	Popul-ation value
Satellite #	-0.0895	-0.0564	-0.1369	-6.34	-2.412	-3.986	-2.412	-9.751	-2.412
GDOP	0.0941	0.0665	0.1256	6.669	2.412	4.702	2.412	8.932	2.412
PDOP	0.0840	0.0591	0.1129	5.948	2.412	4.177	2.412	8.017	2.412
HDOP	0.0883	0.0603	0.1232	6.254	2.412	4.262	2.412	8.759	2.412
VDOP	0.0726	0.0508	0.0983	5.136	2.412	3.589	2.412	6.969	2.412
TDOP	0.1129	0.0799	0.1503	8.017	2.412	5.655	2.412	10.726	2.412

*: means that test failed, *i.e.*, no significant correlation

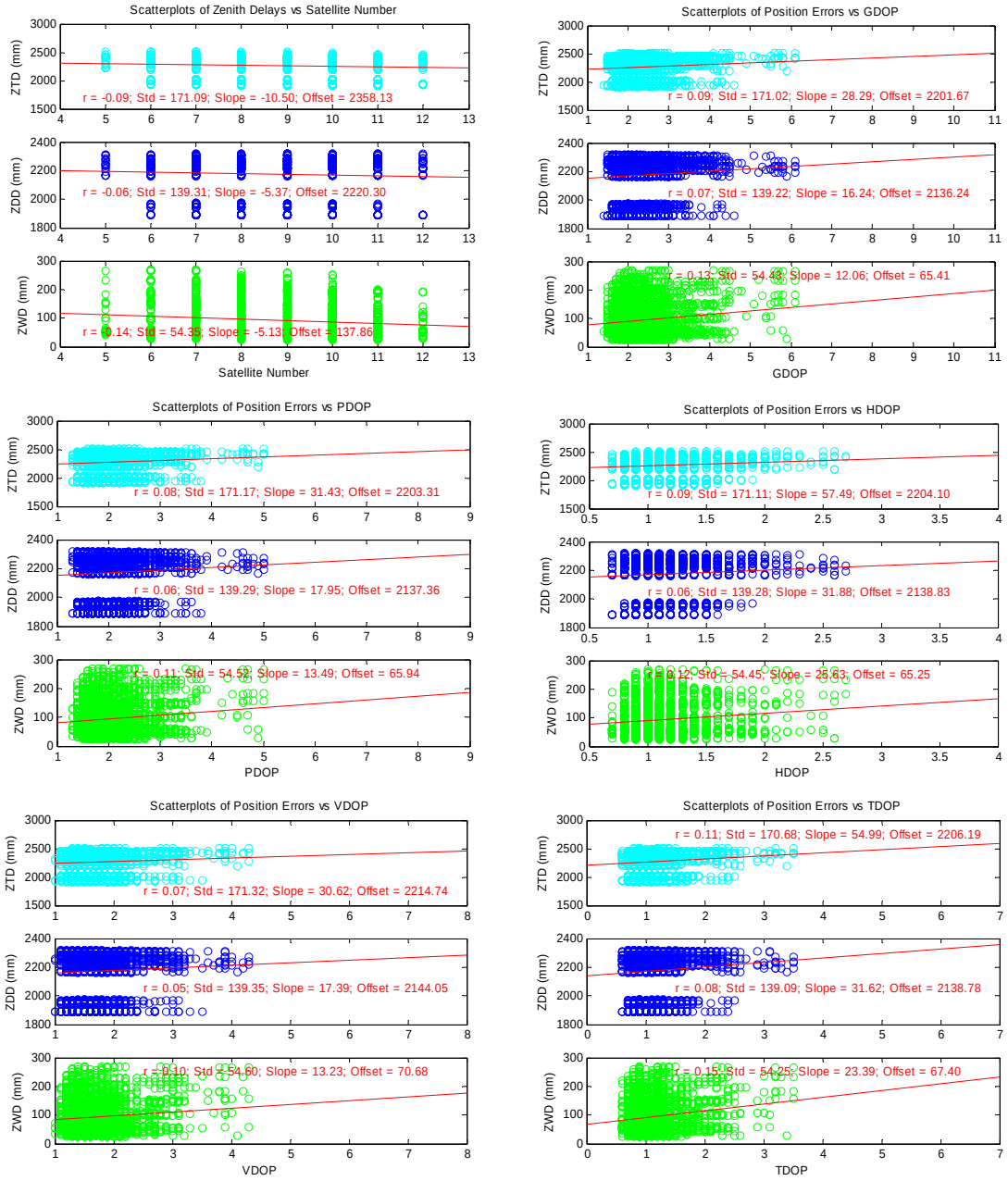

Figure 7.7 Scatter plots of Zenith Delays vs Satellite Geometric Factors

7.3.4 Correlation between satellite geometry factors and position errors

This correlation analysis investigates how satellite geometry factors influence the position errors. Table 7.7 gives the correlation coefficients between these two types of variables and corresponding significant test results. The scatter plots between these types of variables are shown in Figure 7.8. Although the values of correlation coefficients are

not high, the significant correlation tests indicate that the *weak* correlations exist between most of them. The two obvious indications are:

(1) That satellite geometric variables exert impact mainly on *east* and *up position errors*; the impacts on *the latter* (from -20 to -80 mm) are much bigger than on *the former* (from -10 to 25 mm); and

(2) That in this association, *HDOP* is the most significant contributor to position errors.

Table 7.7 Correlation coefficients between position errors and satellite geometric variables and corresponding significant tests

Correlation coefficient (r)				**Correlation test** $(N = 4980, \alpha = 0.01)$					
Satellite geometric variable	**Position Error**			*East*		*North*		*Up*	
	East	*North*	*Up*	Sample value	Popul-ation value	Sample value	Popul-ation value	Sample value	Popul-ation value
Satellite #	0.1746	-0.0887	0.1481	12.30	2.412	-6.283	-2.412	10.566	2.412
GDOP	-0.1188	0.0101	-0.0918	-15.525	-2.412	0.713*	2.412	-6.504	-2.412
PDOP	-0.1050	0.0168	-0.0792	-7.449	-2.412	1.185*	2.412	-5.606	-2.412
HDOP	-0.1477	-0.0017	-0.1546	-10.537	-2.412	-0.120*	-2.412	-11.041	-2.412
VDOP	-0.0761	0.0249	-0.0405	-5.385	-2.412	1.757*	2.412	-2.86	-2.412
TDOP	-0.1509	0.0007	-0.1180	-10.77	-2.412	-0.049*	2.412	-8.384	-2.412

*: means that test failed, *i.e.*, no significant correlation

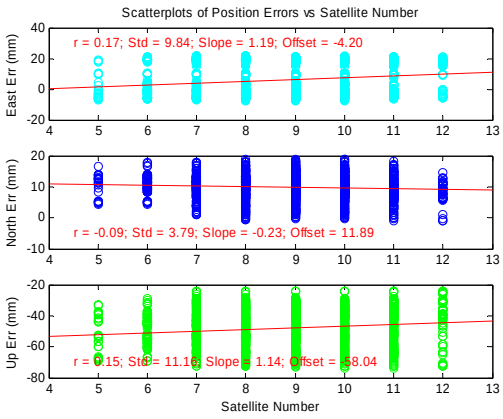

(a) *Position errors vs satellite #*

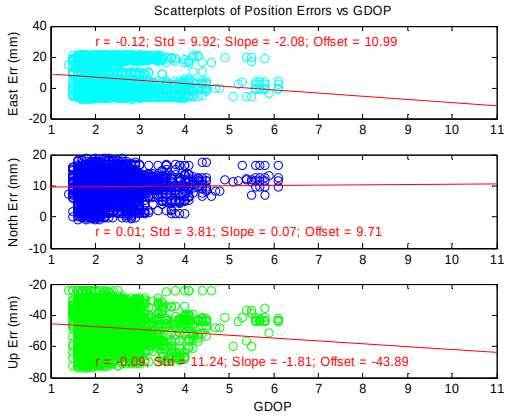

(b) *Position errors vs GDOP*

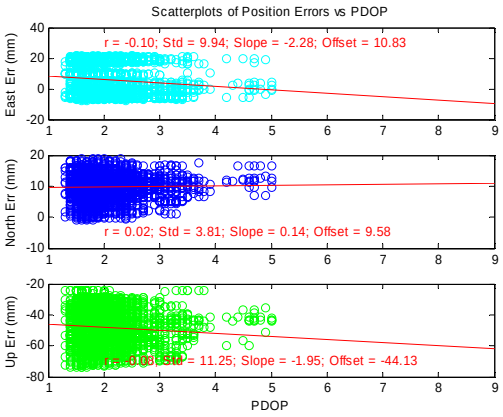

(c) *Position errors vs PDOP*

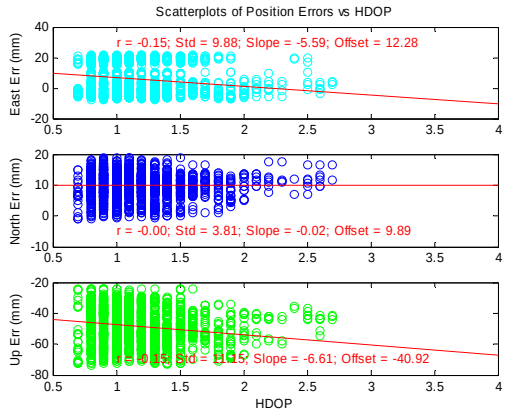

(d) *Position errors vs HDOP*

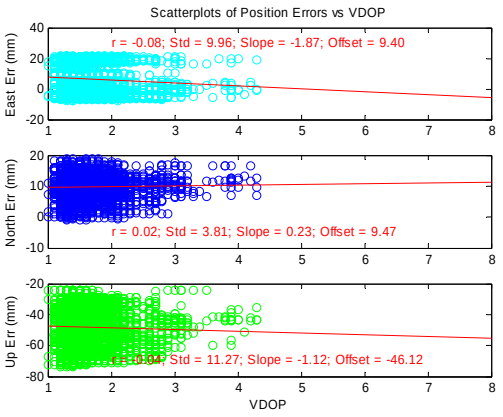

(e) *Position errors vs VDOOP*

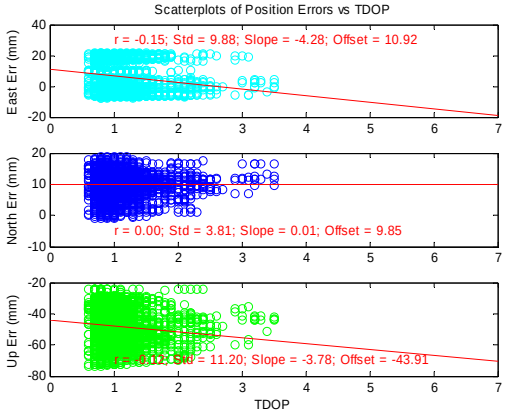

(f) *Position errors vs TDOP*

Figure 7.8 Scatter plots of position errors vs satellite geometric factors

7.3.5 Correlation between PWV bias and satellite geometric factors

This correlation analysis investigates how satellite geometric variables impact the measurements of PWV. The significant correlation test results are given in Table 7.8 and the corresponding scatterplots are shown in Figure 7.9. Table 7.8 does not show strong correlations between these two types of variables. The notable association is between PWV bias and satellite number: *PWV bias* decreases as the satellite number increases (Figure 7.9); this means that the more satellites the more accurate measurement of PWV.

Table 7.8 Correlation Coefficients of PWV bias and Satellite Geometric Variables

Correlation coefficient (r)		**Correlation test** $(N = 4980, \alpha = 0.01)$	
Satellite geometric variable	**PWV bias**	Sample value	Population value
Satellite #	0.0837	5.926	2.412
GDOP	-0.0464	-3.277	-2.412
PDOP	-0.0463	-3.270	-2.412
HDOP	-0.0233	-1.644*	-2.412
VDOP	-0.0514	-3.631	-2.412
TDOP	-0.0526	-3.716	-2.412

*: means that test failed, *i.e.*, no significant correlation

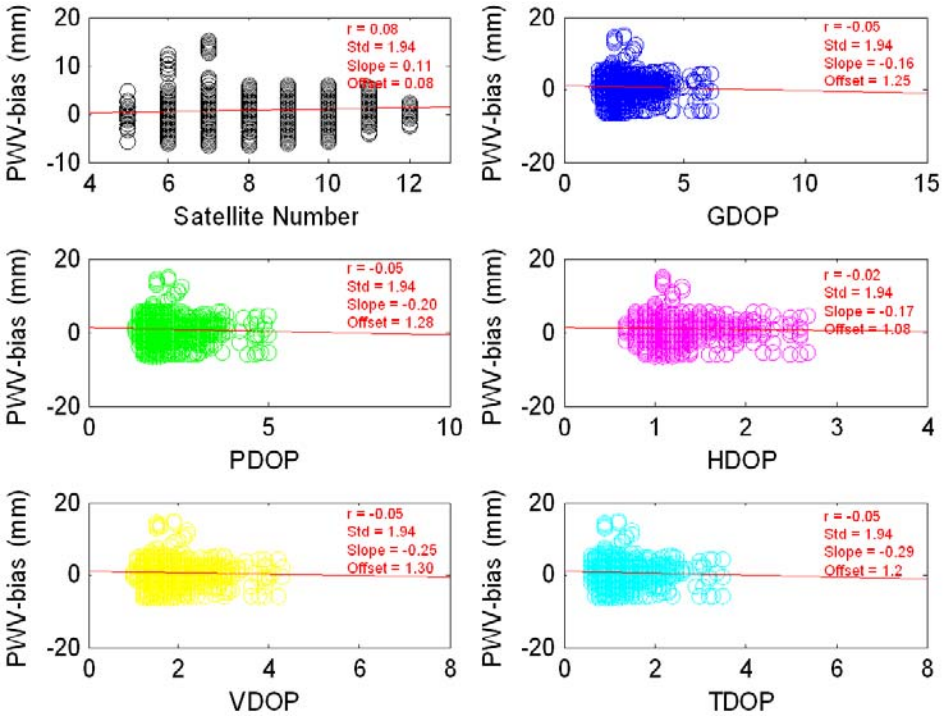

Figure 7.9 Scatter plots of PWV bias vs Satellite Geometric Factors

7.3.6 Correlation between zenith delays and position errors

This correlation analysis investigates how zenith delays contribute to the position errors. The correlation coefficients between these two types and the corresponding significant test results are given in Table 7.9. The scatter plots between these two types of variables are shown in Figure 7.10. The analytical results show:

(1) That *ZTD*/*ZDD* mainly contribute to *east* and *up position errors*: (1) as ZTD/ZDD increases *east position errors* either decrease in positive domain or increase in negative domain; (2) as *ZTD/ZDD* increase, *up position errors* increase in negative domain;

(2) That *ZWD* mainly and positively contributes to *horizontal* position errors; and

(3) That *up position errors* have bigger varying ranges than both *east position errors* do.

Table 7.9 Correlation Coefficients of Zenith Delays and Position Errors

Correlation coefficient (*r*)				**Correlation test** $(N = 4980, \alpha = 0.01)$					
Zenith delay	**Position Error**			*East*		*North*		*Up*	
	East	*North*	*Up*	Sample value	Popul-ation value	Sample value	Popul-ation value	Sample value	Popul-ation value
ZTD	-0.6635	-0.0815	-0.2444	-62.57	-2.412	-5.769	-2.412	-17.783	-2.412
ZDD	-0.6974	-0.1902	-0.3385	-68.657	-2.412	-13.669	-2.412	-25.381	-2.412
ZWD	-0.3041	0.2285	0.0956	-22.522	-2.412	16.560	2.412	6.776	2.412

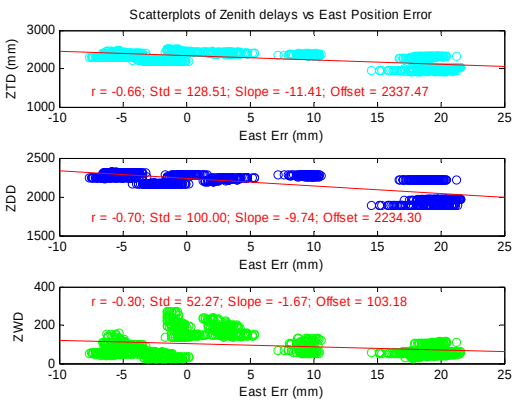

(a) *Zenith delays vs east position error*

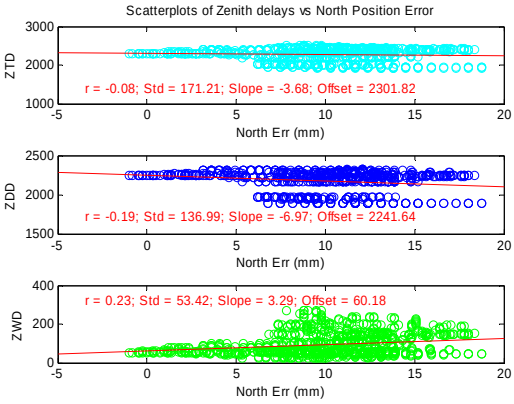

(b) *Zenith delays vs north position error*

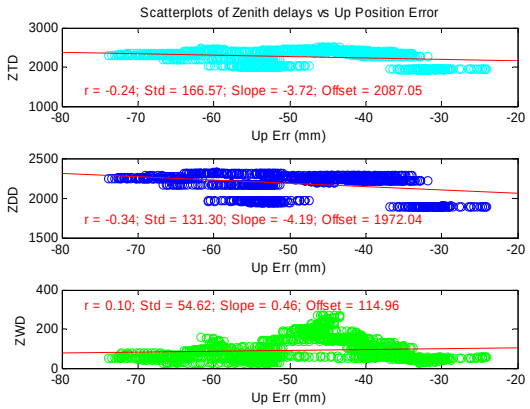

(c) Zenith delays vs up position error

Figure 7.10 Scatterplots of Zenith Delays vs Position Errors

7.3.7 Correlation between PWV bias and position errors

Some author (Skone et al., 2006) mentioned that position errors could contribute to PWV bias error. This issue is validated using the correlation coefficient test. Table 7.10 gives the correlation coefficients of each individual station; the correlation coefficient of all-nine-station is given in last line. Each individual station correlation coefficients are also plotted in Figure 7.11. The all-nine-station scatter plot of PWV bias vs position errors is shown in Figure 7.12. The significant correlation tests for each individual station show that 80% of *east*, 90% of *north* and 55% of *up* position errors associate with PWV bias; but the significant correlation tests of all-nine-station statistics indicates that only *east* and *north position errors* have associations with PWV bias.

Table 7.10 Correlation coefficients and significance test

Correlation coefficient (r)				**Correlation test** $(N = 4980, \alpha = 0.01)$					
PWV bias (at Station)	**Position error**			*East*		*North*		*Up*	
	East	*North*	*Up*	Sample value	Popul-ation value	Sample value	Popul-ation value	Sample value	Popul-ation value
100	0.4320	-0.1774	0.0311	11.213	2.412	-4.22	-2.412	0.728*	2.412
101	0.5908	-0.0122	0.1979	17.142	2.412	-0.286*	-2.412	4.726	2.412
102	-0.2895	0.1685	0.4913	-7.08	-2.412	4.002	2.412	13.205	2.412
104	0.4466	0.5140	-0.0669	11.685	2.412	14.027	2.412	-1.57*	-2.412
105	0.3611	-0.2494	-0.2808	9.065	2.412	-6.029	-2.412	-6.849	2.412
107	0.0243	-0.5313	-0.1154	0.569*	2.412	-14.681	-2.412	-2.72	2.412
109	0.4020	-0.2610	-0.0726	10.278	2.412	-6.329	-2.412	-1.704*	-2.412
112	0.2577	0.2269	0.0027	6.243	2.412	5.454	2.412	0.063*	2.412
115	0.0207	-0.1483	0.1438	0.485*	2.412	-3.51	-2.412	3.402	2.412
All nine stations (N = 4980)	**0.1706**	**-0.1723**	**-0.0193**	12.216	2.4121	-12.341	-2.412	-1.362*	-2.412

*: means that test failed, *i.e.*, no significant correlation

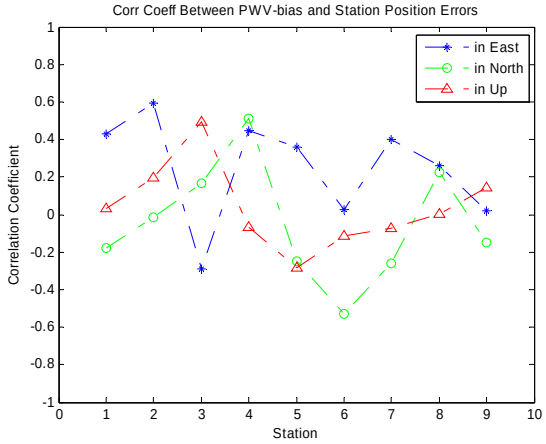

Figure 7.11 Plots of correlation coefficients of PWV biases versus position errors

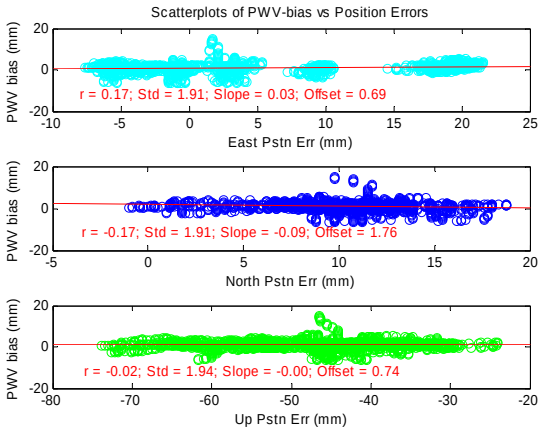

Figure 7.12 Scatter plots of PWV bias versus position errors

7.4 Summary

The GPS water vapour dataset consists of four types of intercorrelated variables, which are 17 by number. Principal component analysis has been performed to simplify the description of the GPS water vapor dataset. Variable correlation analysis has been also carried out to further investigate and explain the between-type relationship among those four variable types.

The PCA of the GPS water vapor dataset derives a seven-principal-component/domain structure of the GPS water vapor dataset: *Size of DOP*, *Volume of ZDD*, *Moisture Content*, *Volume of ZWD*, *Volume of Up Position Error*, *East-Up* (*Position*) *Error Contrast* and *Volume of PWV Bias*. In the GPS water vapor measurement system (without GPS receiver clock error), *Size of DOP* takes up 34.23% of the variance; *Volume of ZDD* 15.92%; *Moisture Content* 10.73%; *Volume of ZWD* 8.31%; *Volume of Up Position* 7.08%; *East-Up Error Contrast* 6.45% and *Volume of PWV Bias* 5.56%. All the seven principal components explain the variances of the system by 88.30%.

The correlation analysis focuses on the seven between-subset associations between four types of variables. These analytic results show that:

(1) All Zenith Delays have *positive* associations with Meteorological Parameters: (i) ZTD associates *strongly* with pressure (r = 0.96); (ii) ZWD is *strongly* associated with Temperature (r = 0.83); and (iii) ZWD has a *weaker* association with Humidity (r = 0.37) than it does with temperature;

(2) The associations exist between Position Errors and Meteorological Parameters as follows: (i) both Pressure and Temperature largely, *negatively* contribute to east position error (r = -0.69 and r = -0.35); and (ii) Humidity largely, *positively* contributes to Up Error (r = 0.47);

(3) Zenith Delays have *weak* associations with Satellite Geometrical Factors: (i) *all* six satellite geometrical factors mainly contribute to *ZWD*; (ii) *all* DOPs have *positive* associations with zenith delays;

(4) A weak association exists between position errors and satellite geometric factors as follows: (i) HDOP is the most significant contributor to the position errors; (ii) satellite geometric factors exert impact mainly on *east* and *up*

position errors and the impacts on *the latter* (from -20 to -80 mm) are much bigger than on *the former* (from -10 to 25 mm);

(5) PWV bias has very weak association with satellite geometric factors;

(6) ZTD/ZDD has a strong association with *east error*: east errors *either* decrease in positive domain *or* increase in negative domain as ZTD/ZDD increases; and

(7) Both east and north position error has a weak association with PWV bias.

Chapter Eight: Conclusions

Atmospheric water vapor plays a crucial role in the climatic systems (transporting moisture and latent heat), in particular over high latitudes where water vapor exhibits a significant seasonal variability. Better knowledge of the global distribution of atmospheric water vapor in space and time will improve the performance of weather prediction and climate monitoring. In Canada, the sparse spatial and temporal sampling of atmospheric water vapor observations needs to be improved. Conventional radiosonde technique can not meet this requirement. Water vapor radiometry (WVR) can not either, since it has poor spatial resolution and is also limited in high-latitude areas like the Arctic. The GPS atmospheric remote sensing technology has been proved to be a key method to improve high latitude sparse spatial and temporal sampling of water vapor observation in Canada. In this thesis, the method for developing a near real-time GPS water vapor sensing system using GPS PPP technique and Canada sparse geodetic GPS network has been presented. The fundamental problems addressed in this work are (i) how to design/implement a workable distributed GPS water vapor sensing network, (ii) how to evaluate the system performance, (iii) how to create an interpolated map of (near real time) water vapor, and (iv) how to investigate the hidden variable relations in a GPS water vapor dataset.

8.1 Contributions

In this thesis, the following ideas and approaches were utilized to develop the real-time GPS PPP-inferred water vapor system.

(1) A distributed real-time GPS PPP-inferred water vapor remote sensing system has been realized, in which distributed GPS data sources (network) and distributed computing facility (PPP software) cooperate under network protocols. The system concurrently and continuously processes 21-station data and produces near real-time tropospheric products: ZTD/ZWD/PWV for each station under all weather conditions. In the future when the GPS network is expanded, *i.e.*, more stations

are added, the increased workload of data processing can easily be distributed over network to newly added GPS processing centers.

(2) The performance of the developed system has been analyzed in three aspects: *position errors*, *ZTD* and *PWV*. The results show: (i) the position errors: RMS = l.1 ~ 4.3 cm; (ii) the significant position error occurs in the *up* direction which has relation to the un-modeled atmospheric errors; (iii) the ZTD and PWV accuracies of the current (near) real-time water vapor system are ~13 mm and ~2 mm, respectively, which should be improved if the real-time Meteorological data stream were available to the system.

(3) An *ordinary kriging* program has been developed in Matlab, which generates near real-time interpolated surface maps of PWV over Canada using the limited available sample datasets. The Matlab program consists of three steps: (i) Calculating experimental semivariogram; (ii) Estimating semivariogram model (model fitting); and (iii) Estimating surface map of PWV by ordinary kriging. In step one, the reliability of the calculated experimental semivariogram impacts the best model choosing, and consequently the accuracy of kriging interpolation. In step two, firstly, three different semivariogram models: *Spherical*, *Exponential* and *Gaussian* are fitted by *nonlinear weighted least-squares* respectively and then the best fitted model is determined by *cross-validation process*. In step three, the interpolated PWV maps and associated kriging standard error maps are generated by ordinary kriging algorithm.

(4) The kriginged PWV maps over Canada and associated kriging standard error maps based on the sparse and limited sample dataset provide valuable information to other applications, and they are also used to evaluate the meteorological role of Canada geodetic GPS network.

(5) The experiments show that the accuracy of the estimated PWV values does not depend directly on the observation values but on the semivariogram and the configuration of the sample points. The current Canada (real-time) GPS network has a small number of (real-time) GPS stations and its configuration is not balanced in Canada domain. In order to improve the accuracy of the estimated

PWV maps, the configuration of the GPS network needs improving by increasing the number of GPS stations and properly deploying them within the network.

(6) 17 variables of the GPS water vapor dataset derived from the developed system are sorted into 4 categories. *Principal Component Analysis* has been performed to simplify the description of this set of intercorelated variables. A seven-principal component/domain structure of the GPS water vapor dataset is found: *Size of DOP, Volume of ZDD, Moisture Content, Volume of ZWD, Volume of Up (Position) Error, East-Up (Position) Error Contrast* and *Volume of PVW Bias*. All the seven principal components explain the variance of the whole dataset by 88.30%; among it, *Size of DOP* explains 34.23%, *Volume of ZDD* 15.92%, *Moisture of Content* 10.73% and *Volume of ZWD* 8.31%.

(7) *Variable Correlation Analysis* has been further performed on the GPS water vapor dataset to investigate seven between-type relations among those 4 types. The Correlation Analysis uses scatterplot and linear regression techniques to quantitatively provide meaningful results to validate those seven relations.

The results of this study suggest that PPP technique integrated with a sparse GPS reference network is an efficient approach to estimate atmospheric water vapor in Canada and the developed system performance could reach an accuracy level comparable with other operational GPS networks. The near real-time GPS PPP-inferred water vapor system provides valuable information and experiences for the construction of workable operational GPS network for meteorology in Canada.

8.2 Future works

Some aspects of this research work still need to be addressed.

(1) At present, the developed system works under *near* real-time mode because of using one-hour-latency MET files. When the real-time MET data stream is available, the system needs to be switched to real-time mode and its performance needs to be validated again.

(2) In this thesis, the comparable post-mission results were derived based on IGS *final* GPS satellite orbits and clocks data. To get a more accurate and comparable

performance validation, a PPP post-mission program which uses the recorded *real-time* JPL satellite orbit and clock correction data needs to be created.

(3) In order to produce more accurate interpolated surface maps of PWV, *universal kriging* algorithm may be implemented in the kriging program since the *universal kriging* models the spatial process trend as a simple polynomial function instead of a constant, which is a more general case of spatial variable.

(4) The PCA-derived conclusions obtained in near real-time mode need to be further validated when the developed system works under real-time mode.

Appendix A: Coefficients for Neill's Mapping Function

The coefficients for Neill's mapping functions m_d (2.24) and m_{wv} (2.25) are given in Table A.1 and Table A.2 as a function of the latitude φ of the station. If $\varphi < 15°$ the values for $\varphi = 15°$ should be used; if $\varphi > 75°$ then the values for $\varphi = 75°$ should be used; if $15° \le \varphi \le 75°$, then linear interpolation applies. Before substitution, however, the coefficients *a*, *b*, and *c* in Equation 2.24 (m_d) must be corrected for periodic terms using the following general formula: (Leick, 2004)

$$a(\varphi,\ \mathrm{DOY}) = \tilde{a} - a_p \cdot \cos\left(2\pi \cdot \frac{\mathrm{DOY} - \mathrm{DOY}_0}{365.25}\right) \qquad \text{(A.1)}$$

where DOY denotes the day of year and DOY_0 is 28 or 211 for stations in the Southern or Northern Hemisphere, respectively.

Table A. 1: Coefficients for Niell's Hydrostatic Mapping Function

φ	$\tilde{a} \cdot 10^3$	$\tilde{b} \cdot 10^3$	$\tilde{c} \cdot 10^3$	$a_p \cdot 10^5$	$b_p \cdot 10^5$	$c_p \cdot 10^5$
15°	1.2769934	2.9153695	62.610505	0	0	0
30°	1.2683230	209152299	62.837393	1.2709626	2.1414979	9.0128400
45°	102465397	209288445	63.721774	2.6523662	3.0060779	4.3497037
60°	102196049	209022565	63.824265	3.4000452	7.2562722	84.795348
75°	102045996	2.9024912	64.258455	4.1202191	11.723375	170.37206
	$a_h \cdot 10^5$	$b_h \cdot 10^3$	$c_h \cdot 10^3$			
	2.53	5.49	1.14			

Table A. 2: Coefficients for Neill's Wet Mapping Function

φ	$a \cdot 10^4$	$b \cdot 10^3$	$\tilde{c} \cdot 10^2$
15°	5.8021897	1.4275268	4.3472961
30°	5.6794847	1.5138625	4.6729510
45°	5.8118019	1.4572752	4.3908931
60°	5.9727542	1.5007428	4.4626982
75°	6.1641693	1.7599082	5.4736038

Appendix B: Introduction to Network Protocol

The realization of the real-time water vapor sensing system relies on the Internet. UDP and IP Multicast are the two Internet communication protocols used in this thesis. To help understanding, the basic concepts on network protocol are briefly illustrated below.

B.1 Network transmission models

The network transmission models are also called network addressing methods. There are three basic network transmission models: *Unicast*, *Broadcast* and *Multicast* (Figure B-1). The number of transmitter (sources) and receivers (destinations) portray the different models.

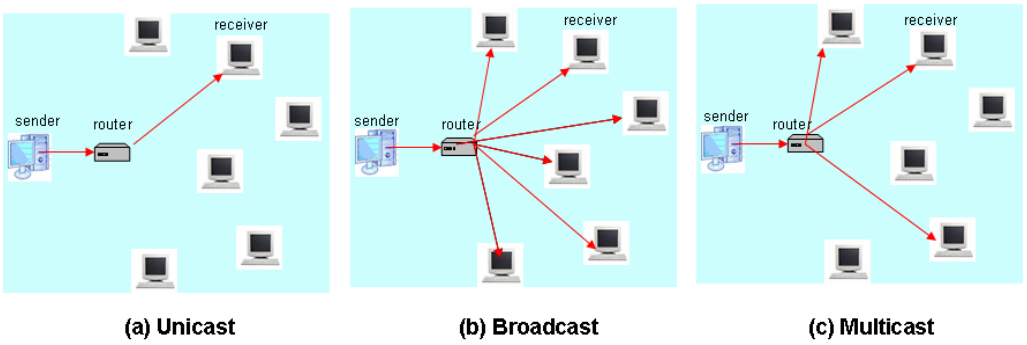

Figure B-1 Transmission models

- Unicast transmission

This is the traditional data transmission on the Internet, between one specific source and one specific receiver, i.e., single sender and single receiver (Figure B-1 (a)). The vast majority of all data transmissions on the Internet today are Unicast. The unicast flow is the basic building block found in all networks.

- Broadcast transmission

In this model, a host sends a message to all other hosts, i.e., single sender and global receivers (Figure B-1 (b)). The model is used when a piece of information needs communicating to every host on the network, or used when the sender needs to send a message to just one receiver, but doesn't know its address.

The problem with the model is that sending the broadcast everywhere is a significant usage of network resources if not all the hosts need to see the packets. This global transmission can cause unnecessary traffic.

- Multicast transmission

Multicast model is similar to broadcast model in that there is a one-to-many traffic pattern. The difference is that the receiving hosts are a subset of all the hosts, i.e., single sender and selected receivers (Figure B-1 (c)). This model enables a single host to send data to a specific set of hosts by making just a single call. Multicasting can conserve network bandwidth by reducing the amount of unnecessary network traffic. In addition, it is the most economic technique for sending a packet stream from one location to many other locations on the Internet simultaneously.

B.2 Protocol layering

Protocols are sets of standards which define how data are represented when they are being transmitted from one machine to another. Protocols govern the communications between computers on a network: how the transmission occurs, how errors are detected, and how acknowledgements are passed (Comer, 2000). To simplify protocol design and implementation, network communication functionality is organized into a layered protocol model, in which each layer corresponds to one protocol that deals with one part of the communication problem (Figure B-2). Figure B-2 delineates the Open System Interconnection Reference Model designed by the International Organization for Standardization (ISO) and the corresponding Internet protocols. The Networking-layer protocol is Internet Protocol (IP) and the Transport-layer protocols are Transmission Control Protocol (TCP) and User Datagram Protocol (UDP). The access interface between protocols is implemented through protocol ports. Each protocol port is identified by a positive integer (Figure B-3).

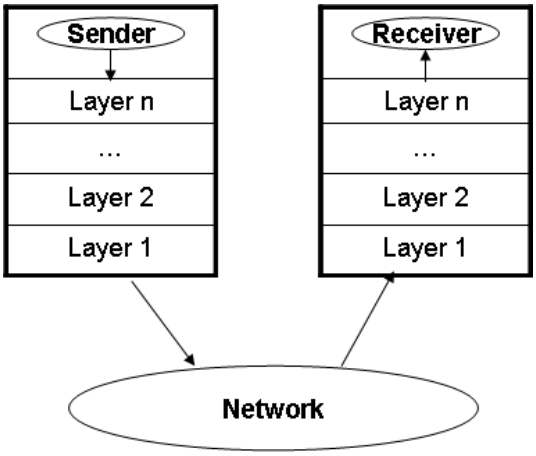

Figure B-2 The conceptual organization of protocol software in layers

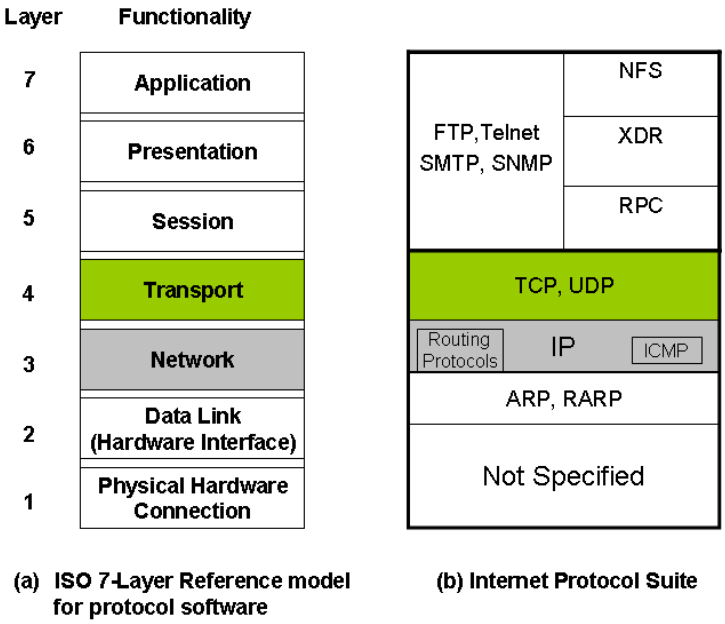

Figure B-3 OSI model layer and Internet protocols (Cisco Documentation) Cisco Documentation, Internet Protocol. (Chow, 2006)

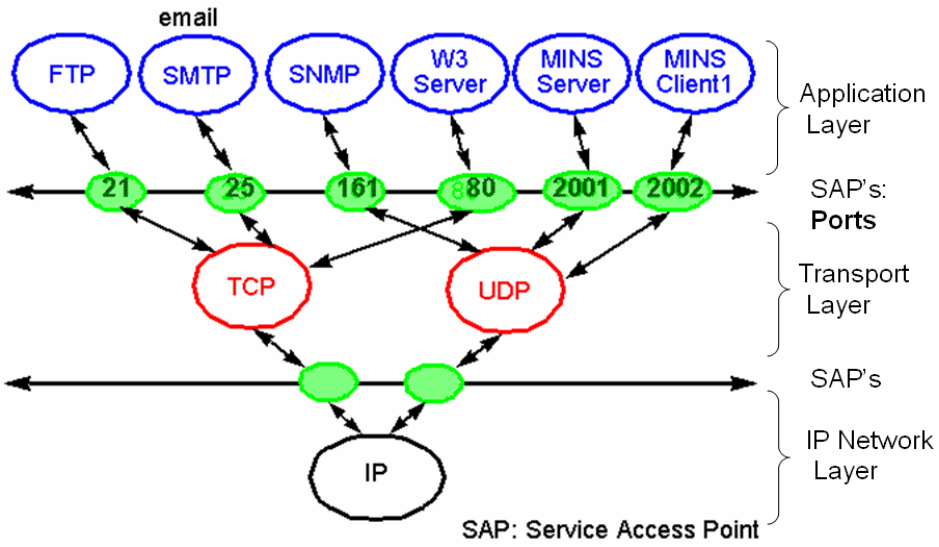

Figure B-4 Example – A UNIX workstation network interface (Adapted from: Chow (2006))

B.3 IP, UDP and IP Multicast protocols

The common network protocols used in this thesis are introduced below.

Internet Protocol (IP). IP is the networking-layer protocol which specifies the format of packets/datagrams (a piece of a message transmitted over network) and the addressing scheme. IP functions like the postal system. It allows the sender to address a package and drop it in the system, but there's no direct link between the sender and the receiver. Thus, the service provided by IP is a connectionless, best-effort delivery service. But, when it is combined with a higher-level transport-layer protocol called Transmission Control Protocol (TCP), it establishes a connection between two hosts so that both can send messages back and forth.

User Datagram Protocol (UDP). UDP is a core transport-layer protocol defined for use with the IP network layer protocol. Like IP, UDP provides a connectionless and unreliable (no acknowledge) service that provides no guarantees for delivery and no protection from duplication. It merely sends out the message. Due to its simplicity and low overhead, UDP may be adequate in many cases.

UDP provides a few functions beyond that of IP:

- Port numbers. They are 16-bit destination port number and 16-bit source port number and let multiple processes use UDP services on the same machine. A UDP address is a combination of 32-bit IP address and the 16-bit number.
- Checksum. Unlike IP, UDP does checksum its data, ensuring data integrity.

0

IP Multicast protocol. IP Multicast is a protocol for transmitting IP datagrams from one source to many destinations in a local or wide-area network of hosts (Figure B-1 (c)). The current standard of IP is unicast transmission service (Figure B-1 (a)), *i.e.*, each packet sent is forwarded from a single source host to a single destination host identified by its IP address. For IP multicast, the IP address refers to a group of IP hosts. This is done by modifying IP protocol by adding *multicast routing* support to it. Besides this, IP Multicast use UDP as its underlying transport protocol.

The idea of a basic IP multicast model is that any host can join a given multicast group G, and any host can send a packet with destination address G, and have it delivered to all members of the group G. The sender does not need to be a member of G (Intro to IP muticast, The Norwegian research network).

The advantages with IP multicast are (i) that it conserves bandwidth; (ii) that it can construct truly distributed applications and (iii) that it provides important performance optimisations over unicast transmission.

In the thesis, IP multicast is used to transmit the real-time GPS data from Canadian geodetic (GPS) network, which makes it possible for all receivers who are interested in the data to share the same information simultaneously. Likewise, when the demand of calculation resource is increased with more added GPS stations in the system, the system can easily divide the workload into more servers using IP multicast.

References

Alan, D., and P. Shardlow (1995). *The global positioning system as a passive integrated atmospheric water vapour sensing device*. The international society for opti proceeding of SPIE, Atmospheric sensing and modeling II.

Afifi, A., V.A. Clark and S. May. (2004). *Computer-Aided Multivariate Analysis*, Chapman & Hall/CRC.

Awange, J.L., and E.W. Grafarend (2005). *Solving algebraic computational problems in geodesy and geoinformatics*. Springer.

Basu, S., R.F. Gunst, E.A. Guertal, and M.I. Harifield (1997). The effects of influential observations on sample semivaiograms, *Journal of Agricultural, Biological, and Environmental Statistics*, Vol. 2, No. 4, pp: 490-512.

Barry, R. and R. Chorley (2003). *Atmosphere, Weather and Climate*. Routledge (download from: http://www.weather-climate.org.uk/01.php).

Bishop, C.M. (2006). *Pattern recognition and machine learning*. Springer.

Bengtsson, L., G. Robinson, R.Anthes, K. Aonashi, A. Dodson, G. Elgered, G. Gendt, R. Gurney, M. Jietai, C. Mitchell, M. Mlaki, A. Rhodin, P. Silvestrin, R. Ware, R. Watson, and W. Wergen (2003). The use of GPS measurements for water vapor determination, *American Meteorological Society*, Sept., pp: 1,249-1,258.

Bevis, M., S. Businger, T.A. Herring, C. Rocken, R.A. Anthes, and R.H. Ware (1992). GPS meteorology: remote sensing of atmospheric water vapour using the global positioning system, *Journal of Geophysical Research*, Vol. 97, No. D14, 15,787-15,801.

Bohling, G. (2005). Introduction to geostatistics and variogram analysis, pdf file (downloaded from http://people.ku.edu/~gbohling/cpe940/Variograms.pdf).

Bokoye, A.I., A. Royer, N.T. O'Neill, P. Cliché, L.J.B. McArthur, P.M. Teillet, G. Fedosejevs, and J.-M. Theriault (2003). Multisensor analysis of integrated atmospheric water vapor over Canada and Alaska, *Journal of Geophysical Research*, Vol. 108, No. D15 4480.

Brocard, E. (2006). Overview on satellite experiments which measure atmospheric water vapour. IAP Research Report. Institut fur angewandte Physik, University Bern, Switzerland.

Brunner, F.K. and W.M. Welsch (1993). Effect of the troposphere on GPS measurements, *GPS world*, January 1993, 42-51.

Bruyninx, C. (2008). Present Status and Modernization Plans, Royal Observatory of Belgium (download from: http://www.gps.oma.be/gb/modern_gb_ok_css.htm).

Businger, S., M. Bevis, S.R. Chiswell, and J. Duan (1996). The promise of GPS in atmosphere ic monitoring, *Bulletin of the American Meteorological Society*, Vol. 77, No. 1, pp: 5-18.

Cardall and Daunt (2008). Astronomy 161: The solar system (downloaded from: http://csep10.phys.utk.edu/astr161/lect/earth/atmosphere.html).

Cess, R.D. (2005). Atmospheric science: water vapour feedback in climate models, *Science*, Vol 310. No. 5749, pp: 795-796.

Champollion, C., F. Masson, M.-N. Bouin, A. Walpersdorf, E. Doerflinger, O. Bock, and J. Van Baelen (2005). GPS water vapour tomography: preliminary results from the ESCOMPTE field experiment, *Atmospheric Research*, Vol. 74, Issues 1-4, pp: 253-274.

Chen, G., and T.R. Herring (1997). Effects of atmospheric azimuthal asymmetry on the analysis of space geodetic data, *Journal of Geophysical Research*, Vol. 102, No. B9, pp: 20,489-20,502.

Chow, C. (2006). Introduction to network and protocol (http://cs.uccs.edu/~cs522/intro)

Cressie, N. 1994. 'Spatial chemostatistics', in Cothern, C.R. *et al*. (eds), *Environmental statistics, assessment, and forecasting*, CRC Press, pp: 131-146.

Deblonde, G. and S. Macpherson (2005). Evaluation of GPS precipitable water over Canada and the IGS network, *American Meteorological Society*, Jan. pp: 153-166.

Dodson, A.H., P.J. Shardlow, L.C.M. Hubbard, G.Elgered, and P.O.J. Jarlemark (1996). Wet tropospheric effects on precise relative GPS height determination, *Journal of Geodesy*, 70:188-202.

Fuentes, M. (2002). Spatial interpolation of environmental processes, in: Mateu, J. *et al*. (eds), *Spatial statistics through applications*, WIT Press, 69-102.

Gao, Y., and X. Shen (2001). Improving ambiguity convergence in carrier phase-based precise point positioning, *Proceeding of ION GPS 2001*, 11-14 September, Salt Lake City, Utah, USA, pp: 1,532-1,539.

Gao, Y., S. Skone, K. Chen, and N.A. Nicholson (2004). Real-time sensing atmospheric water vapor using precise GPS orbit and clock products, *Proceedings of ION*, Long Beach, CA.

Willkommen (2005). GPS - explained (downloaded from: http://www.kowoma.de/en/gps/orbits.htm).

Gutman, S.I., S.R. Sahm, S.G. Denjamin, and T.L. Smith (2004). GPS water vapor observation errors. *Eighth Symposium on Integrated Observing and Assimilation Systems for Atmosphere, Oceans, and Land Surface*.

Haan, S. de (2006). National/regional operational procedures of GPS water vapour networks and greed international procedures, *Instruments and observing methods report No. 92*, World Meteorological Organization.

Hagemann, S., L. Bengtsson, and G. Gendt (2002). On the determination of atmospheric water vapor from GPS measurements. MPI Report 340, ISSN 0937-1060.

Hall, G.A., W. Tao and J.C. Munson (2005). Measurement and validation of module coupling attributes, *Software Quality Journal*, 13, 281-296.

Hidore, J.J. (1972). *A geography of the atmosphere*, 2nd edition, Wm. C. Brown Company Publishers.

Hieb, Monte (2003). Water vapour rules the greenhouse system (downloaded from: http://www.geocraft.com/WVFossils/greenhouse_data.html).

Hoyle, V., S. Skone, and S. Shrestha (2003). The use of global positioning system to derive atmospheric water vapour distribution for environmental applications, *Environmental Informatics Archives*, Vol. 1 512-523.

IHF (2008). *Optimierung von GrundwassermeBnetzen mit dem Kriging-Verfahren*, Freiburger Schriften zur Hydrologie, Institute of Hydrology (download from: http://www.hydrology.uni-freiburg.de/publika/band03-sum.html).

Jian, X., R.A. Loea, and Y.S. Yu (1996). Semivariogram modeling by weighted least squares, *Computers & Geosciences*, Vol. 22, No.4, pp: 387-397.

Kruse, L.P. (2001). Spatial and Temporal distribution of atmospheric water vapour using space geodetic techniques, *Einundsechzigster Band*, Vol 61.

Krzanowski, W.J. (1988). *Principles of multivariate analysis*, Oxford University Press, Walton street, Oxford OX2 6DP.

Kouba, J., and P. Heroux (2001). Precise point positioning using IGS orbit and clock Products, *GPS Solutions*, Vol. 5, No. 2, pp: 12-28.

Kuo, Y,-H., Y.-R, Guo, and E. Westwater (1993). Assimilation of precipitable water measurements into a mesoscale numerical weather model, *Monthly Weather Review*, 121, pp: 1,215-1,238.

Kursinski, E.R. and G.A. Hajj (2001). A comparison of water vapour derived from GPS occultations and global weather analyses, *Journal of geophysical research*, Vol. 106, No.D1, pp: 1,113-1,138.

Langley R. (1990). Why is the GPS signal so complex? *GPS World*, May/June, p. 56.

Leick, A. (2004). *GPS satellite surveying*, John Wiley & Sons, Inc.

Li, P.W., X.Y. Wang, Y.Q. Chen, and S.T. Lai (2005). Use of GPS signal delay for real-time atmospheric water vapor estimation and rainfall nowcast in Hong Kong, *The First International Symposium on Cloud-prone & Rainy Areas Remotes Sensing*, Chinese University of Hong Kong, October 6-8, 2005.

VOLUME XXXIV, PART2, COMMISSION II, Xi'an, Aug. 20-23, 2002.

McBratney, A.B. and R. Webster (1986). Choosing functions for semi-variograms of soil properties and fitting them to sampling estimates, *Journal of Soil Science*, 37, 617-639.

Melbourne W.G., E.S. Davis, C.B. Duncan, G.A. Hajj, K. Hardy, R. Kursinski, T.K. Mechan, and L.E. Young(1994). *The application of spaceborne GPS to atmospheric limb sounding and global change monitoring*, JPL Publication pp: 94-18.

Michelsen, M.W. (1998). GPS 'Noise" Benefits Weather Forecasting. Earth Observation Magazine, Oct. (downloaded from: http://www.eomonline.com/Common/Archives/1998oct/98oct_michael.html).

Misra, P., and P. Enge (2001). *Global positioning system*, Ganga-Jamuna Press.

Neill, A.E. (1996). Global mapping functions for the atmosphere delay at radio Wavelengths, *Journal of Geophysical Research*, Vol. 101, No. B2, pp: 3,227-3,246.

Nelson, M.R., T.V. Orm, R. Jaime-Garcia and A. Nadeem (1999). Applications of geographic information systems and geostatistics in plant disease epidemiology and management, *Plant Disease*, Vol. 83, No. 4, pp: 308-319.

Nielsen, A.A. (2007). Least Squares adjustment: linear and nonlinear weighted regression analysis.

NRCan (2005). Real-time IGS archiver (RTIGSA) user guide. Natural Resources Canada, Centre for Remote Sensing, Geodetic Survey Division, 615 Booth Street, Ottawa, Ontario, Canada

NRCan (2005). Real-time IGS Multicast Receive (RTIGSMR) user guide. Natural Resources Canada, Centre for Remote Sensing, Geodetic Survey Division, 615 Booth Street, Ottawa, Ontario, Canada

Pardo-Iguzquiza, E., P.A. Dowd, and D.I.F. Grimes (2005). Anautomatic moving window approach for mapping meteorological data, *Int. J. Climatol*, 25, pp: 665-678.

Rabbel, W., and H. Schuh (1986). The influence of atmosphere loading on VLBI-ecperiments, *J. Geophys*, 59, pp:164-170.

Ramirez, J.A. (2007) The earth-atmosphere system (Course notes), Colorado State University (downloaded from: http://www.engr.colostate.edu/~ramirez).

Roken, C., R. Ware, V. Hove, F. Solheim, C. Alber, and J. Johnson (1993). Sensing atmospheric water vapor with the global positioning system. *Geophysical Research Letters*,Vol. 20, pp: 2631-2634.

Rocken, C., V. Hove, J. Johnson, F. Solheim, R. Ware, R. Bevis, M. Chiswell, and S. Businger (1995). GPS/STORM – GPS sensing of atmospheric water vapor for Meteorology. *Journal of Atmospheric and Oceanographic Technology* 12, pp: 468-478.

Rocken, C., R.A. Anthes, M. Exner, D. Hunt, S. Sokolovskiy, R. Ware, M. Gorbunov, W. Schreiner, D. Feng, B. Herman, Y.H. Kuo, and X. Zou (1997). Analysis and validation of GPS/MET data in the neutral atmosphere, *J. Geophys. Res.* **102** D25, 29849–29866.

Rothacher, M., and G. Beutler (2002). Advanced aspects of satellite positioning. Lecture notes for ENGO 609.90, The University of Calgary, AB, Canada.

Russell, P., and J. Livingston (2003). Aerosol Optical Depth, Ozone & Water Vapor Measurements by Airborne Sun Photometer in SOLVE II: Comparisons to SAGE III, POAM III and Other Measurements. *AGU Fall Meeting*, San Francisco, CA, December 11, 2003.

S & TR (2004). Tropopause Height (download from: https://www.llnl.gov/str/March04/pdfs/03_04.2.pdf).

Seidel, D.J. (1995). Water vapour: distribution and trends (downloaded from: http://www.wiley.co.uk/wileychi/egec/pdf/GB085-W.PDF).

Seko, H., H. Najime and S. Shimada (2004). An evaluation of atmospheric models for GPS data retrieval by output from a numerical weather model, *Journal of the Meteorological Society of Japan*, Vol. 82, No. 1B, pp. 339-350.

Skone, S. and S.M. Shrestha (2003). 4-D modeling of water vapour using a regional GPS network. *Proceedings of the Institute of Navigation 2003 National Technical Meeting*, January 22–24, Anaheim, CA, 809–816.

Skone, K., Y. Gao, O. Al-Fanek, W. Tao, and Y. Chang (2006). Atmospheric Moisture Estimation using GPS on a Moving Platform, *ION GNSS 2006* (September 26-29, 2006), Fort Worth, USA.

Tralli, D.M., T.H. Dixon and S.A. Stephens (1988). The effect of wet tropospheric path delays on estimation of grodetic baselines in the Gulf of California using the Global Positioning System. *J. Geophys. Res*., 93:6545-6557.

Tralli, D.M. and S.M. Lichten (1990). The stochastic estimation of tropospheric path delays in global positioning system geodetic measurements, *Bull. Geod*. pp: 127-159.

Tregoning, P., and T.V. Dam (2005). Atmospheric pressure loading corrections applied to GPS data at the observation level, *Geophysical Research Letters*, Vol. 32, L22310.

Ware, R., C. Alber, C. Rocken, and F. Solheim (2001). Sensing integrated water vapor along GPS ray paths, *Geophysical Research Letters*, Vol. 24, No. 4, pp: 417- 420.

Ware, R.H., D.W. Fulker, S.A. Stein, D.N. Anderson, S.K. Avery, R.D. Clark, K.K. Droegemeier, J.P. Kuettner, J. B. Minster, and S. Sorooshian (2001). Real-time national GPS networks for atmospheric sensing, *Journal of Atmospheric and Solar – Terrestrial Physics*, Vol 63, Issue 12, pp:1315-1330.

Ware, R., J. Braun, S.-Y. Ha, D. Hunt, Y.-H. Kuo, C. Rocken, M. Sleziak, T. Van Hove, J. Weber, and R. Anthes (2003). Real-time water vapour sensing with SUOMINET – today and tomorrow. *International GPSMET Workshop*, Tsukuba, Japan.

Warren, D.L.M., and J.F. Raquet (2003). Broadcast vs. precise GPS ephemerides: a historical perspective, *GPS Solutions*, 7:151-156.

Warner, C.D. (2006). Lecture notes: METO 200 (downloaded from the Internet).

Webster, R. and M., Oliver(2001). *Geostatistics for Environmental Scientists*, John Wiley & Sons, LTD.

Williams (2008). Earth's Atmosphere (downloaded from:

http://www.williamsclass.com/EighthScienceWork/Atmosphere/EarthsAtmosphere.htm).

Willkommen, (2005). GPS – explained (downloaded from: http://www.kowoma.de/en/gps/)

Wolfe, D., and S. Gutman (2000). Developing an operational, surface-based, GPS, water vapour observing system for NOAA: network design and results, *Journal of Atmospheric and Oceanic Technology*, Vol. 17, pp: 426-440.

Wu, J.T., S.C. Wu, G.A. Hajj, W.I. Bertiger, and S.M. Lichten (1993). Effects of antenna orientation on GPS carrier phase, *Man. Geodetica* 18, pp: 91-98.

Yuan, L.L., R.A. Anthes, R.H. Ware, C. Rocken, W.D. Bonner, M.G. Bevis, and S. Businger (1993). Sensing climate change using the global positioning system, *Journal of geophysical research*, Vol. 98, NO. D6, pp: 14,925-14,937.

Zhang, J. (1999). Investigations into the estimation of residual tropospheric delays in a GPS network (Thesis). Department of Geomatics Engineering, The University of Calgary.

Zimmerman, D.L. and M.B. Zimmerman (1991). A comparison of spatial semivariogram estimators and corresponding ordinary kriging predictors, *Technometrics*, 33, pp: 77-91.